Dissertation zur Erlangung des Doktorgrades

der Fakultät für Chemie und Pharmazie

der Ludwig-Maximilians-Universität München

# Non-spherical micro- and nanoparticles: Fabrication, Characterization, and in-vitro Investigations



Roman Willi Mathäs

aus Mainz, Deutschland

2015

Erklärung

Diese Dissertation wurde im Sinne von § 7 der Promotionsordnung vom

28.11.2011 von Herrn Prof. Dr. Gerhard Winter von der Fakultät Chemie und
Pharmazie betreut.

Eidesstattliche Versicherung

Diese Dissertation wurde eigenständig und ohne unerlaubte Hilfe erarbeitet.

Basel, den

........................................................

Dissertation eingereicht am:

1. Gutachter: Prof. Dr. Gerhard Winter

2. Gutachter: Prof. Dr. Wolfgang Friess

Mündliche Prüfung am:

Für meine Eltern und Schwestern

## Acknowledgments

# I.    Table of Contents

# I.  Chapter 1

## Aim of This Thesis

Micro- and nanoparticles are investigated extensively for biomedical applications like drug delivery or vaccination. The majority of the studies are performed with spherical particles, which can feature different particle properties. Common design parameters are size, surface charge or attached target ligands. In contrast particle shape is usually neglected. The current thesis aims to fill this gap.

The motivation to investigate non-spherical particles for different drug delivery applications was originated by several non-spherical natural examples. The vision was to transfer the surprising properties of the natural examples to particulate drug delivery systems of tailored geometries [1, 2]. For example, the 7 µm red blood cells (RBCs), which circulated 100-120 days in the body before they are eliminated by macrophages, are discoidal. The non-spherical shape and the flexibility of the RBCs is essential to pass through thin microcapillaries. Certain bacterial strains like *Escherichia coli*, *Aeromonas hydrophila,* or *Streptococcus pneumonia* possess an elongated shape [3], with very unique in-vivo behavior. For example, *Streptococcus pneumonia* evades phagocytosis by the immune system and can circulate remarkably long in the human body. It is still unclear, whether the immune system is insensitive and blind to such elongated organisms or has adopted and triggers an adequate and shape-specific activation response.

Long circulating particles create new possibilities in the field of drug delivery, particle biodistribution, and passive tumor targeting. In contrast, immune activating particles, which mimic pathogens, could be used as vaccine delivery vehicles to boost the immune response and increase patient safety. Therefore, this thesis was divided into two parts to investigate both concepts.

1. Immune evasion:

In the immune evasion part we compared our non-spherical particles to spherical particles in an *in-vitro* macrophages up-take assay to investigate their ability to evade phagocytosis.

2. Immune activation:

In the immune activation part we adsorbed toll-like receptor agonists to our non-spherical particles and spherical particles to compare their ability to activate a dendritic cell line.

In this thesis, we first established a reproducible method (film stretching method in hot oil) to fabricate elongated particles in different size ranges and different aspect ratios (Chapter 2, 3). In a second step, several innovative methods were applied to characterize the non-spherical particles (Chapter 2). Finally, the impact of particle shape was investigated with two *in-vitro* cell lines (Chapter 4, 5).

During the non-spherical particle characterization experiments we realized the importance of the gathered knowledge in the field of protein formulation (Chapter 6). Despite the fact that the topic of this thesis does not directly address protein formulation several publication in this field were published including the publication in chapter 6.

# Non-spherical Micro- and Nanoparticles: Fabrication, Characterization and Drug Delivery Applications

## 1. Abstract

**Introduction:** Micro- and nanoparticles in drug and vaccine delivery have opened up new possibilities in pharmaceutics. In the past, researchers focused mainly on particle size, surface chemistry and the use of various materials to control particle characteristics and functions. Lately, shape has been acknowledged as an important design parameter having an impact on the interaction with biological systems.

**Areas covered:** In this review, we report on the latest developments in fabrication methods to tailor particle geometry, summarize analytical techniques for non-spherical particles, and highlight the most important findings regarding their interaction with biological systems and their potential applications in drug delivery.

**Expert opinion:** The impact of shape on particle internalization into different cell types and particle bio-distribution has been extensively studied in the past. Current research focuses on shape dependent uptake mechanisms and applications for tumor therapy and vaccination. Different fabrication methods can be used to produce a variety of different particle types and shapes. Key challenges will be the transfer of new non-spherical particle fabrication methods from lab-scale to industrial large-scale production. Not all techniques may be scalable for the production of high quantities of particles. It will also be challenging to transfer the promising *in vitro* findings to suitable *in vivo* models.

**Keywords:** non-spherical particles; particle fabrication techniques; particle shape; shape analytics

## 2. Introduction

Particulate drug delivery systems have attracted great attention in the past years [4]. Numerous particulate delivery vehicles like liposomes [5], polymeric micro- and nanoparticles [6, 7], micelles [8], carbon nano-tubes [9], microbubbles [10], virus like particles [11], dendrimers [12], and quantum dots [13] have been established. Such particulate carriers have been applied to various fields in the biomedical research domain like bio-imaging [14, 15], treatment [16], and vaccination [17, 18]. Some products have received FDA (United States Food and Drug Administration) approval. This includes Abraxane™, a 130 nm paclitaxel-albumin drug delivery system for second-line breast cancer therapy [19], and Doxil/Caelyx™, a PEGylated liposomal doxorubicin formulation for various cancer treatments [20].

The observed interest in such carriers and the exponential increase in particle-based biomedical publications and patents can be explained by several advantages these particulates offer [21], such as the possibility of tailoring them to achieve active or passive targeting that in turn allows drug enrichment at the tumor site [22]. Additionally, they can improve the efficiency and the toxicological profile of available therapies, which has been demonstrated in several clinical trials [4, 23], in which the encapsulated drugs are protected from degradation [24] or the dosing intervals can be reduced by a controlled and prolonged drug release [25].

Despite these benefits, some challenges remain unsolved. Upon intravenous (i.v.) injection, a protein corona is formed on particulate carriers [26], that leads to an adsorption of opsonins on their surface [26] and a rapid particle elimination from the blood circulation by the reticuloendothelial system (RES) [27]. In addition, nanoparticle delivery confronts difficulties in crossing biological barriers [28, 29]. Thus, particles face a challenging *in vivo* environment that includes the interaction with serum proteins, different cell types, complex fluid dynamics, and various biological barriers [30]. This can lead to several limitations, such as a preliminary release of payload, an aggregation due to an

interaction with serum components [31], a premature removal from the blood stream [32, 33], and a low target efficiency [34].

These limitations regarding particulate delivery systems have been approached by several researchers who use different strategies that primarily focus on particle size and surface chemistry. The role of particle size is well described and has a large impact on particle fate *in vivo*. For example, particles of a size smaller than 5 nm are rapidly eliminated from free circulation through extravasation or renal clearance [35], while larger particles up to the micrometer range preferentially accumulate in the liver and the spleen [36]. In addition, tailored surface chemistries are common methods to avoid opsonization and elimination by the RES. Hydrophilic polymeric chains like polyethylene glycol (PEG) [37], hydroxyethyl starch (HES) [38] or polysialic acid (PSA) [39] are adsorbed or covalently linked to the particles' surface to prevent serum proteins adsorption in order to achieve prolonged circulation times [40].

Recently, particle shape has emerged as a new design parameter to control micro- and nanoparticles properties, which impact their interaction with biological systems [41, 42]. Such progress was enabled by new and precise production and characterization methods of non-spherical particles [43]. Additionally, major advances towards a sound understanding of particle shape effects on biological interactions have been published by a growing number of researchers [41]. In this review, we will focus on the latest progresses in the field of non-spherical particle fabrication, characterization, the effect of geometry on biological interactions and their *in vitro* and *in vivo* applications.

## 3. Particle fabrication

Several different techniques are now available to produce non-spherical particles. In the following section we describe methods allowing *de-novo* synthesis of non-spherical particles or methods that process already formed spherical particles towards different shapes.
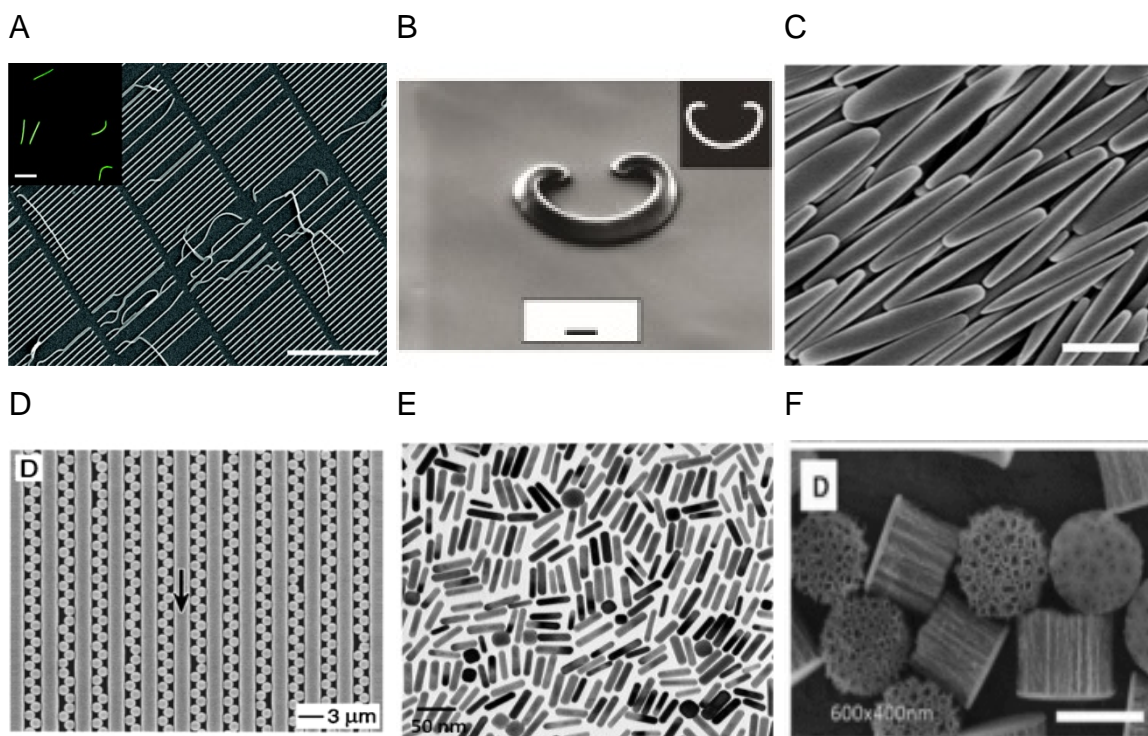
Figure I-1 A) PRINT particles, the scale bar is 5 µm [44], B) Continuous flow lithography particle, the scale bar is 10 µm [45], C) Film-stretched particles, the scale bar is 2 µm [46], D) Template self-assembly particles, the scale bar is 4 µm [47], E) Gold nano-rods, the scale bar is 50 nm [48], F) Porous silicon particles, the scale bar is 500 nm [49]

### 3.1. Non-wetting templates

The particle fabrication method PRINT (Particle Replication In Non-wetting Templates) was established by the group of DeSimone (Figure I-1 A). Here, non-wetting characteristics of fluorinated materials are used to force raw materials into a designable mold where they are photo-chemically cross-linked (Figure I-2). The PRINT technology gives full control over particles' size (below 100 nm – micrometer), shape, flexibility [44], surface functionalization [50] and charge, as well as the possibility to change those attributes individually [51]. Particles can be produced from different materials like lipid-complexes such astripropylenglycol diacrylate [52], polyethylene - glycol (PEG) and polylactic-

co-glycolic acid (PLGA) [53], or a combination thereof [15, 54], and loaded with drugs by simple incorporation into the raw material [55-58].
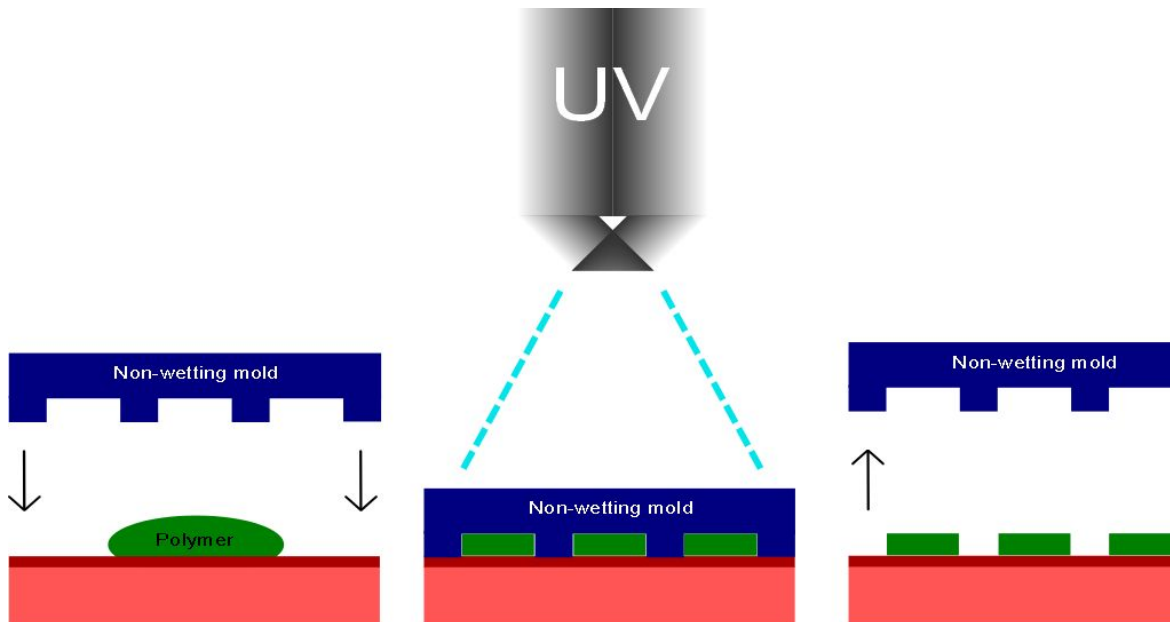


Figure I-2: Schematic illustration of the preparation of non-spherical particles using a non-wetting mold fabrication process.

### 3.2. Microfluidic systems

Microfluidic devices are promising systems to fabricate non-spherical particles of different sizes, shapes (Figure I-1 B), porosities, and materials [59, 60]. Especially microfluidic systems coupled to lithography [61, 62], photolithography [63] and template assembly processes [47] have proven their potential to create complex particle shapes. A schematic illustration of a microfluidic system is given in Figure I-3. Optical microscopes equipped with digital micromirrow devices, which precisely project UV light to the microfluidic channel, allow precise design of microparticles' shape at will [64-66]. With all the benefits of the versatile method, traditional microfluidic devices do not exceed a flow rate of 5 ml/h and are not feasible for industrial particle production. However, Nisisako

*et al.* reported a first approach to scale up production with a circularly arranged microfluidic chip processing up to 320 ml/h [67].
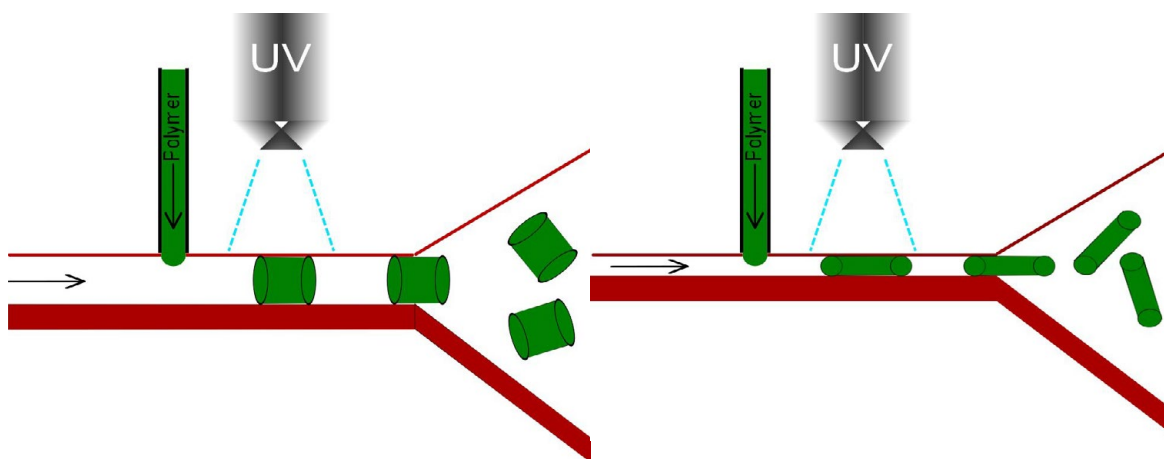


Figure I-3: Schematic illustration of the preparation of non-spherical particles using a microfluidic system. The outlet channel defines particle geometry. A) high aspect ratio particles, B) cylindrical particles.

### 3.3. Film-stretching

The film stretching method is another simple but versatile technique to produce non-spherical polymeric particles of numerous shapes in the micro- and nanometer range (see Figure I-1 C) [46, 68, 69]. Spherical particles are embedded into a PVA film, liquefied in hot oil over the particles' $t_g$ or a plasticizer like toluene and then stretched in one or two dimensions. The stretching process is achieved by strong association by hydrogen bonding of liquefied particles and the film. The stretching degree and temperature, as well as film and particle properties determine the aspect ratio. The stretching degree is proportional to the final aspect ratio, while temperature or the use of a plasticizer determines the viscosity of liquefied particles. A low particle viscosity results in flat shapes. Two - dimensional stretches can create complex geometries [2]. Non-spherical particles are recovered by dissolving the film. A schematic illustration of the film-stretching method is provided in Figure I-4.

Different polymeric materials like polystyrene or biodegradable PLGA [70] have been successfully treated. Despite the simplicity of the film-stretching method, an industrial scale up is rather problematic as films have to be stretched individually and a continuous production process is not possible.
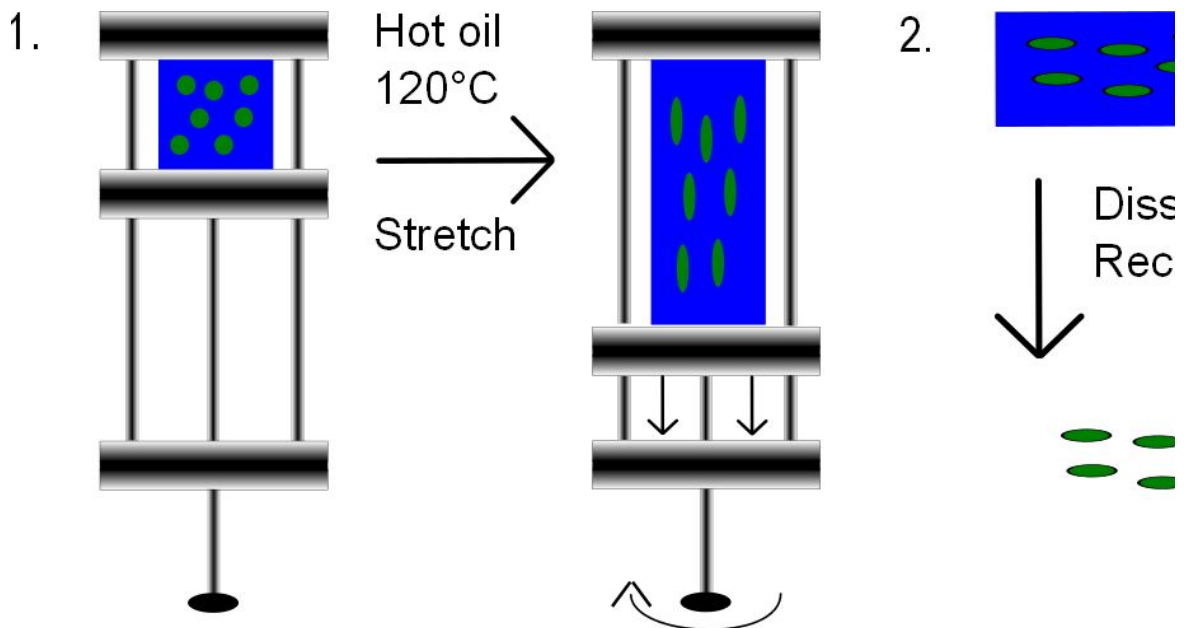


Figure I-4: Schematic illustration of the preparation of non-spherical particles using the film stretching method.

## 3.4. Template-assembly

Similar to the film-stretching method, spherical particles are used as starting material for template-assembly (Figure I-1 D). Spheres are forced into well-defined arrays and joined together by cross-linking agents or heat [71]. The process is illustrated in Figure I-5. Long chains of connected spheres display high aspect ratios [72]. Self-assembly techniques and microfluidics are often combined to produce non-spherical colloidal structures [73]. Velev *et al.* have shown that it is possible to grow differently sized and shaped colloidal crystals by varying the aqueous droplets in the assembly suspension [74]. Kohler *et al.* reported on a template-assisted polyelectrolyte encapsulation method. Here,

nanoporous membranes were used into which nanoparticles were deposited. Nanoparticles in the pores where then encapsulated by polyelectrolytes due to electrostatic interactions, and colloidal, non-spherical nanoparticles or nanostructured microfibers were obtained [75]. Nonetheless, a scale up of non-spherical particle production with template assembly techniques is problematic and has not been reported yet.
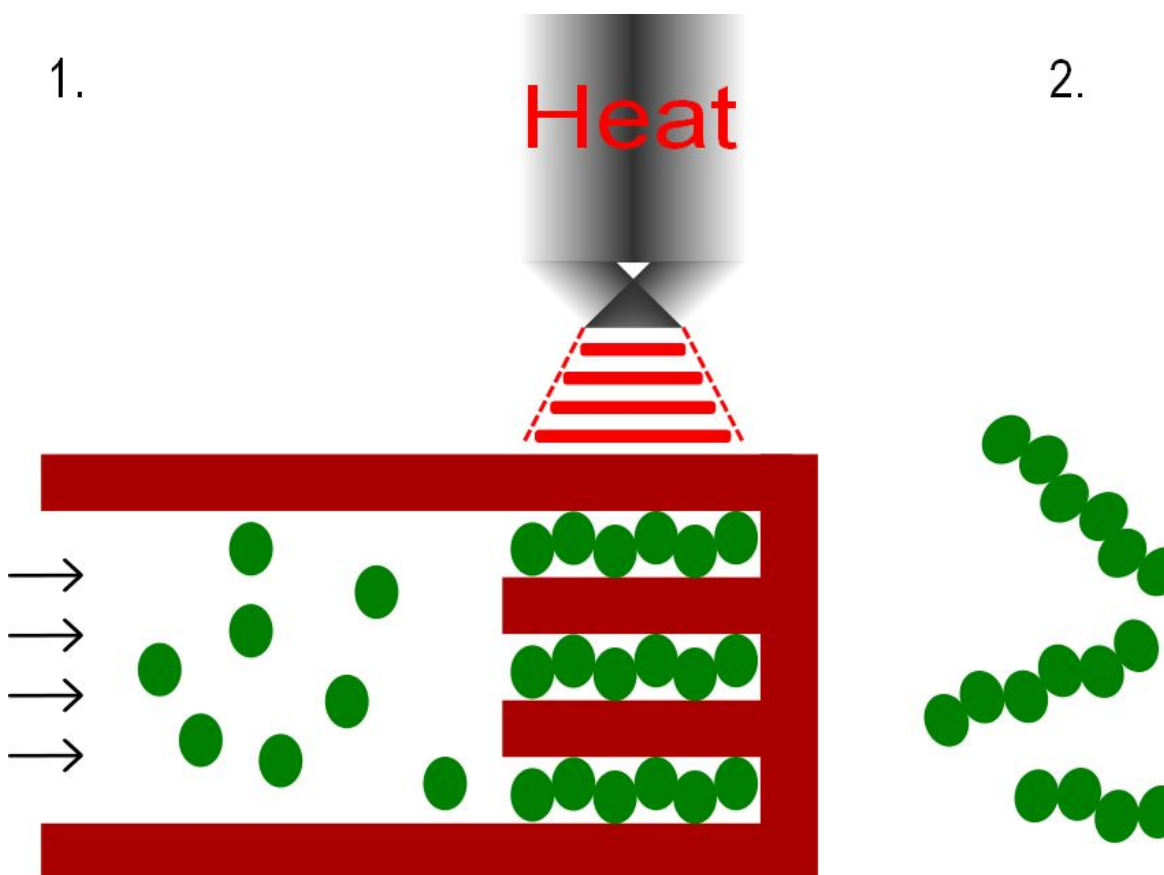


Figure I-5: Schematic fabrication process of high aspect ratio template assembly particles.

### 3.5. Further techniques

Several other non-spherical particle production methods have been reported lately. For example, three fabrication processes to create gold nano-rods (NRs) (Figure I-1 E) have been reported: A template- [76], electrochemical- [77] and

seed growth method, which was improved towards a high yield (ca. 90%) and designable aspect ratios (up to 18) [78]. The seed grow method usually involves the addition of toxic cetyl-trimethylammonium bromid (CTAB) in the fabrication process, which cannot be washed off and limits bio-medical applications. Functionalized mesoporous silica can condensate to particles with various morphologies (Figure I-1 F) [79, 80]. Other methods involved the use of a piezoelectric inkjet printer to create drug loaded polymeric microparticles [81] or ball milling conventional glass wool to non-spherical needles [82]. Furthermore, PEGylated carbon nanotubes (single-wall nanotubes (SWNTs)) can be produced by an electric arc and laser ablation method [83]. Lepeltier *et al.* reported on an amphiphilic prodrug of gemcitabine that self-assembled spontaneously in water as non-spherical nanoparticles [84]. Moreover, non-spherical lipid platelets have been produced by high-pressure homogenization [85]. Finally, different polymeric micelles were produced from block copolymers, where non-spherical flexible micelles can be produced in a wide size range from nanometers [86] to micrometers [87] at different aspect ratios.

## 4. Characterization of non-spherical particles

Following the preparation process, a characterization of the non-spherical particles is an essential step in analyzing and controlling product quality. While electron microscopy is the standard method for particle analysis, other methods such as microflow imaging (MFI), flow cytometry and asymmetric flow field flow fractionation (AF4) can be used as high to medium-throughput analytical methods.

### 4.1. Scanning electron microscopy (SEM)

Scanning electron microscopy is by far the most commonly used method to image particles in the micro- and nanometer range. However, samples require an elaborative, water free sample preparation. The image analysis is time

consuming and has no high through-put capabilities for quality control. Several other methods for quality control and shape characterization of non-spherical particles have been evaluated [43].

## 4.2. Microflow imaging (MFI)

Microflow imaging techniques capture images of particles suspended in a fluid as they pass through the flow cell. By this the precise shape of micro-sized particles can be analyzed, and it can be used to quantitatively identify the quality of film-stretched particles in few minutes with no sample preparation [43]. This method allows analyzing particles down to a size of 5 μm. However, characterization of particle shape below 5 μm is not possible as the resolution is insufficient.

## 4.3. Flow cytometry

Flow cytometry (or fluorescence-activated cell sorting, FACS) is usually used to analyze fluorescent cells. It was also shown that the method can be used to measure a mixture of spherical and non-spherical particles, which pass a static light scattering module with forward and side detectors. The method can analyze particles in the medium to low micrometer range, and can quantify the amount of non-spherical particles and spherical contaminants, since the former scatter more light to the forward detector [43]. However, this method does not provide information about the exact particle size or shape.

## 4.4. Asymmetric flow field flow fractionation (AF4)

Asymmetric flow field flow fractionation (AF4) coupled to multi angel laser light scattering (MALLS) and quasi-elastic light scattering (QELS) can be used to analyze particle shape in the nanometer range. The hydrodynamic radius is not

affected by particle shape, whereas the geometric radius increases with non-spherical shapes. The quotient of the geometric radius (form MALLS) and the hydrodynamic radius (from QELS) is a factor for particle geometry [43]. Spherical particles display a shape factor (SF) of 1, whereas elongated, non-spherical particles have an increased SF of 1.5 – 2.

## 5. Biological Interactions

Table I-1: Overview of different non-spherical particle platforms and the biological effect of particle geometry.

| Particle type | Shape | Biological effect | Fig. | Ref. | |
|---|---|---|---|---|---|
| PRINT - particle | Elongated | Uptake increase | 1a | [51] 2008 | Gratton |
| Film-stretching | 2D particle design at will | Uptake-decrease, targeting increased | 1c | [88] 2013 | Barua |
| Gold particles | Rods | Uptake decreased, half-life increased, | 1e | [48] 2011 | Arnida |
| Silica | Rods | Uptake decreased | 1f | [89] 2013 | Herd |
| Micelles | Worm-like | Uptake decreased, half-life increased, | 1e | [87] 2007 | Geng |

### 5.1. Particle uptake and uptake mechanism

Shape effect on particle internalization was extensively investigated in phagocytic and non-phagocytic cells using different approaches (Table I-1). The group of Mitragotri manipulated spherical particles by the film-stretching method towards numerous shapes. This allowed a comparison of spherical and non-spherical particles of the same material, surface charge and volume. For

instance they showed that IgG-coated 1 μm and 3 μm ellipsoid rods displayed a 10 times lower internalization by rat macrophages [90]. We benchmarked particle shape and PEGylation as two uptake inhibiting tools in J774.A1 macrophages. PEGylation and an elongated shape reduced internalization to the same extent. In addition, a combination of the non-spherical particle shape and PEGylation displayed additive effects [91]. Similar results were found using differently shaped gold nanoparticles, where Qiu *et al.* investigated gold nano-rods of different aspect ratios. A decreased internalization of gold nano-rods was found with increased aspect ratios in MCF-7 cells [92]. These findings could be transferred to different cell types and particle coatings [93] and surface chemistries (PEGylation) [48, 94]. For instance, Agarwal *et al.* investigated differently sized and shaped polyethylene glycol diacrylate hydrogel nanoparticles in several cell types, where elongated particle-shape lowers particle internalization [95]. Similarly, filamentous block-copolymer micelles displayed a decreased cellular uptake by CHO-K1 and macrophages under static- [96] and fluid dynamic conditions [87]. The observed reduction in uptake of elongated particles can be time dependent. In HUVEC cells, 1 μm PLGA spheres had a 4-5 times increased inner cell concentration in the first 30 min of incubation compared to elongated ellipses, while the difference was almost equaled out to 1.25 times after 4 h [70, 97, 98].

The long flat axis of elongated spheres or oblate discs gives them unique adhesive and targeting features. Decuzzi *et al.* discussed the receptor mediated binding of circulating non-spherical particles and predicted an ideal size of 100 nm – 500 nm for targeted drug delivery systems [99, 100]. The two uptake inhibition aspects and enhanced receptor mediated binding were illustrated in a study by Barua *et al.*, where 200 nm elliptical particles coated with BSA displayed a reduced unspecific internalization into BT-474 (Her2$^+$) cells compared to spherical particles. In contrast, Trastuzumab coated ellipses showed an 2.3 fold enhanced uptake [88]. An elongated particle shape resulted in reduced particle internalization. However, Gratton *et al.* investigated differently sized and shaped PRINT particles in HELA cells. 150 nm cylindrical particles with an aspect ratio of 3 displayed an increased internalization

compared to cylindrical nanoparticles with an aspect ratio of 1 [51]. *In vitro* particle internalization is a combination of particle sedimentation, particle attachment to the cell surface and the process of membrane deformation [95]. Non-spherical particles display a greater surface to volume ratio, which promotes cell membrane attachment [98]. However, the energy required to bend the cell membrane around non-spherical particles is greater compared to their spherical counterparts. The competition of the two subtending processes will determine uptake kinetics of different shapes. [95].

The mechanism of uptake of non-spherical and spherical particles with different sizes was investigated in several studies with various cell uptake inhibitors. Herd *et al.* compared the internalization of 200 nm spherical and worm-like silica nanoparticles in RAW 264.7 macrophages. The clarithrin-mediated endocytotic uptake inhibitor chlorpromazine reduced the internalization of spheres below 20% of the controls. The uptake of worm-like silica particles was not affected by chlorpromazine (over 80% of control). The macropinocytosis blocker wortmannin preferentially blocked internalization of worms, while caveolae inhibitors had no influence on cellular particle uptake [89]. These results suggest that spherical particles are primary taken up by clarithrin-mediated endocytosis, while the worm-like structures are internalized by macropinocytosis or phagocytosis. Chlorpromazine elicited similar uptake reducing effects of discoidal and cylindrical nanoparticles in HeLa cells like in the RAW 264.7 cells. Only minor differences in uptake were observed in HEK 293 and HUVEC cells. In HEK 293 the major internalization route for discoidal particles was caveolae mediated, while inhibition of calveolae had no effect on high aspect ratio cylindrical nanoparticles [95]. No uptake inhibitor could block particle uptake completely, suggesting that a combination of different internalization routs is usually involved [89]. These uptake mechanism studies show that particle internalization is a complex process which is also dependent on several experimental setups. Major differences were observed between the different cell types, shapes and particle raw materials.

## 5.2. Blood circulation time

The fluid dynamics of micro- and nanoparticles in the blood stream is shape-dependent and has an influence on plasma half-life time. Different computer models suggest that a non-spherical particle-shape promotes lateral drift towards the vascular endothelia [101]. The theoretical findings were confirmed using *in vitro* flow chamber systems, where non-spherical particles preferentially attached to the flow chamber wall [69, 102, 103]. Despite these *in vitro* findings, numerous *in vivo* models have proven a superior blood circulation half-life time of non-spherical particles. *In vivo* blood circulation half-life time is a complex interplay of adhesion to the vascular endothelia, uptake by cells of the RES and passing natural barriers in the liver, lung and spleen, which is difficult to simulate *ex-vivo*. Arnida *et al.* compared blood levels of PEGylated gold nano-spheres and nano-rods after i.v. administration at a 6 h time point in mice. Nano-rods had a plasma concentration of 11% of the injected dose whereas spheres concentrations stayed below 1% [48]. Other groups achieved comparable results to Arnida *et al.* with PEGylated nano-rods [104-106]. Elongated 15 µm flexible filomicelles circulated in the blood stream for 7 days, while spherical stealth micelles from the same polymeric material were cleared after 2 days [87]. PEGylated single-walled carbon nanotubes (SWNTs) reach a plasma half-life time of 2 h [107], nano-graphene sheets 7 h (beta-phase) [108]. Merkel and co-workers applied the physical properties of long circulating red-blood cells to flexible hydroxyl PEG acrylate (HPA) discoidal micro- and nanoparticles. The flexibility of the discs allows passing small capillaries in the lung and the 200 nm filtration slits in the spleen. 6.4 µm discs had a blood concentration of 13.2% of the injected dose after 104 h [109, 110]. Particle geometry has proven a clear influence on particles' blood circulation time. However, *in vivo* half-life time is an interplay of particle size, shape, surface chemistry and material properties. More studies need to elucidate the connection of the different drug delivery properties on biological half-life.

## 5.3. Biodistribution

Micro- and nanoparticle geometry plays an important role in their biodistribution. Arnida *et al.* compared the bioaccumulation of i.v. injected PEGylated nano-spheres and nano-rods in ovarian tumor-bearing mice after 6 h. The authors observed a significant lower accumulation of rod-like nanoparticles in the liver and significant higher concentrations (15% of injected dose) in the tumor. Similarly, Akiyama and co-workers found high dosages of PEGylated gold nano-rods in tumor tissue [105]. Long circulating single-walled carbon nano-tubes accumulated 15% of the injected dose in the tumor tissue of mice [107]. The endothelium of the lungs expresses ICAM-1 at basal levels. Kolhar *et al.* coated spherical and elongated 200 nm polystyrene particles with anti-ICAM-1 or anti-transferrin receptor antibody. Anti-ICAM-1 rod-shaped particles accumulated twofold higher in the lungs of mice compared to the spheres. The lung/liver ratio of anti-ICAM-1 rods was 1.7 and only 0.7 for the corresponding spheres. IgG coated non-targeting control particles displayed no shape differences in lung accumulation. The anti-transferrin receptor antibody nano-rods accumulated sevenfold higher in the brain than the coated spheres. This study demonstrates the great targeting potential of high aspect ratio particles [111]. Silica nano-rods preferentially accumulated in the lung [112]. Decuzzi *et al.* investigated the biodistribution of differently shaped silica particles in mice. Discoidal particles displayed a significant low liver entrapment than spherical or cylindrical particles, probably due to the lower propensity of non-spherical particles for cellular uptake by phagocytosis as discussed above. High accumulation of discoidal particles was observed in most of the organs. The higher surface to volume ratio of discs facilitates vessel wall adhesion [100, 113]. Discoidal silica particles (dimensions 600 nm x 400 nm) were found at five times higher concentrations (10.2% of the injected dose / tissue g) in tumors compared to their spherical counter parts [49]. In general, the longer circulation time of non-spherical particles and the increased permeability of tumor vessels (enhanced permeability effect (EPR)) are believed to facilitate the particle enrichment at tumor sites [48].

# 6. Applications

The unique features of non-spherical particles have been applied to several biomedical applications (Table I-2).

Table I-2: Overview of different biomedical application for different non-spherical particulates in drug delivery and vaccination.

| Particle type / shape | Application | Advantage vs. spheres | Reference |
|---|---|---|---|
| Cylindrical PRINT | Vaccination | 5-times immunological response compared to soluble vaccines | [55] Galloway 2013 |
| Gold nano-rods | Vaccination | Higher antibody titer | [114] Niikura 2013 |
| Filomicelles | Drug delivery (cancer) | 2-times apoptosis rate of tumor cells | [87] Geng 2007 |
| Non-spherical PRINT | Drug delivery (cancer) | Not benchmarked | [56] Enlow 2011 |
| Needle shaped PS | Drug delivery (DNA) | Increased knock-down | [111] Kolhar 2013 |

## 6.1. Vaccination

Galloway *et al.* used 320 nm PRINT particles as an influenza vaccine delivery system. The nanoparticles are based on PLGA and cationic additives and display an aspect ratio of 4. The positive zeta-potential as well as the high surface to volume ratio of the non-spherical nanoparticles increased antigen adsorption to 6% w/w. The PRINT nanoparticle bound influenza vaccines displayed a fivefold boosted immunological response (antibody titer response) compared to soluble antigen solutions. The toxicological studies of a broad range of dosages (20 µg – 500 µg) revealed no clinical observations and no significant increases in cytokine levels in mice. In addition, the PRINT technology offers GMP production capabilities to fortify the great potential as a promising drug delivery system for clinical trials [55]. Niikura *et al.* investigated differently sized and shaped gold nanoparticles as vaccine platform. Rod shaped 36 nm x 10 nm nanoparticles displayed a superior antibody titer

production compared to the 20 nm corresponding spheres. However, larger spheres were most efficient, which highlights the complex interplay of particle size, shape and material properties in drug delivery systems [114].

## 6.2. Drug Delivery

Geng *et al.* loaded spherical micelles (aspect ratio 1) and long circulating filomicelles (aspect ratio 8) with paclitaxel. The increase in aspect ratio doubled the apoptosis rate of tumor cells in mice and efficiently decreased the tumor size. The longer half-life time of the filomicelles prolongs paclitaxel exposure to tumor cells and enhances passive targeting (EPR) [87]. Similarly, the group of DeSimone investigated non-spherical particles as chemotherapeutic drug delivery systems. Differently shaped PRINT particles had up to 40% w/w doxetaxel loading with a loading efficiency of >90% [56] and were efficient in a murine cancer model [58].

Kolhar *et al.* used spheres and needle-shaped polymeric nanoparticles to deliver siRNA. The needle shaped particles permeated the cell membrane and induced cytoplasmic delivery. The percent of knock down increased with the aspect ratio of the particles [111].

## 7. Conclusion

The current review highlights the tremendous progresses in the last years regarding non-spherical particle fabrication, characterization and applications. New production processes allow precise control over particle shape, and various analytical methods can be used to check the quality of the produced particles. These new possibilities provided the basis for several studies to understand the effect of particle shape on the different biological interactions, focusing on particle uptake and uptake mechanisms, blood circulation time and biodistribution.

## 8. Expert opinion

The basis of this fast growing research field was a remarkable progress in non-spherical particle fabrication methods. These methods open up new possibilities in the research of drug delivery. The impact of particle shape on cellular interactions and biodistribution was demonstrated in numerous studies. A remarkable difference between the non-spherical particles and their spherical counterparts was observed *in vitro* and *in vivo*. Particle uptake into different cell types is well described and the majority of studies suggest a decreased internalization for non-spherical particles. In addition to this, researchers concentrate on shape dependent uptake mechanism. Nevertheless, only little is known how particle geometry predetermines cellular uptake mechanism.

*In vivo* particle biodistribution has been studied extensively. Longer circulation times can lead to high tumor accumulation of particles by passive targeting. However, the majority of those studies were performed with model particles carrying no drug load. Accordingly, future work needs to transfer the promising results obtained by model particles to suitable drug delivery systems including pharmaceutical drug payloads. Chemotherapeutics and vaccines will play the dominate role.

The overall *in vivo* performance is a combination of particle size, shape, material properties like flexibility and surface chemistry. Particle geometry has the potential to play an important parameter in the design of future drug delivery systems. One of the key challenges is to find suitable spherical control particles to benchmark spherical and non-spherical particles. In other words, the major task is to conserve all particle properties and exclusively manipulate particle shape, which is usually not possible. For example, manipulating particle shape will usually change particle's flexibility and can have an effect on particle aggregation in culture media or *in vivo*. However, flexibility and aggregation behavior of particulated systems have an impact on the overall particle *in vitro* and *in vivo* performance.

The integration of the new design parameters increases complexity of drug delivery systems. Therefore, interdisciplinary teams of material scientist, chemists, pharmacist and biologics/immunologists are needed to match all the requirements needed for future drug delivery system design.

The growing number of particulate drug delivery systems in clinical trials requires suitable large scale production methods. Hence, another key challenge will be to transfer the new fabrication methods for non-spherical particles from lab-scale to large-scale in order to provide particles in sufficient quality and quantity for clinical trials and marketed products.

Finally, two aspects of a non-spherical drug delivery system seem very promising: First, including particle shape among size, surface chemistry and flexibility in the drug delivery design mix provides the possibility to mimic the compelling properties of natural entities like red blood cells. Second, the high surface to volume ratio of non-spherical particles offers possibilities for an active targeting. Consequently, an equal amount of non-spherical particles can carry a multiple of targeting ligands.

The final aim is that through careful engineering of the different design parameters, these particulate carriers will provide superior disease treatment with less undesirable side effects and better patient acceptance.

## 9. References

1. Doshi, N. and S. Mitragotri, *Macrophages recognize size and shape of their targets.* PLoS ONE, 2010. **5**(4): p. e10051.
2. Doshi, N., et al., *Red blood cell-mimicking synthetic biomaterial particles.* Proceedings of the National Academy of Sciences, 2009. **106**(51): p. 21495-21499.
3. Martínez, M.J., et al., *The presence of capsular polysaccharide in mesophilic Aeromonas hydrophila serotypes O:11 and O:34.* FEMS Microbiology Letters, 1995. **128**(1): p. 69-73.
4. Peer, D., et al., *Nanocarriers as an emerging platform for cancer therapy.* Nat Nano, 2007. **2**(12): p. 751-760.
5. Dave, N. and J. Liu, *Liposomes for DNA Nanotechnology: Preparation, Properties, and Applications*, in *DNA Nanotechnology*, C. Fan, Editor 2013, Springer Berlin Heidelberg. p. 57-76.
6. Kirtane, A.R. and J. Panyam, *Polymer nanoparticles: Weighing up gene delivery.* Nat Nano, 2013. **8**(11): p. 805-806.
7. Getts, D.R., et al., *Microparticles bearing encephalitogenic peptides induce T-cell tolerance and ameliorate experimental autoimmune encephalomyelitis.* Nat Biotech, 2012. **30**(12): p. 1217-1224.
8. Koyamatsu, Y., et al., *pH-responsive release of proteins from biocompatible and biodegradable reverse polymer micelles.* Journal of Controlled Release, 2014. **173**(0): p. 89-95.
9. Kato, Y., et al., *Thermodynamics on soluble carbon nanotubes: how do DNA molecules replace surfactants on carbon nanotubes?* Scientific reports, 2012. **2**.
10. Noble, M.L., et al., *Ultrasound-targeted Microbubble Destruction-mediated Gene Delivery Into Canine Livers.* Mol Ther, 2013. **21**(9): p. 1687-1694.
11. Smith, D.M., J.K. Simon, and J.R. Baker Jr, *Applications of nanotechnology for immunology.* Nat Rev Immunol, 2013. **13**(8): p. 592-605.
12. Arima, H., et al., *Potential use of folate-polyethylene glycol (PEG)-appended dendrimer (G3) conjugate with [alpha]-cyclodextrin as DNA carriers to tumor cells.* Cancer Gene Ther, 2012. **19**(5): p. 358-366.
13. Zagorovsky, K. and W.C.W. Chan, *Bioimaging: Illuminating the deep.* Nat Mater, 2013. **12**(4): p. 285-287.
14. Cassidy, M.C., et al., *In vivo magnetic resonance imaging of hyperpolarized silicon particles.* Nat Nano, 2013. **8**(5): p. 363-368.
15. Wang, J., et al., *In vivo self-bio-imaging of tumors through in situ biosynthesized fluorescent gold nanoclusters.* Sci. Rep., 2013. **3**.
16. Clyne, M., *Prostate cancer: Magnetic particle thermotherapy for treating bone metastases.* Nat Rev Urol, 2013. **10**(3): p. 125-125.
17. Irvine, D.J., M.A. Swartz, and G.L. Szeto, *Engineering synthetic vaccines using cues from natural immunity.* Nat Mater, 2013. **12**(11): p. 978-990.
18. Willyard, C., *First vaccines targeting 'cruise ship virus' sail into clinical trials.* Nat Med, 2013. **19**(9): p. 1076-1077.

19. Nijhara, R. and K. Balakrishnan, *Bringing nanomedicines to market: regulatory challenges, opportunities, and uncertainties.* Nanomedicine: Nanotechnology, Biology and Medicine, 2006. **2**(2): p. 127-136.

20. Barenholz, Y., *Doxil® — The first FDA-approved nano-drug: Lessons learned.* Journal of Controlled Release, 2012. **160**(2): p. 117-134.

21. Wagner, V., et al., *The emerging nanomedicine landscape.* Nature biotechnology, 2006. **24**(10): p. 1211-1218.

22. Davis, M.E., Z. Chen, and D.M. Shin, *Nanoparticle therapeutics: an emerging treatment modality for cancer.* Nat Rev Drug Discov, 2008. **7**(9): p. 771-782.

23. Hrkach, J., et al., *Preclinical Development and Clinical Translation of a PSMA-Targeted Docetaxel Nanoparticle with a Differentiated Pharmacological Profile.* Science Translational Medicine, 2012. **4**(128): p. 128ra39.

24. Sahay, G., et al., *Efficiency of siRNA delivery by lipid nanoparticles is limited by endocytic recycling.* Nat Biotech, 2013. **31**(7): p. 653-658.

25. Tsurkan, M.V., et al., *Growth factor delivery from hydrogel particle aggregates to promote tubular regeneration after acute kidney injury.* Journal of Controlled Release, 2013. 167(3): p. 248-255.

26. Tenzer, S., et al., *Rapid formation of plasma protein corona critically affects nanoparticle pathophysiology.* Nat Nano, 2013. **8**(10): p. 772-781.

27. Sakurai, Y., et al., *Gene Silencing via RNAi and siRNA Quantification in Tumor Tissue Using MEND, a Liposomal siRNA Delivery System.* Molecular Therapy, 2013. 21(6): p. 1195-1203.

28. Dobrovolskaia, M.A. and S.E. McNeil, *Immunological properties of engineered nanomaterials.* Nature nanotechnology, 2007. **2**(8): p. 469-478.

29. José Alonso, M., *Nanomedicines for overcoming biological barriers.* Biomedicine & Pharmacotherapy, 2004. **58**(3): p. 168-172.

30. Chauhan, V.P., et al., *Normalization of tumour blood vessels improves the delivery of nanomedicines in a size-dependent manner.* Nat Nano, 2012. **7**(6): p. 383-388.

31. Hotze, E.M., T. Phenrat, and G.V. Lowry, *Nanoparticle Aggregation: Challenges to Understanding Transport and Reactivity in the Environment All rights reserved. No part of this periodical may be reproduced or transmitted in any form or by any means, electronic or mechanical, including photocopying, recording, or any information storage and retrieval system, without permission in writing from the publisher.* J. Environ. Qual., 2010. **39**(6): p. 1909-1924.

32. Lesniak, A., et al., *Serum heat inactivation affects protein corona composition and nanoparticle uptake.* Biomaterials, 2010. **31**(36): p. 9511-9518.

33. Walkey, C.D., et al., *Nanoparticle Size and Surface Chemistry Determine Serum Protein Adsorption and Macrophage Uptake.* Journal of the American Chemical Society, 2011. **134**(4): p. 2139-2147.

34. Salvati, A., et al., *Transferrin-functionalized nanoparticles lose their targeting capabilities when a biomolecule corona adsorbs on the surface.* Nat Nano, 2013. **8**(2): p. 137-143.

35. Ernsting, M.J., et al., *Factors controlling the pharmacokinetics, biodistribution and intratumoral penetration of nanoparticles.* Journal of Controlled Release, 2013. **172**(3): p. 782-794.

36. Kutscher, H.L., et al., *Threshold size for optimal passive pulmonary targeting and retention of rigid microparticles in rats.* Journal of Controlled Release, 2010. **143**(1): p. 31-37.

37. Otsuka, H., Y. Nagasaki, and K. Kataoka, *PEGylated nanoparticles for biological and pharmaceutical applications.* Advanced Drug Delivery Reviews, 2012.

38. Noga, M., et al., *The effect of molar mass and degree of hydroxyethylation on the controlled shielding and deshielding of hydroxyethyl starch-coated polyplexes.* Biomaterials, 2013. **34**(10): p. 2530-2538.

39. Bader, R.A., A.L. Silvers, and N. Zhang, *Polysialic Acid-Based Micelles for Encapsulation of Hydrophobic Drugs.* Biomacromolecules, 2011. **12**(2): p. 314-320.

40. Owens III, D.E. and N.A. Peppas, *Opsonization, biodistribution, and pharmacokinetics of polymeric nanoparticles.* International Journal of Pharmaceutics, 2006. **307**(1): p. 93-102.

41. Champion, J.A., Y.K. Katare, and S. Mitragotri, *Particle shape: A new design parameter for micro- and nanoscale drug delivery carriers.* Journal of Controlled Release, 2007. **121**(1-2): p. 3-9.

42. Daum, N., et al., *Novel approaches for drug delivery systems in nanomedicine: effects of particle design and shape.* Wiley Interdisciplinary Reviews: Nanomedicine and Nanobiotechnology, 2012. **4**(1): p. 52-65.

43. Mathaes, R., et al., *Application of different analytical methods for the characterization of non-spherical micro- and nanoparticles.* International Journal of Pharmaceutics, 2013. **453**(2): p. 620-629.

44. Kersey, F.R., et al., *Effect of Aspect Ratio and Deformability on Nanoparticle Extravasation through Nanopores.* Langmuir, 2012. **28**(23): p. 8773-8781.

45. Dendukuri, D., et al., *Continuous-flow lithography for high-throughput microparticle synthesis.* Nature Materials, 2006. **5**(5): p. 365-369.

46. Champion, J.A., Y.K. Katare, and S. Mitragotri, *Making polymeric micro- and nanoparticles of complex shapes.* Proceedings of the National Academy of Sciences, 2007. **104**(29): p. 11901-11904.

47. Yin, Y., et al., *Template-Assisted Self-Assembly: A Practical Route to Complex Aggregates of Monodispersed Colloids with Well-Defined Sizes, Shapes, and Structures.* Journal of the American Chemical Society, 2001. **123**(36): p. 8718-8729.

48. Arnida, et al., *Geometry and surface characteristics of gold nanoparticles influence their biodistribution and uptake by macrophages.* European Journal of Pharmaceutics and Biopharmaceutics, 2011. **77**(3): p. 417-423.

49. Godin, B., et al., *Discoidal porous silicon particles: fabrication and biodistribution in breast cancer bearing mice.* Advanced Functional Materials, 2012. **22**(20): p. 4225-4235.

50. Morton, S.W., et al., *Scalable Manufacture of Built-to-Order Nanomedicine: Spray-Assisted Layer-by-Layer Functionalization of PRINT Nanoparticles.* Advanced Materials, 2013. **25**(34): p. 4707-4713.

51. Gratton, S.E., et al., *The effect of particle design on cellular internalization pathways.* Proceedings of the National Academy of Sciences, 2008. **105**(33): p. 11613-11618.

52. Xu, J., et al., *RNA Replicon Delivery via Lipid-Complexed PRINT Protein Particles.* Molecular Pharmaceutics, 2013. **10**(9): p. 3366-3374.

53. Rolland, J.P., et al., *Direct Fabrication and Harvesting of Monodisperse, Shape-Specific Nanobiomaterials.* Journal of the American Chemical Society, 2005. **127**(28): p. 10096-10100.

54. Zhang, H., et al., *Fabrication of multiphasic and regio-specifically functionalized PRINT® particles of controlled size and shape.* New Journal of Physics, 2009. **11**(7): p. 075018.

55. Galloway, A.L., et al., *Development of a nanoparticle-based influenza vaccine using the PRINT® technology.* Nanomedicine: Nanotechnology, Biology and Medicine, 2013. **9**(4): p. 523-531.

56. Enlow, E.M., et al., *Potent Engineered PLGA Nanoparticles by Virtue of Exceptionally High Chemotherapeutic Loadings.* Nano Letters, 2011. **11**(2): p. 808-813.

57. Petros, R.A., P.A. Ropp, and J.M. DeSimone, *Reductively Labile PRINT Particles for the Delivery of Doxorubicin to HeLa Cells.* Journal of the American Chemical Society, 2008. **130**(15): p. 5008-5009.

58. Chu, K.S., et al., *Nanoparticle drug loading as a design parameter to improve docetaxel pharmacokinetics and efficacy.* Biomaterials, 2013. **34**(33): p. 8424-8429.

59. Xu, S., et al., *Generation of Monodisperse Particles by Using Microfluidics: Control over Size, Shape, and Composition.* Angewandte Chemie, 2005. **117**(5): p. 734-738.

60. Shang, L., et al., *Microfluidic generation of magnetoresponsive Janus photonic crystal particles.* Nanoscale, 2013. **5**(20): p. 9553-9557.

61. Hakimi, N., et al., *One-Step Two-Dimensional Microfluidics-Based Synthesis of Three-Dimensional Particles.* Advanced Materials, 2013: p. n/a-n/a.

62. Dendukuri, D., et al., *Continuous-flow lithography for high-throughput microparticle synthesis.* Nat Mater, 2006. **5**(5): p. 365-369.

63. Love, J.C., et al., *Microscope Projection Photolithography for Rapid Prototyping of Masters with Micron-Scale Features for Use in Soft Lithography.* Langmuir, 2001. **17**(19): p. 6005-6012.

64. Lee, S.A., et al., *Three-dimensional fabrication of heterogeneous microstructures using soft membrane deformation and optofluidic maskless lithography.* Lab on a Chip, 2009. **9**(12): p. 1670-1675.

65. Chung, S.E., et al., *Guided and fluidic self-assembly of microstructures using railed microfluidic channels.* Nat Mater, 2008. **7**(7): p. 581-587.

66. Kim, H., et al., *Structural colour printing using a magnetically tunable and lithographically fixable photonic crystal.* Nat Photon, 2009. **3**(9): p. 534-540.

67. Nisisako, T. and T. Torii, *Microfluidic large-scale integration on a chip for mass production of monodisperse droplets and particles.* Lab on a Chip, 2008. **8**(2): p. 287-293.

68. Ho, C.C., et al., *Preparation of monodisperse ellipsoidal polystyrene particles.* Colloid &amp; Polymer Science, 1993. **271**(5): p. 469-479.

69. Doshi, N., et al., *Flow and adhesion of drug carriers in blood vessels depend on their shape: a study using model synthetic microvascular networks.* Journal of Controlled Release, 2010. **146**(2): p. 196-200.

70. Yoo, J.-W., N. Doshi, and S. Mitragotri, *Endocytosis and Intracellular Distribution of PLGA Particles in Endothelial Cells: Effect of Particle Geometry.* Macromolecular Rapid Communications, 2010. **31**(2): p. 142-148.

71. Yin, Y. and Y. Xia, *Self-Assembly of Monodispersed Spherical Colloids into Complex Aggregates with Well-Defined Sizes, Shapes, and Structures.* Advanced Materials, 2001. **13**(4): p. 267-271.

72. Yin, Y. and Y. Xia, *Self-Assembly of Spherical Colloids into Helical Chains with Well-Controlled Handedness.* Journal of the American Chemical Society, 2003. **125**(8): p. 2048-2049.

73. Vanapalli, S.A., et al., *Fluidic assembly and packing of microspheres in confined channels.* Langmuir, 2008. **24**(7): p. 3661-3670.

74. Velev, O.D., A.M. Lenhoff, and E.W. Kaler, *A Class of Microstructured Particles Through Colloidal Crystallization.* Science, 2000. **287**(5461): p. 2240-2243.

75. Kohler, D., et al., *Template-Assisted Polyelectrolyte Encapsulation of Nanoparticles into Dispersible, Hierarchically Nanostructured Microfibers.* Advanced Materials, 2011. **23**(11): p. 1376-1379.

76. Foss Jr, C.A., M.J. Tierney, and C.R. Martin, *Template synthesis of infrared-transparent metal microcylinders: comparison of optical properties with the predictions of effective medium theory.* The Journal of Physical Chemistry, 1992. **96**(22): p. 9001-9007.

77. Yu, Y.-Y., et al., *Gold nanorods: electrochemical synthesis and optical properties.* The Journal of Physical Chemistry B, 1997. **101**(34): p. 6661-6664.

78. Busbee, B.D., S.O. Obare, and C.J. Murphy, *An Improved Synthesis of High-Aspect-Ratio Gold Nanorods.* Advanced Materials, 2003. **15**(5): p. 414-416.

79. Huh, S., et al., *Organic functionalization and morphology control of mesoporous silicas via a co-condensation synthesis method.* Chemistry of materials, 2003. **15**(22): p. 4247-4256.

80. Björk, E.M., F. Söderlind, and M. Odén, *Tuning the Shape of Mesoporous Silica Particles by Alterations in Parameter Space: From Rods to Platelets.* Langmuir, 2013. **29**(44): p. 13551-13561.

81. Lee, B.K., et al., *Fabrication of drug-loaded polymer microparticles with arbitrary geometries using a piezoelectric inkjet printing system.* International Journal of Pharmaceutics, 2012. **427**(2): p. 305-310.

82. Raphael, A.P., et al., *Elongate microparticles for enhanced drug delivery to ex vivo and in vivo pig skin.* Journal of Controlled Release, 2013. **172**(1): p. 96-104.

83. Ajayan, P.M. and O.Z. Zhou, *Applications of carbon nanotubes*, in *Carbon nanotubes*2001, Springer. p. 391-425.

84. Lepeltier, E., et al., *Self-Assembly of Polyisoprenoyl Gemcitabine Conjugates: Influence of Supramolecular Organization on Their Biological Activity.* Langmuir, 2014. **30**(22): p. 6348-6357.

85. Jores, K., W. Mehnert, and K. Mäder, *Physicochemical investigations on solid lipid nanoparticles and on oil-loaded solid lipid nanoparticles: a nuclear magnetic resonance and electron spin resonance study.* Pharmaceutical Research, 2003. **20**(8): p. 1274-1283.

86. Alemdaroglu, F.E., et al., *Cellular uptake of DNA block copolymer micelles with different shapes.* Macromolecular Rapid Communications, 2008. **29**(4): p. 326-329.

87. Geng, Y., et al., *Shape effects of filaments versus spherical particles in flow and drug delivery.* Nat Nanotechnol, 2007. **2**(4): p. 249-55.

88. Barua, S., et al., *Particle shape enhances specificity of antibody-displaying nanoparticles.* Proceedings of the National Academy of Sciences, 2013. **110**(9): p. 3270-3275.

89. Herd, H., et al., *Nanoparticle Geometry and Surface Orientation Influence Mode of Cellular Uptake.* ACS Nano, 2013. **7**(3): p. 1961-1973.

90. Champion, J. and S. Mitragotri, *Shape Induced Inhibition of Phagocytosis of Polymer Particles.* Pharmaceutical Research, 2009. **26**(1): p. 244-249.

91. Mathaes, R., et al., *Influence of particle geometry and PEGylation on phagocytosis of particulate carriers.* International Journal of Pharmaceutics, 2014. 465(1): p. 159-164.

92. Qiu, Y., et al., *Surface chemistry and aspect ratio mediated cellular uptake of Au nanorods.* Biomaterials, 2010. **31**(30): p. 7606-7619.

93. Chithrani, B.D., A.A. Ghazani, and W.C.W. Chan, *Determining the Size and Shape Dependence of Gold Nanoparticle Uptake into Mammalian Cells.* Nano Letters, 2006. **6**(4): p. 662-668.

94. Malugin, A. and H. Ghandehari, *Cellular uptake and toxicity of gold nanoparticles in prostate cancer cells: a comparative study of rods and spheres.* Journal of Applied Toxicology, 2010. **30**(3): p. 212-217.

95. Agarwal, R., et al., *Mammalian cells preferentially internalize hydrogel nanodiscs over nanorods and use shape-specific uptake mechanisms.* Proceedings of the National Academy of Sciences, 2013. **110**(43): p. 17247-17252.

96. Zhang, K., et al., *Shape effects of nanoparticles conjugated with cell-penetrating peptides (HIV Tat PTD) on CHO cell uptake.* Bioconjugate Chemistry, 2008. **19**(9): p. 1880-1887.

97. Muro, S., et al., *Control of endothelial targeting and intracellular delivery of therapeutic enzymes by modulating the size and shape of ICAM-1-targeted carriers.* Molecular Therapy, 2008. **16**(8): p. 1450-1458.

98. Sharma, G., et al., *Polymer particle shape independently influences binding and internalization by macrophages.* Journal of Controlled Release, 2010. **147**(3): p. 408-412.

99. Decuzzi, P. and M. Ferrari, *The adhesive strength of non-spherical particles mediated by specific interactions.* Biomaterials, 2006. **27**(30): p. 5307-5314.

100. Decuzzi, P., et al., *Intravascular Delivery of Particulate Systems: Does Geometry Really Matter?* Pharmaceutical Research, 2009. **26**(1): p. 235-243.

101. Lee, S.-Y., M. Ferrari, and P. Decuzzi, *Shaping nano-/micro-particles for enhanced vascular interaction in laminar flows.* Nanotechnology, 2009. **20**(49): p. 495101.

102. Gentile, F., et al., *The effect of shape on the margination dynamics of non-neutrally buoyant particles in two-dimensional shear flows.* Journal of biomechanics, 2008. **41**(10): p. 2312-2318.

103. Toy, R., et al., *The effects of particle size, density and shape on margination of nanoparticles in microcirculation.* Nanotechnology, 2011. **22**(11): p. 115101.

104. Niidome, T., et al., *PEG-modified gold nanorods with a stealth character for< i> in vivo</i> applications.* Journal of Controlled Release, 2006. **114**(3): p. 343-347.

105. Akiyama, Y., et al., *The effects of PEG grafting level and injection dose on gold nanorod biodistribution in the tumor-bearing mice.* Journal of Controlled Release, 2009. **139**(1): p. 81-84.

106. Perry, J.L., et al., *PEGylated PRINT nanoparticles: the impact of PEG density on protein binding, macrophage association, biodistribution, and pharmacokinetics.* Nano Letters, 2012. **12**(10): p. 5304-5310.

107. Liu, Z., et al., *In vivo biodistribution and highly efficient tumour targeting of carbon nanotubes in mice.* Nature nanotechnology, 2007. **2**(1): p. 47-52.

108. Yang, K., et al., *In vivo pharmacokinetics, long-term biodistribution, and toxicology of PEGylated graphene in mice.* ACS Nano, 2010. **5**(1): p. 516-522.

109. Merkel, T.J., et al., *The effect of particle size on the biodistribution of low-modulus hydrogel PRINT particles.* Journal of Controlled Release, 2012. **162**(1): p. 37-44.

110. Merkel, T.J., et al., *Using mechanobiological mimicry of red blood cells to extend circulation times of hydrogel microparticles.* Proceedings of the National Academy of Sciences, 2011. **108**(2): p. 586-591.

111. Kolhar, P., et al., *Using shape effects to target antibody-coated nanoparticles to lung and brain endothelium.* Proceedings of the National Academy of Sciences, 2013. **110**(26): p. 10753-10758.

112. Yu, T., et al., *In vivo biodistribution and pharmacokinetics of silica nanoparticles as a function of geometry, porosity and surface characteristics.* Journal of Controlled Release, 2012. **163**(1): p. 46-54.

113. Decuzzi, P., et al., *Size and shape effects in the biodistribution of intravascularly injected particles.* Journal of Controlled Release, 2010. **141**(3): p. 320-327.

114. Niikura, K., et al., *Gold nanoparticles as a vaccine platform: influence of size and shape on immunological responses in vitro and in vivo.* ACS Nano, 2013. **7**(5): p. 3926-3938.

# II.  Chapter 2

## Application of different analytical methods for the characterization of non-spherical micro- and nanoparticles

The final aim of the thesis was to investigate non-spherical particles *in-vitro.* However, *in-vitro* experiments require homogenously stretched particles with a defined particle size. In contrast to particle size measuring instruments, instruments measuring particle shape are rare. Therefore, the first major aim of

this thesis was to homogeneously produce and characterize non-spherical micro- and nanoparticles.

# 1. Abstract

Non-spherical micro- and nanoparticles have recently gained considerable attention due to their surprisingly different interaction with biological systems compared to their spherical counterparts, opening new opportunities for drug delivery and vaccination. Up till now, electron microscopy is the only method to quantitatively identify the critical quality attributes (CQAs) of non-spherical particles produced by film-stretching; namely size, morphology and the quality of non-spherical particles (degree of contamination with spherical ones). However, electron microscopy requires expensive instrumentation, demanding sample preparation and non-trivial image analysis. To circumvent these drawbacks, the ability of different particle analysis methods to quantitatively identify the CQA of spherical and non-spherical poly(1-phenylethene-1,2-diyl (polystyrene) particles over a wide size range (40 nm, 2 µm and 10 µm) was investigated. To this end, light obscuration, image-based analysis methods (Microflow imaging, MFI, and Vi-Cell XR Coulter Counter) and flow cytometry were used to study particles in the micron range, while asymmetric flow field fractionation (AF4) coupled to multi-angle laser scattering (MALS) and quasi elastic light scattering (QELS) was used for particles in the nanometer range, and all measurements were benchmarked against electron microscopy. Results show that MFI can reliably identify particle size and aspect ratios of the 10 µm particles, but not the 2 µm ones. Meanwhile, flow cytometry was able to differentiate between spherical and non-spherical 10 or 2 µm particles, and determine the amount of impurities in the sample. As for the nanoparticles, AF4 coupled to MALS and QELS allowed the measurement of the geometric ($r_g$) and hydrodynamic ($r_h$) radii of the particles, as well as their shape factors ($r_g/r_h$), confirming their morphology. While this study shows the utility of MFI, flow cytometry and AF4 for quantitative evaluation of the CQA of non-spherical particles over a wide size range, the limitations of the methods are discussed. The use of orthogonal characterization methods can provide a complete picture about the CQA of non-spherical particles over a wide size range.

**Keywords**

Non-spherical particles; Flow cytometry (FACS); Microflow imaging (MFI); Asymmetric flow field flow fraction (AF4); Nano-rods

## 2. Introduction

Synthetic micro- and nanoparticulate systems are being extensively studied for biomedical applications, including therapy, monitoring, diagnosis and vaccination [1-3]. This is because these systems show a number of benefits, including the potential for passive or active targeting to different body or cell compartments [4], protection of sensitive therapeutic payloads (*e.g.* proteins or oligonucleotides) from degradation, and helping to increase compliance by longer dosing schedules [5, 6].

In contrast to particle size, charge and surface properties, particle geometry has been traditionally neglected in studying micro- and nanoparticles for biomedical use. This can be attributed to several reasons, including limitations in production processes, which usually result in spherical particles to reduce surface energy. Additionally, methods for particle characterization and assurance of homogeneity are rather limited. However, recently different production methods including soft lithography, mechanical stretching, templated self-assembly, nano-moulding and microfluidics, allow for the production of particles with different, non-spherical morphologies [7-12]. The possibility to obtain non-spherical particles created large interest in investigating the impact of particle shape on the interaction with biological systems [11, 13-15], with many interesting findings. For example, non-spherical particles are phagocytosed to a different extent compared to spherical ones, where ellipsoids exhibit a lower incidence of uptake by macrophages [16-18] while discs or oblate spheroids show an increased incidence of phagocytosis [19]. Additionally, Geng et al. observed that shape could alter the particle circulation time *in vivo* [20], as filamentous micelles persisted in the circulation of rodents for a week, nearly 10 times longer than their spherical counterparts [20]. These

observations show that particle shape can be an important design parameter for particulate drug delivery systems.

Despite these developments in producing and applying non-spherical micro- and nanoparticles, there are still very few methods for their analysis and characterization. At the moment, electron microscopy is the only analytical method used for the characterization of non-spherical particles [17]. Despite its strength, the method requires expensive instruments, laborious sample preparation and non-trivial image analysis [21]. Additionally, due to the broad size range and different possible shapes of non-spherical particles, it would be beneficial to identify different analytical methods which can cover several orders of magnitude of the possible size ranges [22, 23].

In this study, a number of different analytical methods were used to characterize non-spherical particles with different sizes and aspect ratios. For this purpose, 40 nm, 2 µm and 10 µm spherical polystyrene particles were stretched towards different aspect ratios using a film-stretching method[16]. Light obscuration particle counting (LO), image-based analysis methods (microflow imaging, MFI and Vi-Cell XR Coulter Counter) and flow cytometry were used to characterize particles in the micrometre range, while asymmetrical flow field flow fractionation (AF4) and dynamic light scattering (DLS) were used to characterize non-spherical particles in the nanometer range.

## 3. Materials and methods

### 3.1. Particles

Non-crosslinked 40 nm, 2 µm and 10 µm polystyrene (PS) particles were purchased from Polysciences (Eppelheim, Germany). Poly(1-hydroxyethylene) (Polyvinylalcohol 40–88 (PVA)) was purchased from Sigma–Aldrich (Steinheim, Germany). All other materials were of analytical grade.

### 3.2. Preparation of non-spherical particles

Ellipsoidal particles were prepared from spherical 40 nm, 2 µm and 10 µm polystyrene particles using the film stretching method in hot oil according to Champion et al.[7] Briefly, PVA was dissolved in water at 85 °C (10%, w/v), and then 2.5% of glycerol was added. To this solution, spherical polystyrene particles were added at a concentration of 0.08%, w/v. The mixture was poured into moulds and dried for 48 h at room temperature. The dried PVA/PS-particle film was cut into 3 cm × 2 cm sections and stretched using a manual device built in-house, consisting of two metal clamps attached to a screw which separates the two clamps during the stretching process. The films were stretched in an oil bath at 110 C at a constant stretching speed of 0.5 mm/s. After stretching, the film was cooled down to approximately 60 °C and washed with 100% 2-propanol (isopropanol).

### 3.3. Electron microscopy

Particle morphology was confirmed by SEM imaging using a JEOL JSM 6500F scanning electron microscope (Jeol Ltd., Tokyo, Japan) with Inca Software (Oxford instruments, Oxfordshire, UK). The samples were fixed with self-adhesive tape on aluminium stubs and were sputtered with carbon. SEM micrographs were collected at a magnification of 1000× for the 10 µm particles, 3000× for the 2 µm particles and 50,000× for the 40 nm particles. The diameters reported from the SEM micrographs are the Ferret diamaters of the particles to better express the particles' elongated shape.

### 3.4. Light obscuration

Light obscuration is usually used to measure particles in the range of 1–200 µm. The system measures an equivalent circular diameter of particles that pass a laser beam blocking light proportional to their cross-section area. The blocked

light is recorded by a photo diode [24]. Polystyrene particles were measured by light obscuration using a SVSS-C with a HCB-LD-25/25 sensor (PAMAS, Partikelmess- und Analysesysteme GmbH, Rutesheim, Germany). Triplicates of 0.3 ml of each sample were analyzed with a pre-run volume of 0.5 ml. Fill, rinse and emptying rate were set to 10 ml/min. The system was rinsed with 6 ml of high purified water prior to each run until particles counts of less than 50 particles/ml were reached.

## 3.5. Micro-flow imaging (MFI)

A micro-flow imaging system from Brightwell Inc. (Ottawa, Canada) was utilized to measure particle size and aspect ratio of different particle samples in triplicates. The system is usually used to analyze particles in the range of 1–500 µm. Particles pass a light source and are imaged by a camera. The image analyzing software offers information about particle's size and shape. [24]. In our study we used the Ferret diameter to analyze the particle size. A peristaltic pump was used to create constant particle streams. Sample volume was 1 ml. The system was calibrated with 5 µm polystyrene particles standard (Thermo Scientific, USA).

## 3.6. Vi-Cell XR Coulter Counter

A Vi-Cell XR Coulter Counter from Beckman Coulter GmbH (Krefeld, Germany) was utilized to measure particle size and aspect ratio of 10 µm polystyrene particles in triplicates. The Vi-Cell XR Coulter Counter measures an equivalent circular diameter of particles passing the camera of the system. The cell brightness level was set to 85%, cell sharpness to 100, viable cell spot brightness to 65%, viable cell spot area to 5%, decluster degree to medium, aspiration cycles to 1 and mixing cycles to 3.

### 3.7. Flow cytometry

A Bioscience flow cytometer FACS Canto II (Bioscience, Franklin Lakes, NJ, USA) equipped with forward- and side scattering laser was utilized. Detectors gain and sensitivity were optimized to maximize particle detection. All samples were measured in triplicates. For the 10 µm particles, the forward scatter detector (FSC) was set to 604 V and the side scatter (SSC) detector was set to 416 V, for the 2 µm particles FSC was set to 240 V, SSC to 270 V. The different particle solutions were diluted to 100.000 particles/ml before measurements using a PAMAS SVSS particle counter for concentration determination.

### 3.8. Asymmetric flow field flow fraction (AF4) system

A Wyatt Eclipse 2 AF4 system (Wyatt Technology, Dernbach Germany) combined with an Agilent 1100 HPLC system (Agilent Technologies, Palo Alto, USA) equipped with UV detection and a Wyatt Down Eos multi-angle laser light scattering (MALLS) detector. The AF4 technique can analyze particles in the range of 1 nm to 50 µm [24]. The Wyatt Quasi-Elastic-Light-Scattering (QELS) was utilized to analyze the hydrodynamic radius of particles. Measurement interval length was set to 2 s. The large separation channel was equipped with a 350 µm spacer and a 30 kDa cut-off regenerated cellulose membrane. 10 µl of 40 nm polystyrene particles of a 0.027% (w/w) solution were injected. Focusing period was 7 min with an applied focus flow of 2 ml/min. The detector flow was set to 0.2 ml/min, while the cross flow was held constant at 0.11 ml/min. The running buffer was composed of 0.5% SDS in water, and the pH was adjusted to 9.5. All samples were measured in triplicates. Particle diameters were calculated using the Astra software (version 5, Wyatt Technology).

### 3.9. Dynamic light scattering (DLS)

DLS experiments were performed using a Zetasizer Nano ZS equipped with a 633 nm He–Ne laser (Malvern, Herrenberg, Germany), which analyses the hydrodynamic radius of particles based on light intensity fluctuations of scattered laser light. One ml of polystyrene particle samples were measured in single use poly(methylmethacrylate) cuvettes (Brand, Wertheim, Germany) with a path length of 12.5 mm after an equilibration time of 120 s at 24 °C. Samples were analyzed in triplicates, each triplicate with 10 sub-runs. The average diameter and polydispersity were calculated by the Malvern Dispersion Technology software (version 4.20, Malvern, Herrenberg, Germany).

### 3.10. Calculation of the polydispersity index (PDI)

Except for DLS, the polydispersity index is calculated according to the following equation

$$PDI = (\sum_i M_i^2 N_i / \sum_i M_i N_i) / (\sum_i M_i N_i / \sum_i N_i)$$

where $M_i$ is a specific size fraction and $N_i$ is the number of events in a specific size fraction.

PDI for DLS measurements were reported by the software provided with the Zetasizer Nano ZS, which uses the following equation

$$PDI = \sigma^2/Z_D^2$$

where $\sigma$ is the standard deviation of the hypothetical Gaussian distribution and $Z_D$ is the intensity weighted $Z$ average mean diameter size.

## 4. Results

The film-stretching method was employed to produce ellipsoid particles, as this method is a powerful and simple technique to modify the shape of spherical

particles in the micro- and nanometer range. Additionally, it allows particle stretching in 1 or more dimensions simultaneously or in two subsequent steps, thereby making the production of a wide range of morphologies possible [7]. In this work, standard spherical polystyrene micro and nanoparticles were stretched twice (2x) or three times (3x) their original size, and then characterized using different particle characterization methods.

Electron microscopy was used to prove the successful stretching of the 40 nm, 2 μm and 10 μm particles, as can be seen in Figure II-1, where the stretched particles can easily be discerned from the non-stretched ones. Different elongations can also be measured using the microscope image analysis software, showing that indeed the 2x and 3x stretched particles have sizes quite close to the nominal values Table II-1. Additionally, stretching led to a decrease in the aspect ratio of the spherical particles from 1.0 to 0.18–0.31, depending on the stretching degree Table II-1. It was however possible to identify a small number of non-stretched particles (white arrows) in some batches of the produced non-spherical spheres, which raises the question about the degree of contamination of the produced non-spherical particles with spherical ones. Since electron microscopy requires demanding sample preparation and non-trivial image analysis, we set forward to test other analytical methods in order to evaluate their ability to deliver reliable quantitative information about the critical quality attributes (CQA) of the particles, namely size, morphology as well as the degree of contamination of the non-spherical particles. For this purpose, light obscuration, image-based particle analysis and flow cytometry were used for micron-sized particles, while DLS and AF4 were used for nanoparticles.
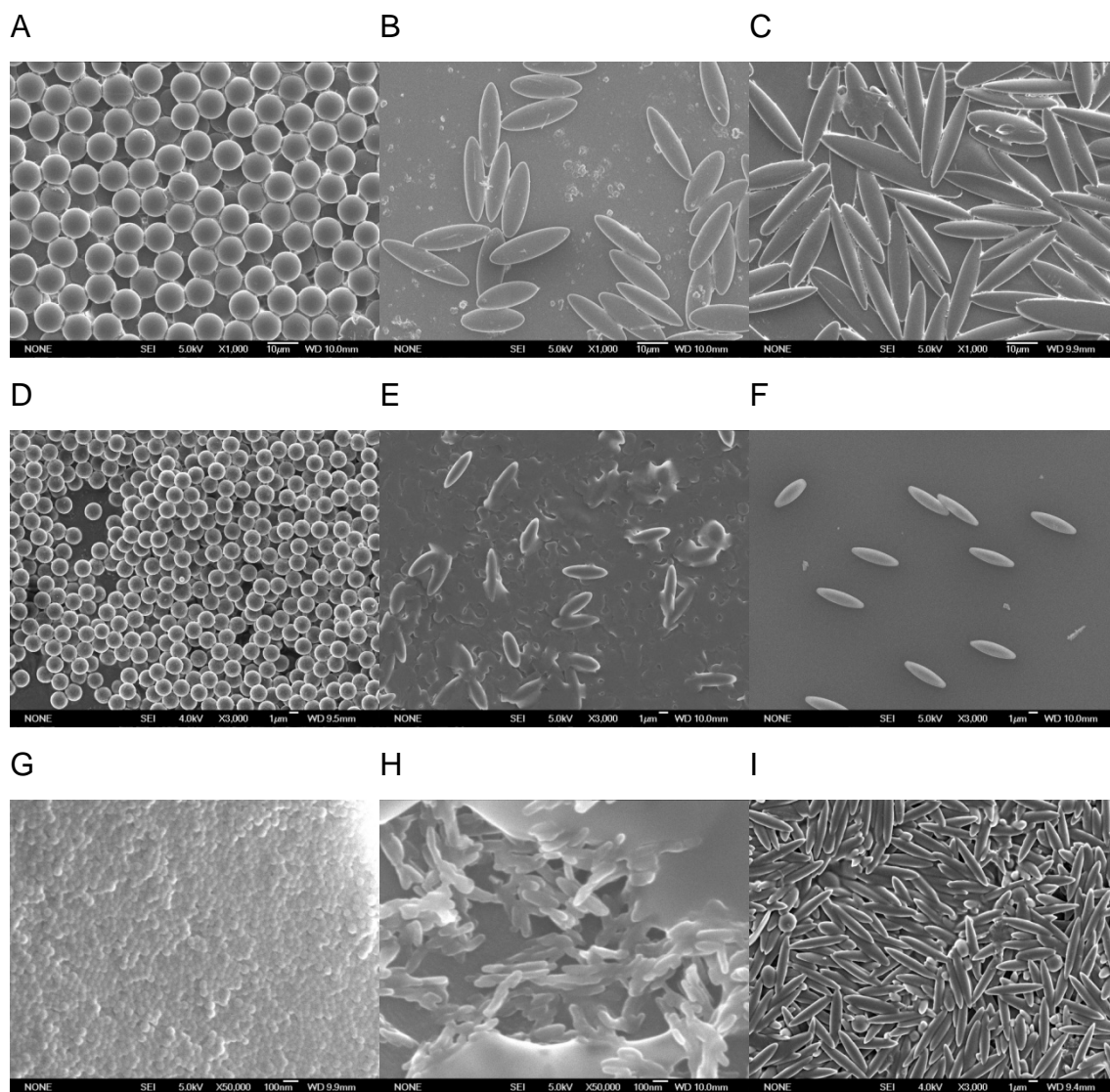
Figure II-1: SEM micrographs of differently sized and shaped polystyrene micro- and nanoparticles: (A) 10 µm spheres (1000× magnification), (B) 2× stretched, (C) 3× stretched particles, (D) 2 µm spheres (3000×), (E) 2× stretched, (F) 3× stretched, (G) 40 nm spheres (50,000×), (H) 40 nm 3× elongated (50,000×), and (I) 2 µm 3× stretched with spherical impurities.

Table II-1: Particle size and aspect ratio of spherical, 2X and 3X stretched 40 nm, 2 µm and 10 µm particles as determined from electron micrographs. (n=20)

| | Spheres Size | Aspect ratio | 2X stretched Size | Aspect ratio | 3X stretched Size | Aspect ratio |
|---|---|---|---|---|---|---|
| 40 nm | 40 nm ± 1.8 | 1 ± 0 | ------------ | ------------ | 207 nm ± 26 | 0.24 ± 0.02 |
| 2 µm | 2.2 µm ± 0 | 1 ± 0 | 4.3 µm ± 0.3 | 0.32 ± 0.02 | 5.7 µm ± 0.3 | 0.19 ± 0.03 |
| 10 µm | 10.1µm ± 0.1 | 1 ± 0 | 24.4 µm ± 1.4 | 0.20 ± 0.02 | 33.5 µm ± 2.7 | 0.26 ± 0.03 |

Prior to performing measurements on microparticles, the concentration of all samples was determined using the light obscuration-based SVSS-C PAMAS particle counter (LO), in order to perform all measurements at equal particle concentrations. Additionally, LO was used to determine particle size and particle size distribution. Results shown in Figure II-2 and Table II-2 demonstrate a slight increase in the mean particle diameter upon stretching, and a slight increase in the width of the size distribution. For instance, the PDI of 2 µm spheres increases from 1.04 to 1.093 for the 2× stretched and 1.085 for the 3× stretched particles. The PDI increases from 1.017 for the 10 µm spheres to 1.042 for the 2× stretched and 1.056 for the 3× stretched particles.

A

B

C
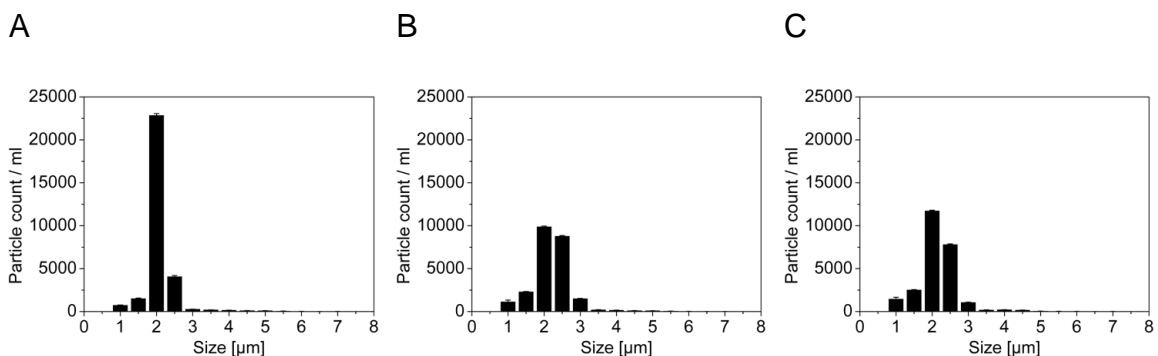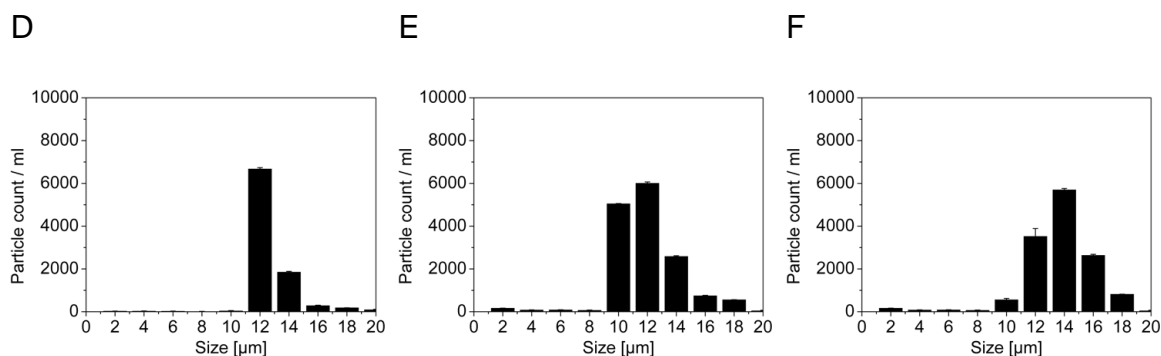
Figure II-2: Measurement of particle size and size distribution of 2 µm and 10 µm polystyrene microparticles using the SVSS-C PAMAS particle counter. (A-C) 2 µm: (A) spherical particles, (B) 2× stretched particles and (C) 3× stretched particles. (D-F) 10 µm: (D) spherical particles, (E) 2× stretched particles and (F) 3× stretched particles.

Table II-2: Mean particle size and polydispersity index (PDI) of the SVSS-C PAMAS particle counter of different polystyrene particles (results represented as mean ± standard deviation).

|  | Particle size (µm) | PDI |
|---|---|---|
| 2 µm spheres | 2.27 ± 0.00 | 1.042 |
| 2× stretched | 2.46 ± 0.01 | 1.093 |
| 3× stretched | 2.39 ± 0.01 | 1.085 |
| 10 µm spheres | 13.64 ± 0.03 | 1.017 |
| 2× stretched | 14.07 ± 0.04 | 1.042 |
| 3× stretched | 13.44 ± 0.01 | 1.056 |

Two image analysis-based instruments were also used for the characterization of the microparticles; namely the Vi-Cell XR Coulter Counter (Beckman Coulter GmbH) and the micro-flow imaging system (Brightwell Inc.). Both measurement methods are based on imaging a number of particles as they flow through a capillary, and thus, can deliver information about the particles' size and morphology. Images from Vi-Cell XR Coulter Counter show that changes in particle shape of the 10 µm particles can be identified (see images in Figure II-3). The Vi-Cell VR Coulter counter calculates particle size by counting the particle pixels and calculation of the theoretical diameter of a spherical particle.

This mean particle diameter as well as the polydispersity increase upon stretching as seen in
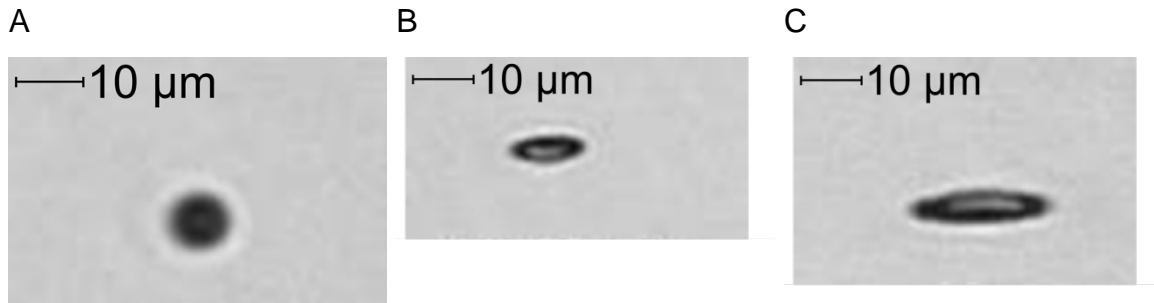


Figure II-3: Vi-cell Coulter counter images of (A) 10 µm spheres and its, (B) 2× stretched and (C) 3× stretched particles.
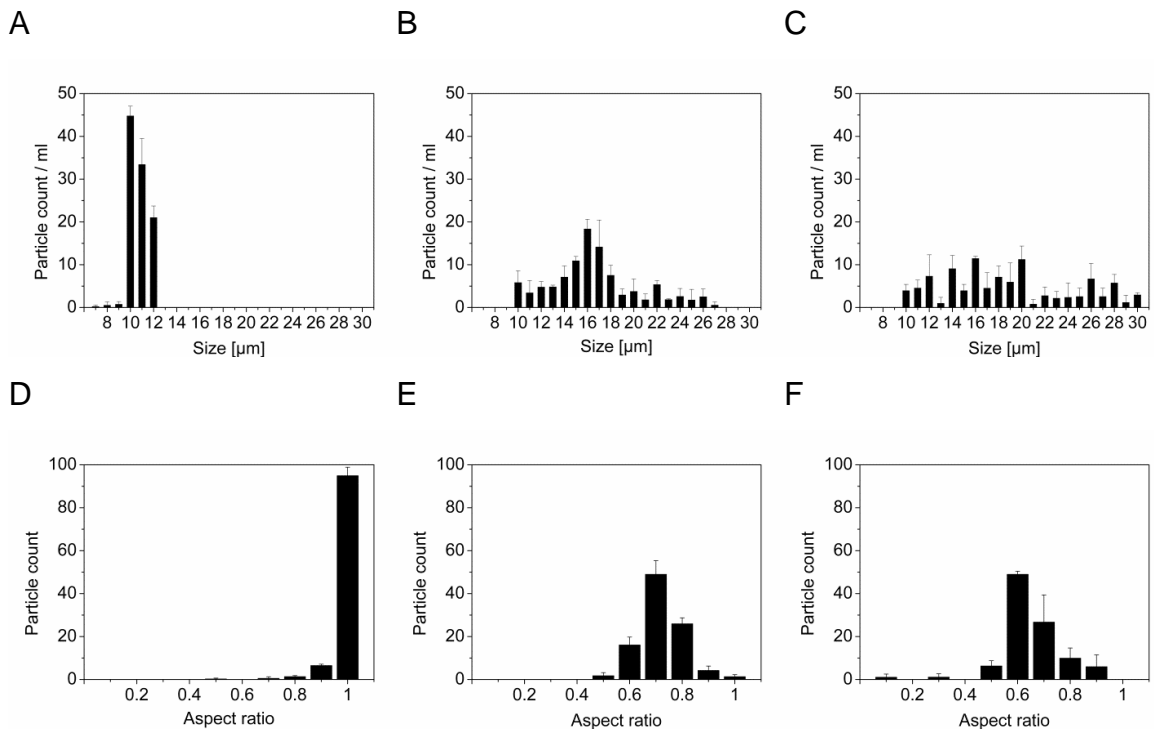


Figure II-4: Vi-Cell XR Coulter Counter measurement: mean diameter (left) and aspect ratio (right) of spheres (top), 2× stretched (middle) and 3× stretched (bottom) 10 µm polystyrene particles. Panels represent diameter of (A)

spherical, (B) 2× stretched, and (C) 3× stretched particles, as well as aspect ratio of (D) spherical, (E) 2× stretched and (F) 3× stretched particles

Table II-3: Mean particle size and PDI as measured by the Vi-Cell XR Coulter Counter for the 10 µm spherical, 2× and 3× stretched polystyrene particles (results represented as mean ± standard deviation).

|  | Particle size (µm) | PDI |
|---|---|---|
| 10 µm spheres | 10.72 ± 0.02 | 1.01 |
| 2× stretched | 16.64 ± 0.47 | 1.05 |
| 3× stretched | 18.80 ± 0.66 | 1.09 |

Results of the MFI measurements are shown in Figure II-5, Figure II-6, Figure II-7 and Figure II-8 and Table II-4. In this case, the diameter is expressed as maximum Ferret diameters (the longest dimension of the particle independent of its angular rotation at the time the image was captured), which represents a better description for ellipsoid particles compared to the equivalent sphere diameter used for Vi-Cell XR Coulter Counter. Results of the 10 µm spherical, 2× and 3× stretched particles show that indeed the particle Ferret diameter increases by stretching, while the aspect ratio decreases as seen in Figure II-5 and Figure II-7 and Table II-4, with results comparable to those obtained by SEM imaging (see Table II-1). Additionally, we further tested the ability of MFI to distinguish 10:90 and 50:50 mixtures of spherical:stretched particles as seen in Figure II-8. Results show a bimodal distribution with medians of the 2 peaks coinciding with the individual populations. Moreover, the particle concentrations in the mixture are in agreement with the set concentrations (determined by LO before mixing), where the 10:90 mixture (spheres:stretched) was found to be 14:86 by MFI, and the 50:50 mixture was 46:54.
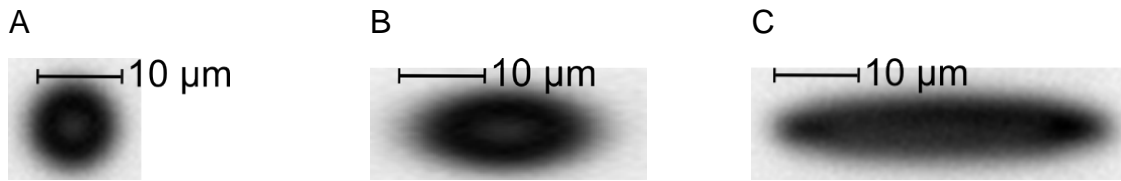
Figure II-5: Micro flow images of (A) spheres, (B) 2× stretched particles, and (C) 3× stretched particles.



Figure II-6: (A) Grey scale, and (B) binary image of a 2 µm 3× stretched particle.
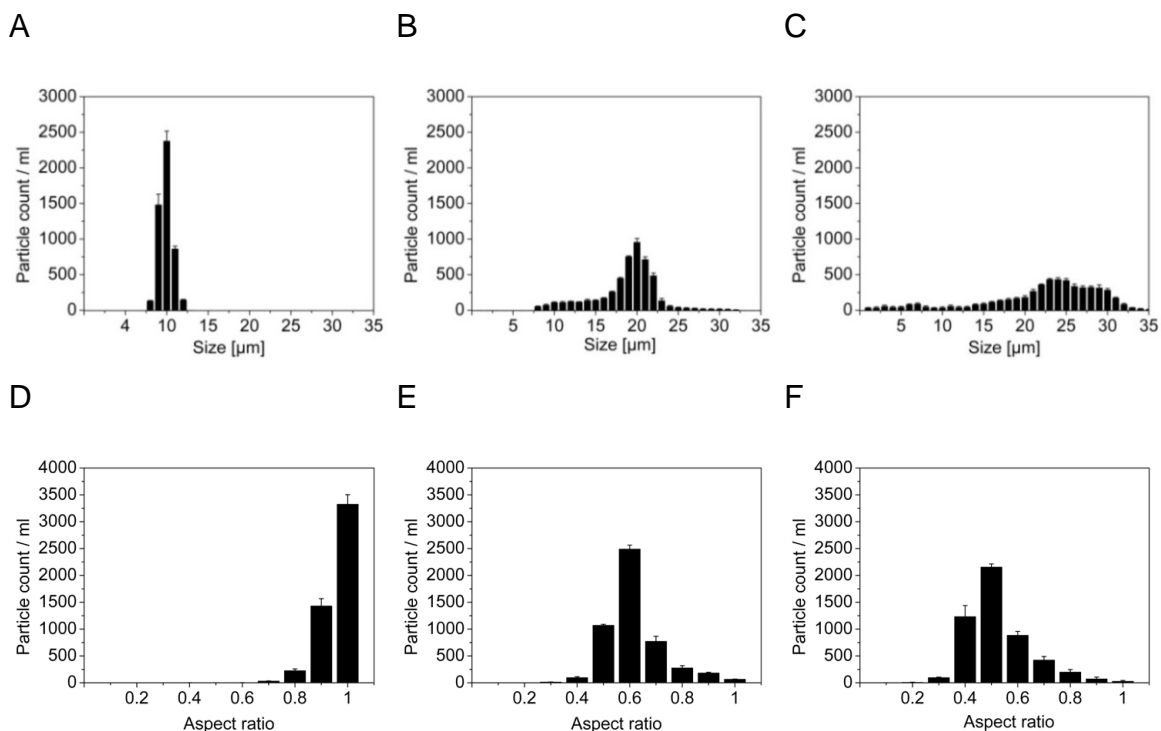


Figure II-7: MFI measurements: The mean Ferret diameter and aspect ratio of spheres, 2× stretched and 3× stretched 10 µm polystyrene particles. Spherical particles have an aspect ratio of 1 elongated particles of <1. (a–c) Ferret diameter: (a) spherical particles, (b) 2× stretched particles and (c) 3× stretched.

(d–f) aspect ratio: (d) spherical particles, (e) 2× stretched particles and (f) 3×
stretched particles.

A



B



C



D
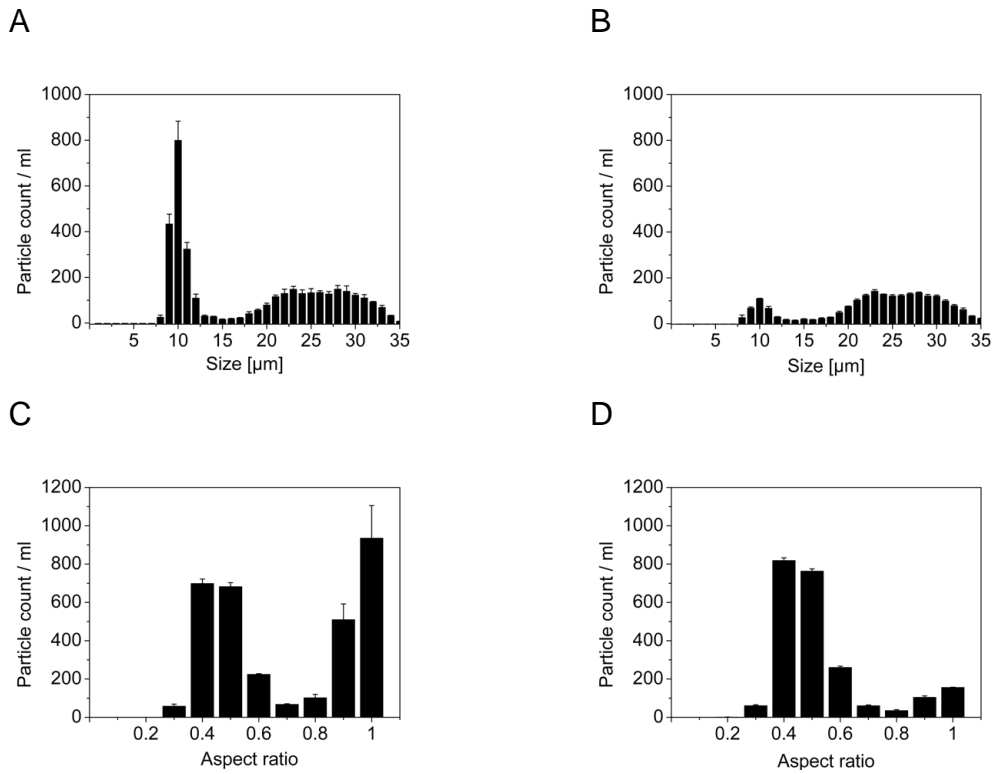


Figure II-8: MFI measurements: Mean ferret diameter and aspect ratio of
mixtures of 10 µm polystyrene spheres and 3× stretched particles. (a and b)
Ferret diameter: (a) 10% spheres/90% 3× stretched particles, (b) 50%
spheres/50% 3× stretched. (c and d) aspect ratio: (c) 10% spheres/90% 3×
stretched particles, (d) 50% spheres/50% 3× stretched.

Table II-4: Mean Ferret diameter and PDI as determined by MFI measurements
for the 10 µm spherical, 2× and 3× stretched polystyrene particles (results
represented as mean ± standard deviation).

|  | Ferret diameter (µm) | PDI |
|---|---|---|
| 10 µm spheres | 9.88 ± 0.08 | 1.01 |
| 2× stretched | 18.69 ± 0.32 | 1.04 |
| 3× stretched | 23.59 ± 0.83 | 1.05 |

It is worth noting that both instruments did not deliver meaningful results for the stretched 2 µm particles. This is because these methods can provide reliable image analysis in the range of 1–50 µm for spherical particles [23], but lack resolution to describe particle geometry in the lower µm range (see Figure II-6).

Additionally flow cytometery was used to analyze spherical and stretched microparticles, because its ability to analyze 0.5–20 µm particles had been reported previously [25]. However, the instrument's ability to distinguish/recognize particle shape has never been reported before. Our results show that the flow cytometer has an even superior ability to differentiate between spherical and non-spherical particles compared to the image-based analyzers. Results from Figure II-9 show that spherical 2 µm particles are expressed as a reproducible discrete population on dot plots, with relatively low forward and side scattering. Meanwhile, the analysis of the stretched particles show a significant increase in side and especially forward scatter, allowing precise identification of the particles, so that very small populations of impurities (non-stretched spherical particles among stretched ones) can be detected and quantified. Thereby the method can be used to describe the quality of stretched particles comprehensively. In the highest quality produced batches, less than 1% of non-stretched spherical contaminants were observed. Very similar results were obtained for the 10 µm spherical and stretched particles (data not shown).
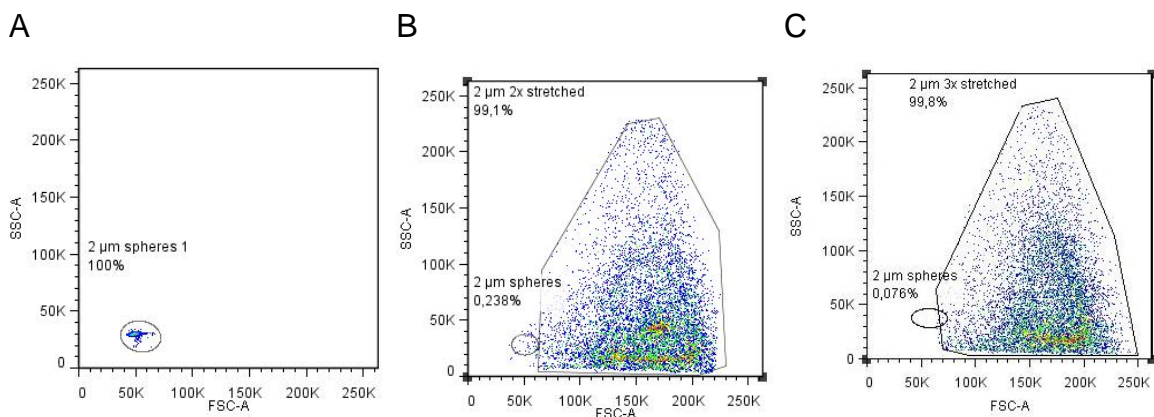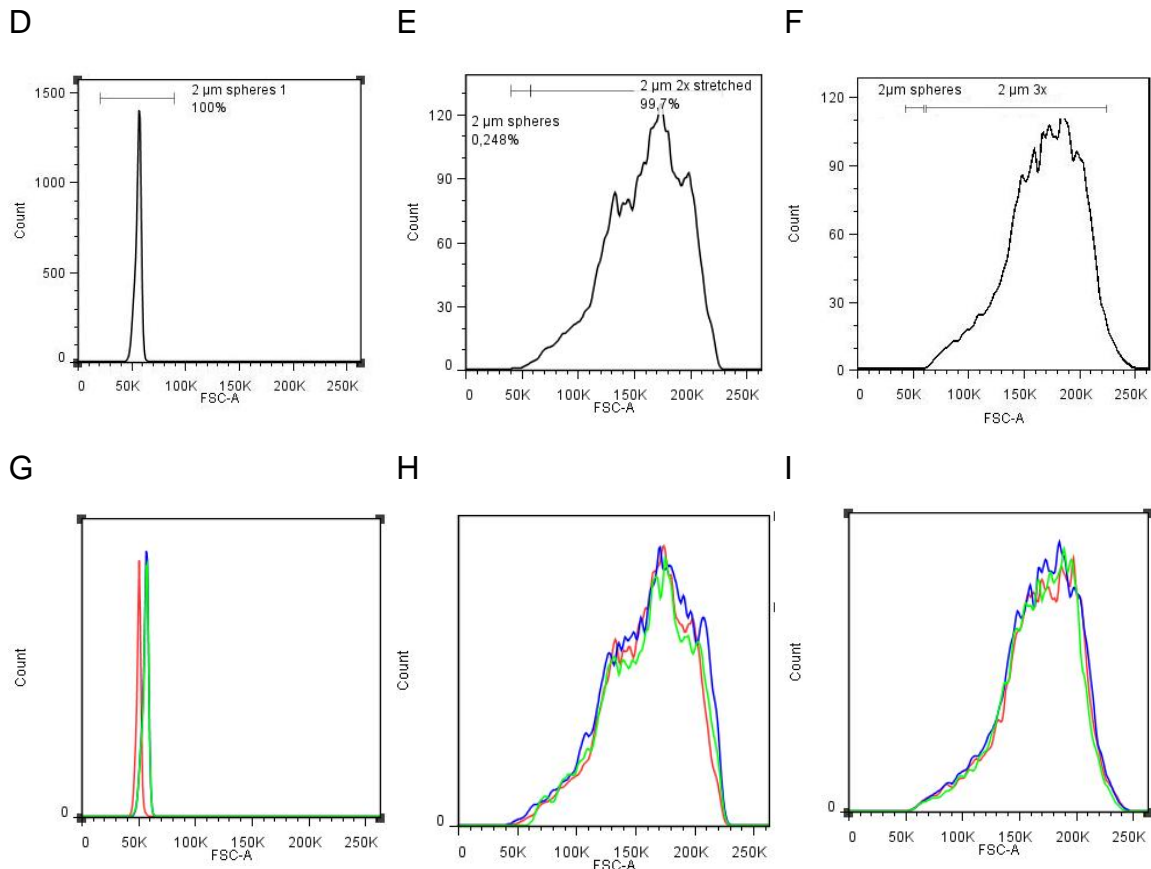
Figure II-9: Flow cytometry measuremnts: Density dot plots and histograms of 2 µm spherical and stretched polystyrene particles. (A-C) Density plots: (A) 2 µm spherical particles, (B) 2 µm 2× stretched particles, (C) 2 µm 3× stretched particles. (D-F) Histograms: (D) 2 µm spherical particles, (E) 2 µm 2× stretched particles and (F) 2 µm 3× stretched particles (G-I) overlays of histograms: (G) 2 µm spherical particles, (H) 2 µm 2× stretched particles and (I) 2 µm 3× stretched particles.

In order to validate the method, different mixtures of known concentrations of spherical and stretched particles were measured using flow cytometry. As described earlier, concentrations of spheres and stretched particles were determined using a LO particle counter, and the mixtures were adjusted to contain 50 or 10% of the spherical particles. As seen in Figure II-10, it is possible to detect small populations of differently shaped particles in mixtures of

spheres and stretched particles, and the measured proportions coincide with the expected ratios measured with light obscuration.
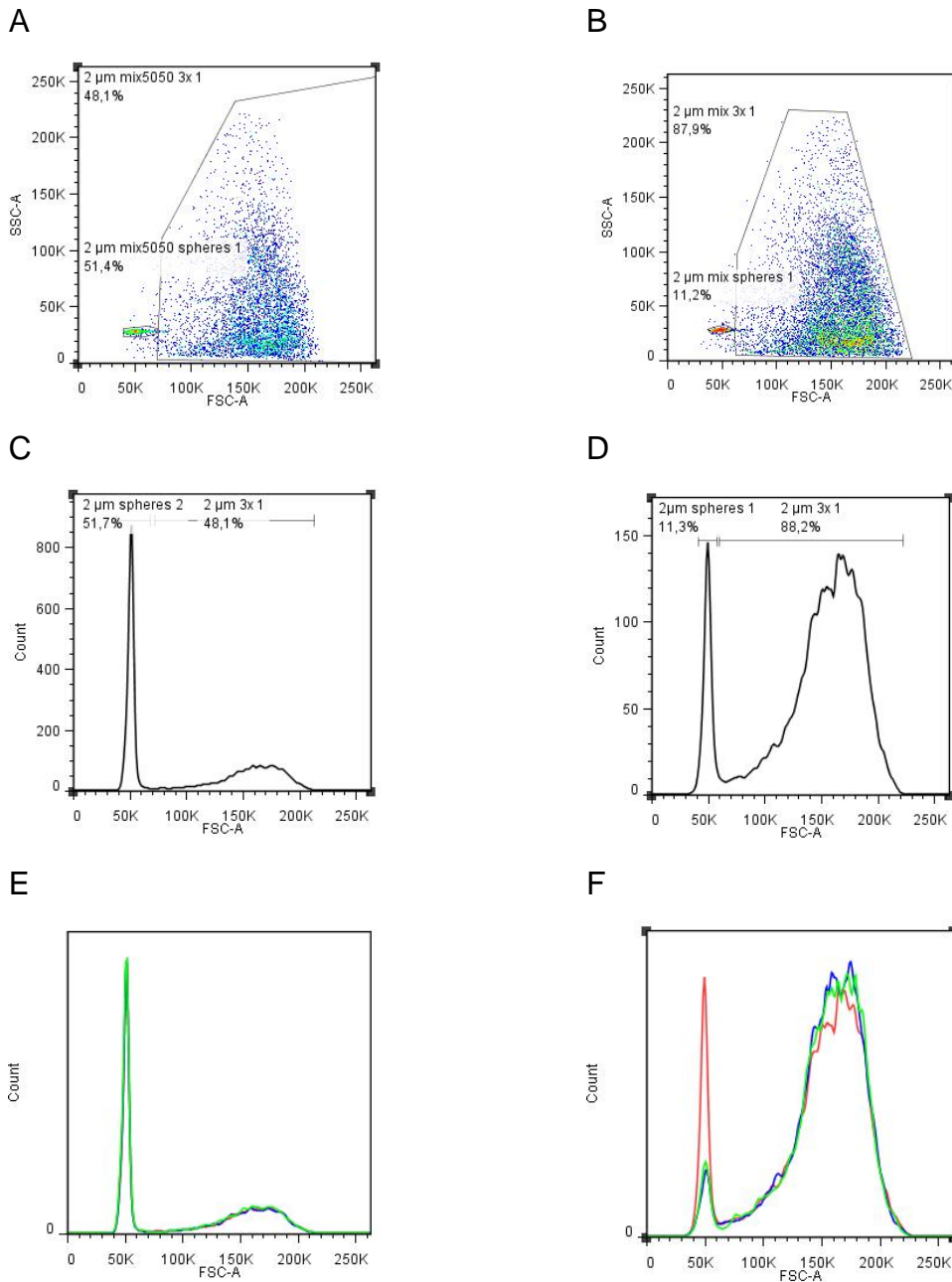


Figure II-10: Density dot plots and histograms of mixtures of spherical and 3× stretched particles. (A and B) density dot plots: (A) 2 µm 50% spherical/50% 3× stretched, (B) 2 µm 10% spherical/90% 3× stretched. (C and D) Histograms: (G) 2 µm 50% spherical/50% 3× stretched, (H) 2 µm 10% spherical/90% 3×

stretched. (E and F) overlays of histograms: (E) 2 μm 50% spherical/50% 3×
stretched, (F) 2 μm 10% spherical and 90% 3× stretched.


For the evaluation of nanoparticles, the AF4 instrument coupled to multi-angle
light scattering (MALS) and quasi-elastic light scattering (QELS) was employed,
where the AF4 is used to separate particles, while QELS measures their
hydrodynamic radius, and MALS measures their radius of gyration (geometric
radius). The chromatograms show clear differences between the 40 nm
spherical and 3× stretched particles, where the chromatograms of the stretched
particles show a relatively broad peak with extensive tailing, contrary to the
symmetric peak of the spherical ones. By examining the measured radii of the
main peaks, the hydrodynamic radius increases slightly after particle stretching,
while the radius of gyration increases dramatically as seen in Figure II-11. The
changes in the hydrodynamic radius observed by the AF4 measurements were
confirmed with the Malvern Zetasizer (Table II-5), where the spherical particles
showed a 19.8 nm radius, while the stretched particles show an apparent radius
of 136.2 nm, quite close to the QELS results seen in Figure II-11b. Results of
the quotient of the geometric radius to the hydrodynamic radius also show clear
differences between the different particles [26], as it is equal to 0.96 in case of
the spherical particles and 1.89 for the 3× stretched ones.
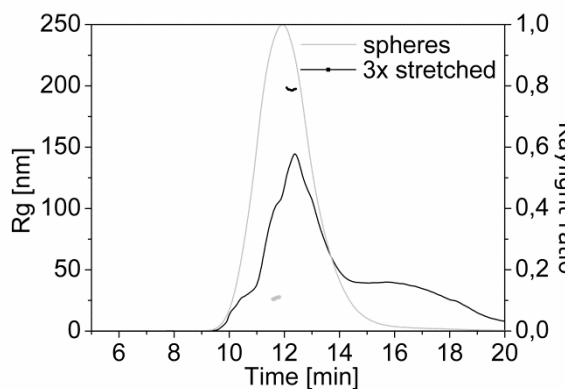
A                                              B
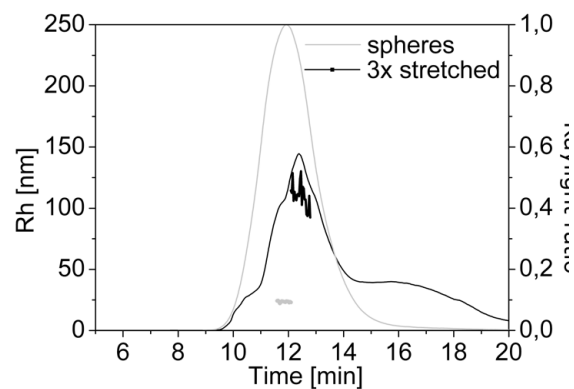
Figure II-11: Chromatograms of 40 nm spheres and 3x stretched polystyrene particles including (A) geometric radius and (B) hydrodynamic radius. Arrows show the difference in radius of spheres (grey) and 3x stretched (black) particles: (A) geometric radius, (B) hydrodynamic radius.

Table II-5: Hydrodynamic radius and PDI of 40 nm spheres and 3x stretched polystyrene particles as determined by DLS (results represented as mean ± standard deviation).

|  | Hydrodynamic radius (nm) | PDI |
|---|---|---|
| 40 nm spheres | 19.8 ± 0.04 | 0.1 ± 0.00 |
| 40 nm 3x stretched | 136.2 ± 8.12 | 0.42 ± 0.19 |

## 5. Discussion

Non-spherical particles are developing into an interesting research field, showing important effects for particle shape on the interaction of micro- and nanoparticles with biological systems [17]. Among the different methods for non-spherical particle production, the film stretching method is a simple and powerful method for producing particles with different shapes [17]. Indeed, using this method allowed the production of rod-like micro- and nanoparticles with different aspect ratios, as shown by electron microscopy Figure II-1. In some electron micrographs, the presence of a few spherical contaminants in the stretched particles was observed (Figure II-1). To evaluate the CQA of non-spherical particles, namely size, shape and degree of contamination with spherical ones, and simultaneously circumvent the laborious and expensive SEM sample preparation and the non-trivial image analysis [21], we tested different particle characterization methods for their ability to deliver quantitative information about the CQA using routine quality control methods. For micron-sized particles, light obscuration (PAMAS), image-based particle analysis (Vi-Cell XR Coulter Counter and MFI) as well as flow cytometry were used to investigate the particle size and shape of those particles.

The PAMAS particle counter is a very fast and easy-to-handle instrument to count particles in the micrometre range, and it can precisely determine particle concentrations of spherical and stretched particles. Accordingly, it was used prior to all experiments to adjust particle concentrations. The value of the LO method as a particle counter could be confirmed by delivering the same particle concentrations and respective ratios in the flow cytometer and MFI experiments. However, light obscuration did not provide reliable information about particle size or shape for the non-spherical particles. This is due to its measurement principle, which relates the intensity of the blocked light to particle size, and accordingly cannot actually determine particle geometry. On average, the stretched particles deliver about the same light obscuration areas when moving through the detector in a statistically distributed orientation.

Two image analysis instruments were used for particle characterization in this study, namely Vi-Cell XR Coulter Counter and MFI. The former analyses 30–150 particles/run, while the MFI can measure and analyze 150–5000 particles/run, which leads to a dramatic enhancement of statistical analysis and reduction of scatter (compare Figure II-4 for Vi-Cell XR Coulter Counter *vs.* Figure II-6 for MFI). Our results show that for particles ≥10 µm, the particle size and geometry of the particles can be reliable analyzed using MFI, and to a lesser extent with the Vi-Cell XR Coulter. In the range of 2 µm, spherical particles can be analyzed in size by both instruments, but the resolution is not high enough to detect the geometry of a stretched particle. It is worth noting that the determined Ferret diameters in MFI are smaller than the dimensions determined by SEM. This is because elongated particles flowing in a tube show a distribution of orientations with respect to the flow direction depending on particle size, aspect ratio, flow rate and dimensions of the capillary [27, 28]. This leads to an averaged Ferret dimension lower than the actual value.

Flow cytometry was also used in this study to examine particles with different shapes. Previous reports describe the use of flow cytometry for particle examination, such as the investigation of protein aggregates [29] as well as silicon oil contamination of protein formulations [30]. To the best of our

knowledge, this is the first report on using the flow cytometer to differentiate between spherical and non-spherical micro and nanoparticles. The flow cytometer is a single particle measurement method, which can analyze large samples of 0.5–100 µm in very short time frames (up to 5000 particles/s) [25]. By examining flow cytometry dot plots for forward and side scatter, spherical particles are found as small homogenous populations with relatively low scatter. This homogeneity is probably due to the isotropicity of the spherical particles, leading to a nearly identical scattering pattern for all the particles. In contrast, the non-spherical particles are anisotropic, leading to different scattering pattern for each particle depending on the orientation of the particle with respect to the incident light beam. Accordingly, non-spherical particles appear as a "cloud" rather than a homogeneous "spot" on the dot plot, with a shift towards higher forward and side scatter (see Figure II-9 and Figure II-10). These results allowed the differentiation between the two particle populations, as well as the determination of the two populations in preformed mixtures, and the levels of spherical contaminants (Figure II-10).

In the nanometer range, we used the asymmetrical flow field flow fraction (AF4) coupled to QELS and MALS to analyze spherical and non-spherical particles, where the geometric radius was analyzed using MALS, while the hydrodynamic radius was investigated by online QELS measurements. Gajdos and Brenner [26] carried out a theoretical analysis for field-flow-fractionation (FFF) of non-spherical particles proving that the method can separate particles based on geometry, however, the experimental proof is rare particularly in the nanometer range. Chromatograms of 40 nm spherical and 3× stretched particles show differences in elution times as well as in the measured radii. One can use the shape factor (the quotient of the geometric radius to the hydrodynamic radius) to estimate particle shape, where it is equal to 0.778 in the case of hard spheres, 0.977 for soft spheres, and ~2 for rod like structures [31]. Our spherical particles have a shape factor of 0.96, nearly identical to the reported values of similar sized spherical nanoparticles, while a value of 1.8 confirms the rod-like morphology of the 3× stretched particles. The AF4 method is, however,

limited by the resolution of the used QELS detector, which can only measure in the range from 3 to 200 nm depending on the detector flow rate.

Comparing the methods for the quantitative characterization of non-spherical microparticles, each method has its strengths and weaknesses. For instance, electron microscopy provides excellent images for the determination of particle size and shape over a wide range of sizes in the micro- and nanometer scale, but requires expensive instrumentation, demanding sample preparation and non-trivial image analysis. LO is a very good method for determining particle concentration, but is not able to accurately determine particle size or shape of elongated particles. The Vi-Cell XR Coulter Counter identified changes in particle shape and morphology, but could not provide reliable results because of the low number of the measured particles. MFI provides excellent results for particles ≥10 µm, but not for the 2 µm particles. Flow cytometry is a powerful tool in differentiating between spherical and non-spherical particles and determining minor amounts of spherical contaminants in non-spherical particles for both 2 and 10 µm spheres, but it cannot determine particle size. AF4 is the only method in the nanometer range to directly analyze particle shape, with the help of the shape factor, but requires demanding method development.

## 6. Conclusion

In conclusion, the current study shows the utility of MFI, FACS as additional methods for determining the CQA of non-spherical microparticles, and can be used for routine measurements for industrial scale quality control. In contrast to SEM imaging, they can rapidly analyze not only small fractions, but also larger samples and obtain quantitative statistically valuable information. On the other hand, AF4 allows the evaluation of size and morphology of non-spherical nanoparticles, proving the high flexibility of this technique. Finally, the use of orthogonal methods can guarantee an optimal characterization of non-spherical particles

## 7. Acknowledgements

## 8. References

1.	Fifis, T., et al., Short peptide sequences containing MHC class I and/or class II epitopes linked to nano-beads induce strong immunity and inhibition of growth of antigen-specific tumour challenge in mice. Vaccine, 2004. 23(2): p. 258-266.
2.	Langer, R., New methods of drug delivery. Science, 1990. 249(4976): p. 1527-1533.
3.	Yang, L., et al., Receptor-Targeted Nanoparticles for In vivo Imaging of Breast Cancer. Clinical Cancer Research, 2009. 15(14): p. 4722-4732.
4.	Cho, K., et al., Therapeutic Nanoparticles for Drug Delivery in Cancer. Clinical Cancer Research, 2008. 14(5): p. 1310-1316.
5.	Besheer, A., et al., Characterization of PLGA Nanospheres Stabilized with Amphiphilic Polymers: Hydrophobically Modified Hydroxyethyl Starch vs Pluronics. Molecular Pharmaceutics, 2009. 6(2): p. 407-415.
6.	Owens III, D.E. and N.A. Peppas, Opsonization, biodistribution, and pharmacokinetics of polymeric nanoparticles. International Journal of Pharmaceutics, 2006. 307(1): p. 93-102.
7.	Champion, J.A., Y.K. Katare, and S. Mitragotri, Making polymeric micro- and nanoparticles of complex shapes. Proceedings of the National Academy of Sciences, 2007. 104(29): p. 11901-11904.
8.	Dendukuri, D., et al., Continuous-flow lithography for high-throughput microparticle synthesis. Nature Materials, 2006. 5(5): p. 365-369.
9.	Manoharan, V.N., M.T. Elsesser, and D.J. Pine, Dense Packing and Symmetry in Small Clusters of Microspheres. Science, 2003. 301(5632): p. 483-487.
10.	Merkel, T.J., et al., Scalable, Shape-Specific, Top-Down Fabrication Methods for the Synthesis of Engineered Colloidal Particles. Langmuir, 2009. 26(16): p. 13086-13096.
11.	Mitragotri, S. and J. Lahann, Physical approaches to biomaterial design. Nature Materials, 2009. 8(1): p. 15-23.
12.	Rolland, J.P., et al., Direct fabrication and harvesting of monodisperse, shape-specific nanobiomaterials. Journal of the American Chemical Society, 2005. 127(28): p. 10096-10100.
13.	Decuzzi, P., et al., Intravascular Delivery of Particulate Systems: Does Geometry Really Matter? Pharmaceutical Research, 2009. 26(1): p. 235-243.

14. Simone, E.A., T.D. Dziubla, and V.R. Muzykantov, Polymeric carriers: role of geometry in drug delivery. Expert Opinion on Drug Delivery, 2008. 5(12): p. 1283-1300.

15. Yoo, J.-W., et al., Bio-inspired, bioengineered and biomimetic drug delivery carriers. Nature Reviews Drug Discovery, 2011. 10(7): p. 521-535.

16. Champion, J. and S. Mitragotri, Shape Induced Inhibition of Phagocytosis of Polymer Particles. Pharmaceutical Research, 2009. 26(1): p. 244-249.

17. Champion, J.A., Y.K. Katare, and S. Mitragotri, Particle shape: A new design parameter for micro- and nanoscale drug delivery carriers. Journal of Controlled Release, 2007. 121(1-2): p. 3-9.

18. Champion, J.A. and S. Mitragotri, Role of target geometry in phagocytosis. Proceedings of the National Academy of Sciences of the United States of America, 2006. 103(13): p. 4930-4934.

19. Sharma, G., et al., Polymer particle shape independently influences binding and internalization by macrophages. Journal of Controlled Release, 2010. 147(3): p. 408-412.

20. Geng, Y., et al., Shape effects of filaments versus spherical particles in flow and drug delivery. Nat Nanotechnol, 2007. 2(4): p. 249-55.

21. Vermant, J., H. Yang, and G.G. Fuller, Rheooptical determination of aspect ratio and polydispersity of nonspherical particles. AIChE Journal, 2001. 47(4): p. 790-798.

22. Narhi, L.O., et al., A Critical Review of Analytical Methods for Subvisible and Visible Particles. Current Pharmaceutical Biotechnology, 2009. 10(4): p. 373-381.

23. Singh, S.K., et al., An industry perspective on the monitoring of subvisible particles as a quality attribute for protein therapeutics. Journal of Pharmaceutical Sciences, 2010. 99(8): p. 3302-3321.

24. Zölls, S., et al., Particles in therapeutic protein formulations, Part 1: Overview of analytical methods. Journal of Pharmaceutical Sciences, 2012. 101(3): p. 914-935.

25. Mach, H., et al., The use of flow cytometry for the detection of subvisible particles in therapeutic protein formulations. Journal of Pharmaceutical Sciences, 2011. 100(5): p. 1671-1678.

26. Gajdos, L.J. and H. Brenner, Field-Flow Fractionation: Extensions to Nonspherical Particles and Wall Effects. Separation Science and Technology, 1978. 13(3): p. 215-240.

27. Bernstein, O. and M. Shapiro, Direct determination of the orientation distribution function of cylindrical particles immersed in laminar and turbulent shear flows. Journal of Aerosol Science, 1994. 25(1): p. 113-136.

28. Gunes, D.Z., et al., Flow-induced orientation of non-spherical particles: Effect of aspect ratio and medium rheology. Journal of Non-Newtonian Fluid Mechanics, 2008. 155(1–2): p. 39-50.

29. Barnard, J.G., et al., Subvisible particle counting provides a sensitive method of detecting and quantifying aggregation of monoclonal antibody caused by freeze-thawing: Insights into the roles of particles in the

protein aggregation pathway. Journal of Pharmaceutical Sciences, 2011. 100(2): p. 492-503.

30.     Ludwig, D.B., et al., Flow cytometry: A promising technique for the study of silicone oil-induced particulate formation in protein formulations. Analytical Biochemistry, 2011. 410(2): p. 191-199.

31.     Brewer, A. and A. Striegel, Particle size characterization by quadruple-detector hydrodynamic chromatography. Analytical & Bioanalytical Chemistry, 2009. 393(1): p. 295-302.

# III. Chapter 3

## Lesson learned: Shape characterization of differently shaped nanoparticles by asymmetric flow field flow fractionation

In a first step the robust film-stretching method was established to produce non-spherical micro- and nanoparticles (Chapter 2). Several methods were applied to characterize non-spherical micro-and nanoparticles (Chapter 2). Following the AF4 method was utilized to separate spherical and non-spherical nanoparticles. The aim was to use the AF4 method to obtain a pure sample of non-spherical nanoparticles. During the method development we realized that our non-spherical particles are susceptible for aggregation (properly during the focus step). Therefore, the AF4 method was an inadequate method to achieve this goal and this chapter was finally not published. Particle aggregation during the focus step is a typical AF4 problem.

## 1. Introduction

Despite promising approaches to fabricate and apply non-spherical nanoparticles, electron microscopy is usually the only analytical method used at the moment to characterize non-spherical particles [1]. Electron microscopy has several drawbacks, namely high costs, time consuming sample preparation and non-trivial image analysis [2].

In this study, non-spherical particles were fabricated using the film stretching method [3]. AF4 coupled with multi-angle-laser-light-scattering (MALLS) and quasi-elastic-light-scattering (QELS) detection was utilized to characterize 20 nm polystyrene spherical and non-spherical nanoparticles. The AF4 system was used to separate populations of different particle geometries, which were analyzed using the two detectors to characterize the particle shape factor. The analysis of the particle size revealed particle aggregation of the non-spherical particles (most likely during the focus step). Particle up-concentration and aggregation during the AF4 focus step is a common problem [4]. Surprisingly, only the non-spherical particles showed aggregation. Therefore, the used AF4 method was not capable to analyze the shape of our non-spherical nanoparticles.

## 2. Materials and Methods

### 2.1. Materials

Poly (vinyl alcohol) (PVA) 40-88 was purchased from Sigma Aldrich (Steinheim, Germany). 20 nm non-cross-linked and 500 nm cross-linked polystyrene (PS) particles were purchased from Polyscience (Eppenheim, Germany). All other materials were of analytical grade.

## 2.2. Non-spherical particle preparation

The film stretching method established by Champion et al. [3] was used to prepare ellipsoid particles from 20 nm polystyrene spheres. Briefly, PVA (10% w/w) and glycerol (2% w/w) were dissolved in water at 85°C, then polystyrene spheres concentrated at 0.1% (w/w) were added. The dispersion was filled into polymethylmethacrylat molds and dried at room temperature for 48 h. PVA / PS particle film sections of 3 x 2 cm were stretched in a manual tool built in-house, consisting of a screw which separates two clamps during stretching at a constant speed of 0.5 mm/s. During stretching, the film was immersed in an oil bath at 110°C. After stretching, the oil bath was first cooled down to 60°C; then films were recovered and washed with 100% isopropanol by three centrifugation steps at 40000 rpm.

## 2.3. Transmission electron microscopy (TEM)

Samples were prepared using the following protocol: 2% of an aqueous solution of phosphotungstic acid (PTA), pH 7.4, was mixed in equal quantities with the nanoparticle dispersion. Of this mixture, 2 µl were placed on a carbon-coated copper grid (Plano, Wetzlar, Germany). Grids were dried for 20 s [5] at room temperature. Transmission electron micrographs were acquired using a FEI Titan electron microscope (Hillsboro, Oregon) at an acceleration voltage of 80 kV.

## 2.4. Asymmetrical flow field flow fraction (AF4)

A Wyatt Eclipse 2 AF4 system (Wyatt Technology, Dernbach Germany) with an Agilent 1100 HPLC system (Agilent Technologies, Palo Alto, USA) equipped with a Wyatt Dawn Eos multi-angle laser light scattering (MALLS) detector and the Wyatt Quasi-Elastic-Light-Scattering (QELS) was used to analyze the radius of spheres and elongated particles. Detector voltage was manually reduced by

the factor 100 by jumpers to increase particle concentration for light scattering analysis. The large separation channel was equipped with a wide 350 µm spacer and a 10 kDa cut-off regenerated cellulose membrane (Wyatt Technology, Dernbach Germany). Following, 5 µl of 20 nm polystyrene particle dispersion (concentration 0.027% w/w) were injected. The detector flow was set to 0.1 ml/min and cross flow to 0.2 ml/min. The running buffer consisted of 0.5% sodium dodecyl sulfate (SDS) in highly purified water and the pH was adjusted with NaOH to 9.5. All particle size calculations were performed using the Astra software (version 5 Wyatt Technology, Dernbach Germany). Particle samples were analyzed using the following settings: 5 detectors: 3, 13 and 16-18 of the total 18 detectors were excluded analyzing geometric radius with the Wyatt Dawn Eos MALLS. Reliable particle radius-analysis was achieved investigating a broad area in the peak middle with high particle concentrations. Radius measurements were not manipulated by curve fitting.

## 2.5. Dynamic Light Scattering (DLS)

The Zetasizer Nano ZS equipped with a 633 nm He-Ne laser (Malvern, Herrenberg, Germany) was utilized to perform DLS measurements. After an equilibration step of 120 sec at 24°C, one ml sample was measured in water in triplicates in a poly(methylmethacrylate) cuvette (Brand, Wertheim, Germany). The Malvern Dispersion Technology software (version 4.20, Malvern, Herrenberg, Germany) was used to calculate average diameter and polydispersity.

## 3. Results

The powerful and simple film-stretching method was utilized to fabricate ellipsoid particles. It has the capacity to produce particles in a wide variety of shapes in the micro- and nanometer range [1, 3]. In this work we stretched the

20 nm polystyrene particles three fold to create ellipsoid rod-like particles and then characterized them with TEM and the AF4 system.

It was possible to find several ellipsoid 20 nm particles with TAM (Figure III-1), where stretched particles can clearly be discriminated from spheres.

A

B
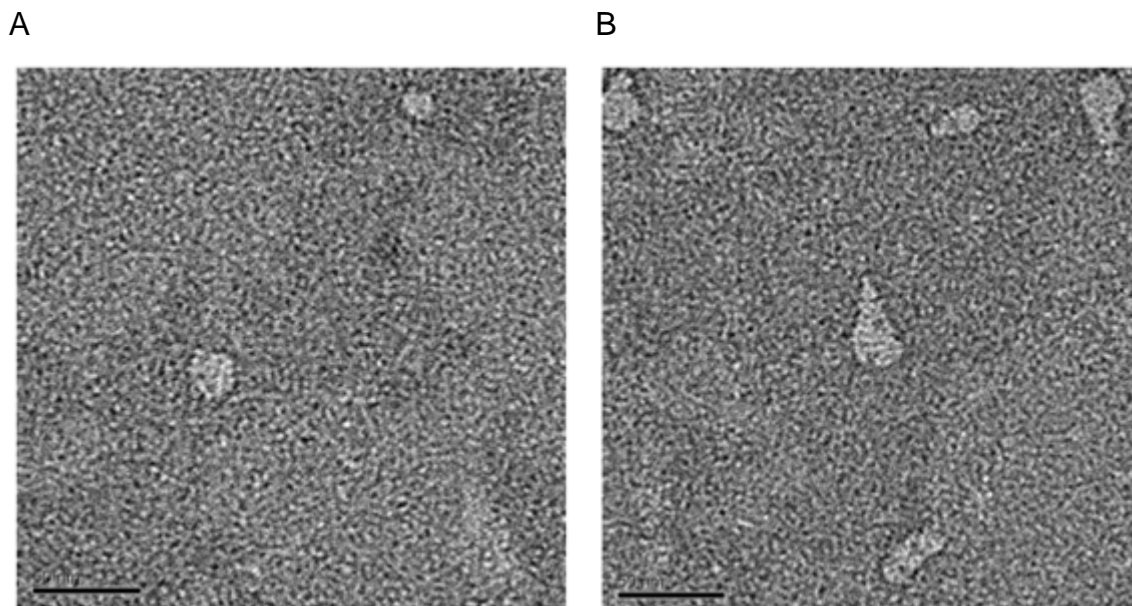


Figure III-1: TAM micrographs of 20 nm spherical polystyrene particles (bar represents 50 nm): (A) spheres, (B) stretched rod-like particles.

TEM requires tedious sample preparation, especially for organic particles, has non trivial image analysis and only analyzes small populations of the entire sample. Accordingly, we applied AF4 to obtain information about the size, morphology of spherical and stretched particles. Using the light scattering detector, one observes that spherical particles elute as a relatively narrow and symmetrical peak at 15 min (Figure III-2), while stretched particles elute as a rather broad peak between 15-40 min, with a small shoulder at 15 min, probably due to traces of non-stretched spherical particles (Figure III-2B). The measured radii of the main peaks show that spheres do not display any difference between hydrodynamic radius (11.4 nm, as determined by QELS) and radius of

gyration (11.8 nm, as determined by MALLS). In contrast, the stretched particles show a significant increase in the observed hydrodynamic radius (226.2 nm, QELS) as well as an even stronger increase in the radius of gyration (339.9 nm, MALLS). The QELS hydrodynamic radii measurements were confirmed using DLS bulk measurments. (Table III-1I).

Table III-1: Hydrodynamic radius ($r_h$) measurements of 20 nm polystyrene spherical and 3x stretched nanoparticles using DLS bulk measurements.

|  | Mean size (nm) | PDI |
|---|---|---|
| spheres | 11.4 | 1.01 |
| 3X stretched | 210 | 1.35 |

A                                                              B
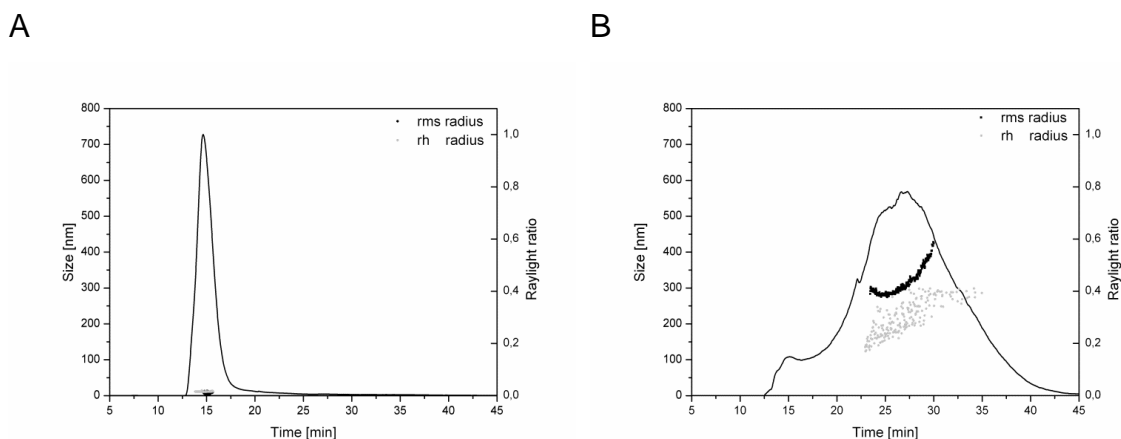


Figure III-2: (A) AF4 fractogram of 20 nm spherical polystyrene particles and (B) AF4 fractogram of 20 nm polystyrene stretched rod-like particles

Non-spherical MALLS and QUELS radii measurements do not correlate with the feret diameter. Therefore a "shape factor" was developed by Gajdos et al. to provide qualitative information about particle's geometry: The quotient of the geometric radius ($r_g$) to the hydrodynamic radius ($r_h$), describes the shape of a particle. Hard spheres have a shape factor around 0.778, soft spheres 0.977 while rod like particles display ~ 2 [6]. Our polystyrene spherical particles have a shape factor of 0.910, the stretched aggregated population displayed a shape factor of 1.792 (Figure III-3).
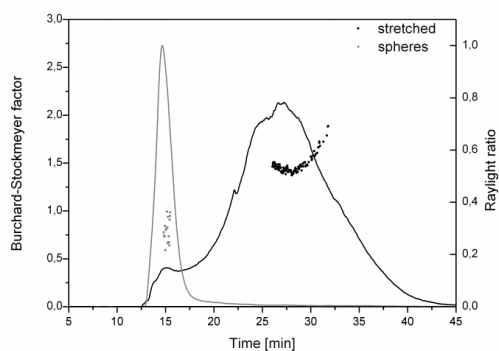
Figure III-3: AF4 fractogram: Burchard-Stockmayer factor of spherical (grey) and 3x stretched (black) aggregated particles.

The very large increase of the non-spherical nanoparticle diameter cannot be accounted exclusively to the stretching process. The washing steps at 40000 rpm might foster non-spherical nanoparticle aggregation. The high centrifugation speed (40000 rpm) was required to spin down the 20 nm nanoparticles. The long axis of the non-spherical nanoparticles made them susceptible for aggregation compared to their spherical counterparts. In addition to the harmful washing steps the long axis of the non-spherical nanoparticles could make them susceptible for membrane adsorption and further aggregation during the focus sequence of the AF4 method.

The existence of large aggregates in the non-spherical sample was confirmed by the injection of 500 nm spherical particles. The 500 nm particles eluted between 23 and 33 min Figure III-4 , which is in the time frame of the non-spherical sample in Figure III-2B.
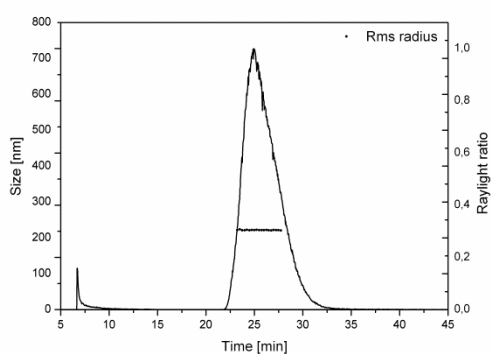
Figure III-4: AF4 fractogram of 500 nm spherical polystyrene particles.

In conclusion, the non-spherical nanoparticles aggregated and displayed an increased particle diameter in bulk DLS and AF4 measurements. The used AF4 method was not suitable to analyze or separate the differently shaped nanoparticle populations.

## 4. Discussion

Electron microscopy is an essential method to confirm the size and morphology of non-spherical particles and delivers useful qualitative information but it has several drawbacks, namely expensive and time consuming sample preparation and image analysis. The AF4 method coupled to MALLS and QELS has proven its versatility in the past to deliver qualitative and quantitative information about the size and morphology of the particles and thus offers the opportunity to become a routine quality control method for non-spherical particle drug delivery systems. However, this study reassures that a careful AF4 method development is required. During the focus sequence an up-concentration promotes the self-association of the sample [7].

QELS and bulk DLS measurements showed that the stretched particles display a much higher hydrodynamic radius compared to spherical ones and thus are aggregated.

As an outlook a new Frit-Inlet channel prototype (Wyatt Technology, Dernbach Germany) was developed, which mechanically routs the sample to the channel membrane. No focus sequence is needed with a Frit-Inlet channel. Accordingly, no up-concentration of the sample occurs, which is beneficial for self-association prone samples [8].

## 5. Conclusion

In conclusion, the use of AF4 as an orthogonal characterization method has proven potential in the past to provide information about particle size and shape. However, the AF4 shows several drawbacks as well and requires careful method development.

## 6. Acknowledgements

# 7. References

1.  Champion, J.A., Y.K. Katare, and S. Mitragotri, *Particle shape: A new design parameter for micro- and nanoscale drug delivery carriers.* Journal of Controlled Release, 2007. **121**(1-2): p. 3-9.
2.  Vermant, J., H. Yang, and G.G. Fuller, *Rheooptical determination of aspect ratio and polydispersity of nonspherical particles.* AIChE Journal, 2001. **47**(4): p. 790-798.
3.  Champion, J.A., Y.K. Katare, and S. Mitragotri, *Making polymeric micro- and nanoparticles of complex shapes.* Proceedings of the National Academy of Sciences, 2007. **104**(29): p. 11901-11904.
4.  Wagner, M., et al., *Asymmetric flow field-flow fractionation in the field of nanomedicine.* Analytical chemistry, 2014. **86**(11): p. 5201-5210.
5.  Harris, J.R., et al., *Application of the negative staining technique to both aqueous and organic solvent solutions of polymer particles.* Micron, 1999. **30**(4): p. 289-298.
6.  Gajdos, L.J. and H. Brenner, *Field-Flow Fractionation: Extensions to Nonspherical Particles and Wall Effects.* Separation Science and Technology, 1978. **13**(3): p. 215-240.
7.  Hupfeld, S., D. Ausbacher, and M. Brandl, *Asymmetric flow field-flow fractionation of liposomes: optimization of fractionation variables.* Journal of separation science, 2009. **32**(9): p. 1465-1470.
8.  Ali, M., et al., *Characterization of sodium hyaluronate blends using frit inlet asymmetrical flow field-flow fractionation and multiangle light scattering.* Analytical and bioanalytical chemistry, 2012. **402**(3): p. 1269-1276.

# IV. Chapter 4

## Influence of particle geometry and PEGylation on phagocytosis of particulate carriers

This chapter was published as a note in the *International Journal of Pharmaceutics*:

Mathaes, R., Winter, G., Besheer, A.* ǂ, & Engert, J.*ǂ (2014). Influence of particle geometry and PEGylation on phagocytosis of particulate carriers. International Journal of Pharmaceutics, 465(1), 159-164.

* These authors contributed equally to this work

ǂ Corresponding author

The experiments reported in this chapter have been carried out by Roman Mathaes. The paper has been written by Roman Mathaes. The following chapter would have not been possible without the scientific guidance of my supervisors Gerhard Winter, Julia Engert, and Ahmed Besheer. Ahmed Besheer provided knowledge about the PEGylation reaction. Julia Engert provided guidance regarding the cell culture experiments. All supervisors critically discussed the results in the end of the study and helped to interpret the data. Julia Engert submitted the manuscript to the journal.

The major aim of the first part of this thesis was to produce and characterize non-spherical micro- and nanoparticles. The aim of the second part was to investigate the non-spherical particles *in-vitro*. In the following chapter non-spherical particles were used in a macrophages cell line to investigate a possible impact of particle shape on phagocytosis.

# 1. Abstract

Particle geometry of micro- and nanoparticles has been identified as an important design parameter to influence the interaction with cells such as macrophages. A head to head comparison of elongated, non-spherical and spherical micro- and nanoparticles with and without PEGylation was carried out to benchmark two phagocytosis inhibiting techniques. J774.A1 macrophages were incubated with fluorescently labeled PLGA micro- and nanoparticles and analyzed by confocal laser scanning microscope (CLSM) and flow cytometry (FACS). Particle uptake into macrophages was significantly reduced upon PEGylation or elongated particle geometry. A combination of both, an elongated shape and PEGylation, had the strongest phagocytosis inhibiting effect for nanoparticles.

# 2. Graphical abstract
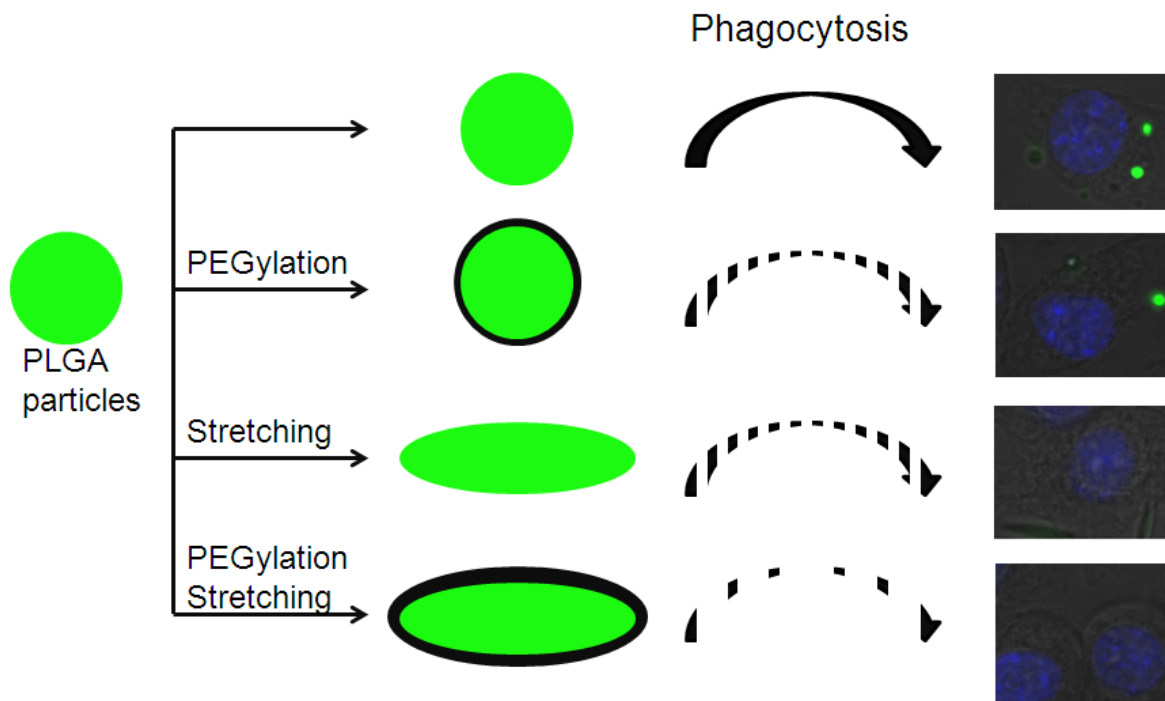
**Keywords**

## 3. Introduction

Biodegradable micro- and nanoparticle drug carrier systems have been explored for numerous applications [1-3], as particulate carrier systems have advantages when it comes to half-life extension [4, 5], protection of the drug from degradation, and enhancement of uptake into antigen-presenting [6] or other target cells [7, 8]. The physical and biochemical properties of particulate drug carrier systems (PDCS), such as size, composition of the polymer, charge and surface properties are usually considered as being the main factors influencing their bio-distribution. To overcome the drawback of rapid clearance by the mononuclear phagocyte system (MPS) in the spleen and liver [9], particle surfaces can be modified, e.g. using hydrophilic polymers such as poly(ethylene glycol) (PEG), thereby increasing circulation times [10]. Surprisingly, particle geometry has been traditionally neglected as an attribute that may alter the bio-distribution and circulation half-time. New fabrication methods like micro-fluids, non-wetting molds and mechanical stretching [11-15] allow the preparation of non-spherical particles and hence the investigation of particle shape's influence on circulation half-time and particle fate. For example, it has been reported in literature that ellipsoid particles display a lower internalization by macrophages [11, 16, 17]. Other shapes like discs trigger an increase in phagocytosis [18]. These observations show that particle shape can be an important parameter influencing the fate of particulate drug delivery systems. Although non-spherical gold particles or PEGylated nanorods have been investigated previously by Arnida et al. [19], a comparative study of PEGylated and non-PEGylated non-spherical biodegradable particles in the micro- and nanometer range has not been reported.

The aim of our study was to prepare elongated nano- and microparticles using the established film-stretching technique [20], and to further modify the particles by PEGylation. The internalization of 150 nm and 2 µm spherical and elongated PLGA particles, which were either PEGylated or non-PEGylated, by macrophages was investigated using confocal microscopy and flow cytometry.

# 4. Materials and Methods

## 4.1. Particles

150 nm and 2 µm fluorescently labeled (extinction 460/ emission 500) and non-labeled poly(lactic-co-glycolic acid) (PLGA) particles with a lactic/glycolic ratio 15/85 and chitosan coating were purchased from Phosphorex (Hopkinton,MA, USA). Polyvinylalcohol 40-88 (PVA) was purchased from Sigma-Aldrich (Steinheim, Germany). All the other materials were of analytical grade.

## 4.2. Preparation of non-spherical particles

Elongated particles were fabricated from spherical 150 nm and 2 µm PLGA particles using the film stretching method established by [11]. Briefly, PVA 40-88 and 2% glycerol was dissolved in highly purified water at 90°C (10% w/v). Spherical PLGA particles were added to this solution at a concentration of 0.2% w/v. The dispersion was poured into 4 x 6 cm molds and dried for 72 h at 20°C. The dried PVA/PLGA-particle film was cut into 3 x 1 cm sections and stretched using an in-house built manual device, consisting of two metal clamps and a screw separating the two clamps during the stretching process. The PLGA-PVA films were stretched in a silicone oil bath at 50°C at a stretching speed of 1 mm/s. After the stretching process, the film was cooled down to 30°C, washed with 100% isopropanol and dissolved in water to collect the particles. The spherical particles investigated in this study were treated the same way, but

without the stretching process. This ensured equal treatment of spheres and elongated particles.

### 4.3. Scanning electron microscopy

A Joel JSM 6500F scanning electron microscope (Joel Ltd, Tokyo, Japan) with Inca Software (Oxford instruments, Oxfordshire, UK) was utilized to confirm particle morphology. The different particle samples were fixed on aluminum stubs with self-adhesive tape and were sputtered with carbon. Collection of SEM micrographs was performed at a magnification of 2000 x for the 2 μm particles and 40000 x for the 150 nm particles.

### 4.4. Light obscuration

The 2 μm PLGA particles were analyzed by light obscuration using a SVSS-C particle counter equipped with a HCB-LD- 25/25 sensor (PAMAS, Partikelmess- und Analysesysteme GmbH, Rutesheim, Germany). The pre-run volume was set to 0.5 ml and the fill, rinse and emptying rate to 10 ml/min. Samples were analyzed in triplicates of 0.3 ml. High purified water was used to rinse the system prior to each run until the particle count of less than 25 particles / ml were reached.

### 4.5. Dynamic Light Scattering (DLS)

The 150 nm PLGA nanoparticles were analyzed in triplicates, each sample with 10 sub-runs using a Malvern Zetasizer Nano ZS with a 633 nm He-Ne laser (Malvern, Herrenberg, Germany). 700 μl of PLGA particles were measured in single use poly(methylmethacrylate) cuvettes (Brand, Wertheim, Germany) The path length of the cuvettes was 12.5 mm. The equilibration time was set to 120 s at 24°C. The Malvern Dispersion Technology software (version 4.20, Malvern, Herrenberg, Germany) was utilized to calculate the average diameter and polydispersity.

### 4.6. Differential Scanning Calorimetry (DSC)

150 nm PLGA particles were dispersed in high purified water at a concentration of 2 mg/ml and incubated overnight. The sample and reference cell of the VP-DSC MicroCalorimeter (MicroCal, Northamton, Massachusetts) were filled with the particle suspension and a corresponding water blank sample. The pre-scan temperature equilibration time was set to 15 min, the DSC scan rate was set to 1.5°C/min. Thermograms were recorded from 28°C to 48°C. The water blank was subtracted using Origin with MicroCal VPViewer2000 version 1.4.10 (Northampton, Massachusetts). Peak maximum represents the glass transition temperature (Tg) of the PLGA particles.

### 4.7. Surface modification of particles by PEGylation

Fluorescence label free PLGA particles with amine functionalized surface at a concentration of 1 mg/ml were incubated with 2 mg aldehyde PEG 20 kDa (Jenkem Technology, TX, USA) and 5 mM sodium cyanoborhydride (Sigma Aldrich, Steinheim, Germany) overnight. Particles were washed three times with water and dissolved in acetone. The successful PEGylation reaction was confirmed and quantified by the amine reactive fluorescence dye, fluorescamine (Sigma Aldrich, Steinheim, Germany), using a Cary Eclipse fluorescence spectrophotometer (Agilent, Boeblingen, Germany). The extinction wavelength was set to 390 nm, emission was observed at 475 nm. The fluorescamine intensity of PEGylated and non-PEGylated particles were compared to calculate the degree of PEGylation.

### 4.8. Determination of fluorescence stability incorporated into micro- and nanoparticles

1 mg/ml of the fluorescently labeled PLGA particles batches were incubated for 1 hour at 37°C. Particles were centrifuged and the supernatant was analyzed by a Cary Eclipse fluorescence spectrophotometer (Agilent, Boeblingen, Germany)

for free fluorescence dye. Values obtained for the supernatants were on a low baseline level.

### 4.9. Macrophage cell line

The murine macrophages cell line J-774A.1 was obtained from the German collection of Microorganisms and Cell Cultures, Heidelberg. Cells were seeded out at $1.5*10^6$ cells / 75 cm² cell culture flasks (Becton-Dickinson, Heidelberg, Germany) and cultured at 37°C for 3 days in an atmosphere containing 5% $Co_2$ in 90% Dulbecco's Modified Eagle's Medium (DMEM) (Sigma-Aldrich, Steinheim, Germany) and 10% FBS (Biochrom, Berlin, Germany). Cells were harvested at $4.5*10^7$ cells / 75 cm² by incubating with 3 ml Tris buffer and gently tappingthe culture flask against a table to detach cells.

### 4.10. Uptake of PLGA particles into macrophages

250 µl of a J774.A1 macrophages cell suspension at a concentration of 6*10^5 cells/ml in Dulbecco's modified eagle's serum with 10% FBS were incubated for 4 h in 8-well IBIDI µ-slides (IBIDI, Martinsried, Germany). 10 µl of a 2 mg/ml PLGA particle suspension was added in triplicates to the cells, homogenized by pipetting up and down and incubated for 45 min at 37° and on ice. The particle/cell suspension was washed and fixed with 4% paraformaldehyde (Sigma-Aldrich, Steinheim, Germany) and a cell core staining was applied using bisBenzimide H 33342 trihydrochloride (Sigma-Aldrich, Steinheim, Germany) for 10 min.

### 4.11. Endotoxin determination

PLGA particles were tested for endotoxin contamination in a Limulus amoebocyte lysate (LAL) assay (Charles River, Wilmington, USA).The endotoxin level measured for the 2 µm particles was between 0.3-0.4 U/mg and 3-4 U/mg for the 150 nm particles, respectively.

### 4.12.   Flow cytometry

Flow cytometry measurements were carried out using a Bioscience FACS Canto II (Bioscience, Franklin Lakes NJ, USA) equipped with forward-, side scatter and fluorescence detector. Fluorescence PLGA particle uptake into J744 macrophages was quantified with forward scatter (FSC) sensitivity of 174 volts and green fluorescence detector sensitivity of 385 volts. A triplicate of 10000 events each was collected per group twice. FACS data was analyzed using the Diva (BD Biosciences) and FlowJo (Tree Star) software using the mean fluorescence tool.

### 4.13.   Confocal Microscopy

The macrophages were examined utilizing a Zeiss 510 LSMNLO confocal microscope (Carl Zeiss Microscope systems, Jena, Germany) with identical setting for all groups. A Carl- Zeiss 63x oil immersion objective was used for acquisition. Images were averaged 4 times and scan speed was set to 6. 18 images were acquired per sample. Experiments were performed in triplicates twice. Internalized particles per cell were counted in case of the micrometer particles.

### 4.14.   Statistical significance

The statistical significance between the groups was investigated by a variance f-test followed by a t-test. A $p$ value $< 0.05$ indicated statistical significant differences.

## 5.  Results

Particle size and a successful stretching process were determined using electron microscopy as shown in Figure IV-1. Stretching the 2 µm PLGA

particles lead to a decrease in aspect ratio from 1 in case of the spheres to 0.204 ± 0.04. The aspect ratio of the 150 nm PLGA particles decreased from 1 for the spheres to 0.233 ± 0.06.
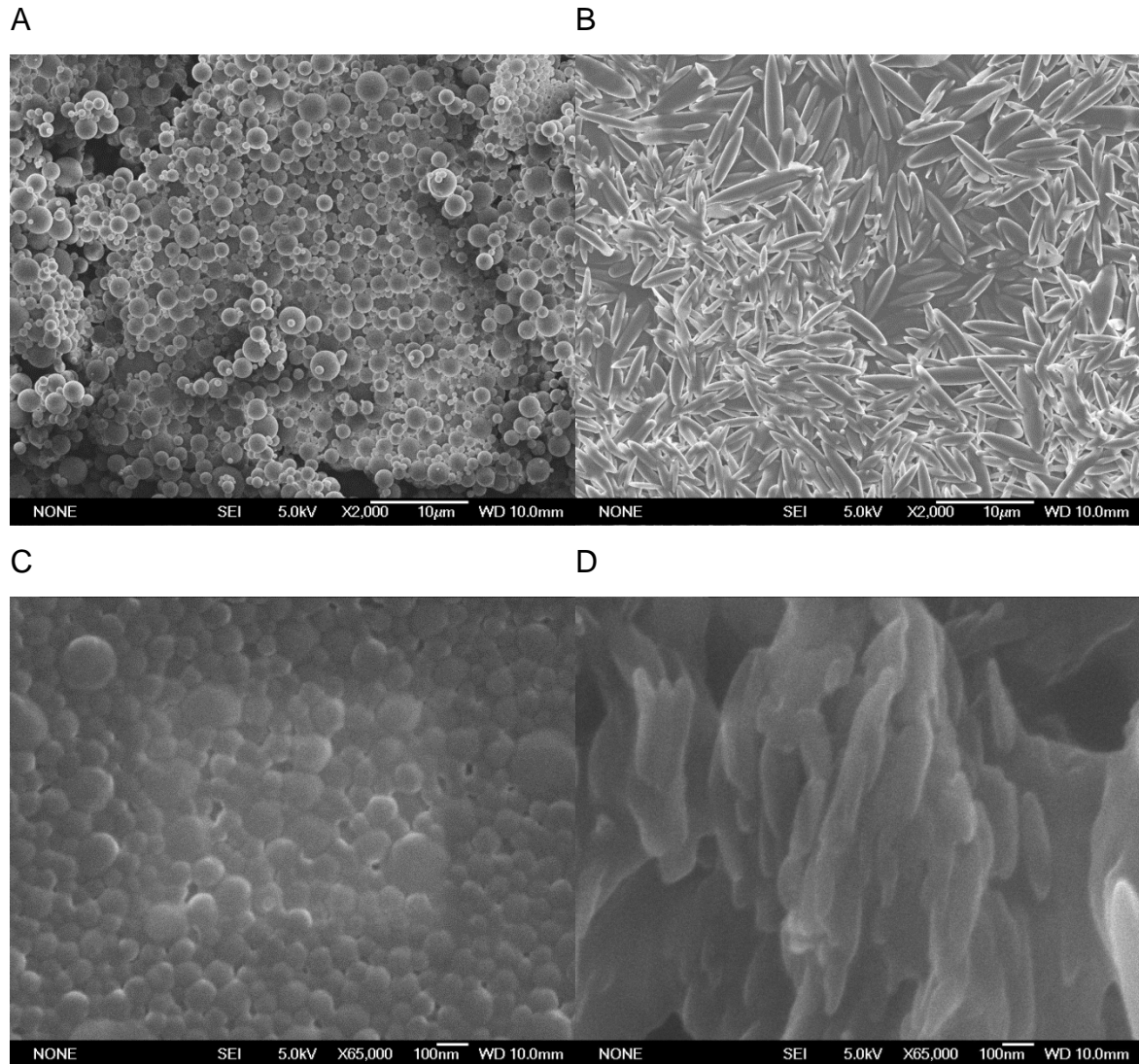


Figure IV-1: PLGA electron micrographs of PLGA particles (A) 2 µm spheres, (B) 2 µm 3× stretched particles, (C) 150 nm spheres and (D) 150 nm stretched.

DSC thermogram displayed a glass transition temperature ($T_g$) for the PLGA particles of 40–41 °C. Therefore, $T_g$ is sufficiently high to maintain particle shape even upon incubation at 37 °C. Nanoparticles were additionally analyzed by SEM to determine particle shape after an incubation step for 30 min at 37 °C. All particle batches were investigated regarding their physico-chemical

properties (Table IV-1), as particulate drug carrier systems can be destabilized when facing serum buffer salts [21], which leads to particle aggregation. In addition, the PEGylation degree and zeta potential may influence phagocytosis. For the microparticles, no aggregation was observed after a 15 min incubation step in culture media as determined by light obscuration. All groups had comparable properties regarding zeta potential (between +9.7 ± 1.3 mV and 15.4 ± 6.2 mV) and PEGylation efficiency (22.94 ± 13.74% for spheres and 30.04 ± 11.88 % for stretched particles). The nanoparticles displayed a small increase in size after 15 min incubation in culture media Table IV-1, however, comparable zeta potential (+27.4 ± 6.3 mV up to +34.1 ± 5.9 mV) and PEGylation degrees (32.33 ± 7.31% for spheres and 27.64 ± 11.87% for the stretched) were observed for all particles.

Table IV-1: The mean size and PDI, the mean size and PDI after incubation for 30 min in DMEM culture media, zeta potential and the degree of PEGylation of the different particle samples.

| | Mean size (µm) | PDI | Mean size (µm) after incubation | PDI | Zeta potential (mV) | PEGylation degree |
|---|---|---|---|---|---|---|
| 2 µm spheres | 1.73 ± 0.01 | 1.29 ± 0.00 | 1.72 ± 0.02 | 1.31 ± 0.01 | +12.5 ± 2.6 | – |
| 2 µm spheres PEG | 1.74 ± 0.02 | 1.29 ± 0.03 | 1.83 ± 0.05 | 1.42 ± 0.06 | +9.7 ± 1.3 | 30.04 ± 11.88 |
| 2 µm stretched | 1.62 ± 0.11 | 1.33 ± 0.01 | 1.65 ± 0.02 | 1.47 ± 0.03 | +15.4 ± 6.2 | – |
| 2 µm stretched PEG | 1.68 ± 0.17 | 1.35 ± 0.02 | 1.64 ± 0.03 | 1.41 ± 0.04 | +14.1 ± 3.7 | 22.94 ± 13.74 |
| 150 nm spheres | 0.182 ± 6.86 | 0.18 ± 0.02 | 0.243 ± 8.65 | 0.29 ± 0.06 | +33.2 ± 1.3 | – |
| 150 nm spheres PEG | 0.196 ± 9.35 | 0.16 ± 0.08 | 0.221 ± 7.37 | 0.21 ± 0.05 | +27.4 ± 6.3 | 32.33 ± 7.31 |
| 150 nm stretched | 0.224 ± 21.87 | 0.28 ± 0.12 | 0.256 ± 29.21 | 0.38 ± 0.19 | +34.1 ± 5.9 | – |
| 150 nm stretched PEG | 0.207 ± 26.41 | 0.31 ± 0.14 | 0.261 ± 41.96 | 0.46 ± 0.23 | +28.4 ± 3.1 | 27. |

The mean fluorescence of the cells correlates with internalized micro- and nanoparticles. The particle shape as well as PEGylation played an essential role influencing the uptake by the macrophages. Figure IV-2 shows CLSM images of macrophages incubated with 2 µm fluorescence green PLGA particles. The number of particles internalized is summarized in Figure IV-3a. J774.A1 macrophages took up 1.23 ± 0.520 spherical particles per cell. Stretched particles had a significantly reduced incident for internalization (0.424 ± 0.210 particles/cell). PEG coating renders a resistance to phagocytosis

for the spheres (0.417 ± 0.086 particles/cell), and PEGylated and stretched particles stayed on a low particle up-take level (0.374 ± 0.255 particles/cell). The number of microparticles attached to the cell membrane is shown in Figure IV-3b: 0.486 ± 0.161 stretched particles attached to the macrophages cell membrane, and PEGylated stretched microparticles attached to a same extend (0.487 ± 0.311). Spherical particles had a lower incident to attach to the macrophages cell membrane, as only 0.217 ± 0.041 spherical particles and 0.275 ± 0.142 PEGylated spherical particles were counted.
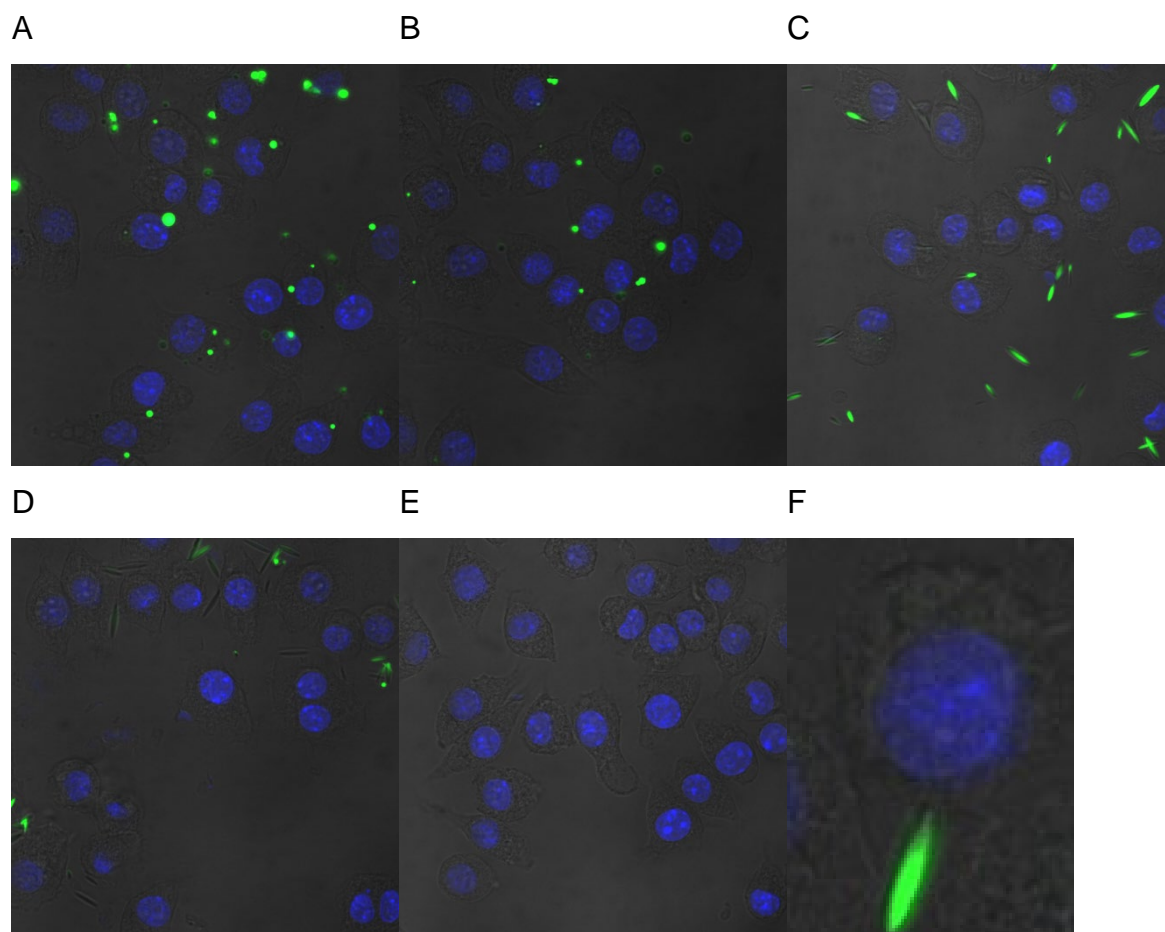


Figure IV-2: Incubation of bisBenzimide H 33342 trihydrochloride cell core stained J774.A1 macrophages at 37 °C with 2 µm green fluorescence PLGA particles analysed by CLSM: (A) spheres, (B) PEGylated spheres, (C) stretched, (D) PEGylated stretched, (E) no particles (control), (F) internalized stretched particles.
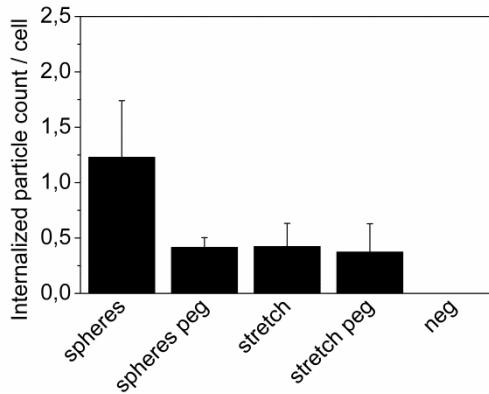
A                                          B
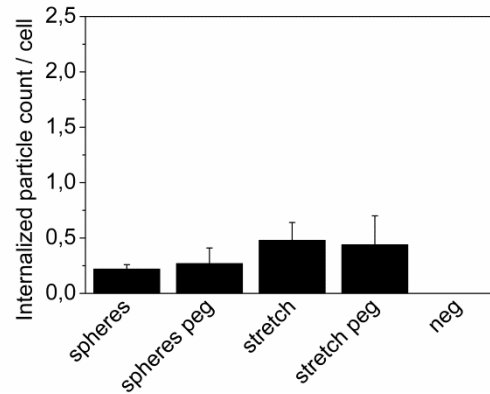


Figure IV-3: (A) Internalized 2 µm PLGA particles into J774.A1 macrophages counts and (B) attached 2 µm PLGA particles to J774.A1 macrophages.
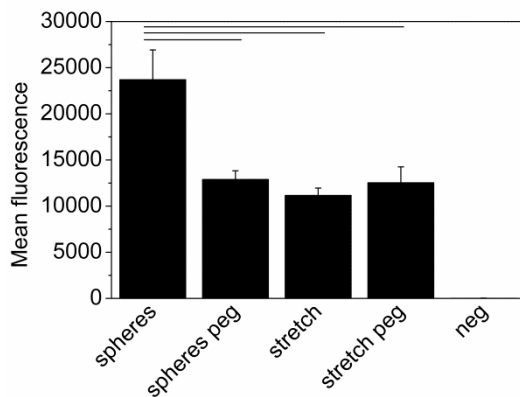
A                                          B
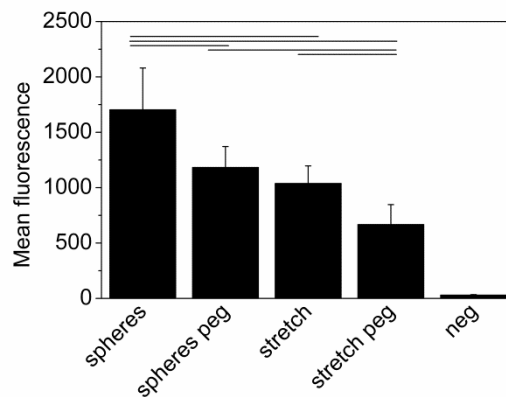


Figure IV-4: Flow cytometry data of the mean fluorescence intensity of J774.A1 macrophages after incubation with (A) 2 µm PLGA particles at 37 °C, (B) 100 nm PLGA particles at 37 °C.

The effect of shape and PEGylation on internalization was investigated also in the nanometer scale and played an essential role. Nanoparticle phagocytosis was analysed using flow cytometry. The mean fluorescence/cell was $1704 \pm 376$ for the spheres and $1183 \pm 187$ for PEGylated spherical particles Figure IV-4b. The mean fluorescence detected was even lower ($1039 \pm 157$) for the stretched and $668 \pm 178$ for the PEGylated stretched nanoparticles Figure IV-4b. Nanoparticle uptake assays were performed on ice to discriminate

between active and passive uptake. All samples displayed a low mean fluorescence level (between 10 ± 8 and 63 ± 43).

Different phagocytosis inhibiting techniques were investigated. The 2 µm microparticles significantly resisted phagocytosis after shape manipulation and PEGylation. CLSM and flow cytometry displayed comparable results regarding particle up-take Figure IV-3 and Figure IV-4. The positively charged 6 µm long major axis of 2 µm 3× stretched particles were prone to cell membrane attachment. However, the internalization process for particles attached to cells with their major axis is slowed down or not taking place at all. Our finding is in agreement with reports in the literature. For example, Yoo et al. reported that internalization of positively charged particles was slowed down in the first hours of incubation [22]. Particle orientation from the phagocyte's perspective also seems to be important for internalization. Elongated 2 µm particles were exclusively observed entering the macrophages at their rounded ends.

These results were also found upon analysis of the 150 nm nanoparticles. Likewise, surface functionalization with PEG and stretching particles to an elongated shape influenced the internalization by macrophages. However, the difference in mean fluorescence measured by flow cytometry for spheres and stretched particles was smaller for the nanometer particles than that observed for the micrometer particles. The decreased particle size seems to attenuate the effect of particle shape regarding phagocytosis resistance [23]. Interestingly, a combination of PEGylation and stretching techniques resulted in a superb internalization reduction for particles in the nanometer range Figure IV-4b.

With regards to the two different particles sizes, we found that 150 nm particles did not sediment on macrophages during the 30 min incubation period unlike the 2 µm microparticles. Instead, nanoparticles had a higher tendency to aggregate in DMEM culture media. Microparticles were counted by traditional particle counting methods like light obscuration, while nanoparticle concentration was determined by their fluorescence intensity. Consequently, a comparison of different experimental groups within one size is significant, while a comparison between micro and nanoparticles needs to be done cautiously.

Our study shows that an elongated particle geometry reduces the recognition and phagocytosis by macrophages. The two uptake inhibiting techniques PEGylation and stretching reduced the incident of internalization to a comparable extent. In the nanometer scale a combination of surface chemistry and particle geometry had an additive effect leading to greatly reduced inner cell particle concentration.

# 6. References

1. Fifis, T., et al., *Size-Dependent Immunogenicity: Therapeutic and Protective Properties of Nano-Vaccines against Tumors.* The Journal of Immunology, 2004. **173**(5): p. 3148-3154.
2. Langer, R., *New methods of drug delivery.* Science, 1990. **249**(4976): p. 1527-1533.
3. Yang, L., et al., *Receptor-Targeted Nanoparticles for In vivo Imaging of Breast Cancer.* Clinical Cancer Research, 2009. **15**(14): p. 4722-4732.
4. Besheer, A., et al., *Characterization of PLGA Nanospheres Stabilized with Amphiphilic Polymers: Hydrophobically Modified Hydroxyethyl Starch vs Pluronics.* Molecular Pharmaceutics, 2009. **6**(2): p. 407-415.
5. Owens III, D.E. and N.A. Peppas, *Opsonization, biodistribution, and pharmacokinetics of polymeric nanoparticles.* International Journal of Pharmaceutics, 2006. **307**(1): p. 93-102.
6. Bachmann, M.F. and G.T. Jennings, *Vaccine delivery: a matter of size, geometry, kinetics and molecular patterns.* Nature Reviews Immunology, 2010. **10**(11): p. 787-796.
7. Cho, K., et al., *Therapeutic Nanoparticles for Drug Delivery in Cancer.* Clinical Cancer Research, 2008. **14**(5): p. 1310-1316.
8. Peer, D., et al., *Nanocarriers as an emerging platform for cancer therapy.* Nat Nano, 2007. **2**(12): p. 751-760.
9. Hume, D.A., *The mononuclear phagocyte system.* Current Opinion in Immunology, 2006. **18**(1): p. 49-53.
10. Gref, R., et al., *'Stealth'corona-core nanoparticles surface modified by polyethylene glycol (PEG): influences of the corona (PEG chain length and surface density) and of the core composition on phagocytic uptake and plasma protein adsorption.* Colloids and surfaces. B, Biointerfaces, 2000. **18**(3-4): p. 301.
11. Champion, J.A., Y.K. Katare, and S. Mitragotri, *Making polymeric micro- and nanoparticles of complex shapes.* Proceedings of the National Academy of Sciences, 2007. **104**(29): p. 11901-11904.
12. Dendukuri, D., et al., *Continuous-flow lithography for high-throughput microparticle synthesis.* Nature Materials, 2006. **5**(5): p. 365-369.
13. Manoharan, V.N., M.T. Elsesser, and D.J. Pine, *Dense Packing and Symmetry in Small Clusters of Microspheres.* Science, 2003. **301**(5632): p. 483-487.
14. Merkel, T.J., et al., *Scalable, Shape-Specific, Top-Down Fabrication Methods for the Synthesis of Engineered Colloidal Particles.* Langmuir, 2009. **26**(16): p. 13086-13096.
15. Rolland, J.P., et al., *Direct fabrication and harvesting of monodisperse, shape-specific nanobiomaterials.* Journal of the American Chemical Society, 2005. **127**(28): p. 10096-10100.
16. Champion, J. and S. Mitragotri, *Shape Induced Inhibition of Phagocytosis of Polymer Particles.* Pharmaceutical Research, 2009. **26**(1): p. 244-249.
17. Champion, J.A. and S. Mitragotri, *Role of target geometry in phagocytosis.* Proceedings of the National Academy of Sciences of the United States of America, 2006. **103**(13): p. 4930-4934.

18. Sharma, G., et al., *Polymer particle shape independently influences binding and internalization by macrophages.* Journal of Controlled Release, 2010. **147**(3): p. 408-412.

19. Arnida, et al., *Geometry and surface characteristics of gold nanoparticles influence their biodistribution and uptake by macrophages.* European Journal of Pharmaceutics and Biopharmaceutics, 2011. **77**(3): p. 417-423.

20. Champion, J.A., Y.K. Katare, and S. Mitragotri, *Particle shape: A new design parameter for micro- and nanoscale drug delivery carriers.* Journal of Controlled Release, 2007. **121**(1-2): p. 3-9.

21. Langer, K., et al., *Optimization of the preparation process for human serum albumin (HSA) nanoparticles.* International Journal of Pharmaceutics, 2003. **257**(1–2): p. 169-180.

22. Yoo, J.-W., N. Doshi, and S. Mitragotri, *Endocytosis and Intracellular Distribution of PLGA Particles in Endothelial Cells: Effect of Particle Geometry.* Macromolecular Rapid Communications, 2010. **31**(2): p. 142-148.

23. Barua, S., et al., *Particle shape enhances specificity of antibody-displaying nanoparticles.* Proceedings of the National Academy of Sciences, 2013. **110**(9): p. 3270-3275.

# V. Chapter 5

## Influence of particle size, geometry, and adjuvants on dendritic cell activation

Roman Mathaes, Gerhard Winter, Teruna Siahaan, Ahmed Besheer*, Julia Engert*,

* These authors contributed equally to this work

‡ Corresponding author

The experiments in this chapter have been carried out by Roman Mathaes, partly in the lab of Teruna Siahaan at the University of Kansas. The mansucribt has been written by Roman Mathaes. The following chapter would have not been possible without the scientific guidance of my supervisors Gerhard Winter, Julia Engert, Ahmed Besheer, and Teruna Siahaan. Ahmed Besheer supervised the adsorption of the polyI:C adjuvants on the different particle batches. Julia Engert supervised the cell culture experiments as well as the immunology assays. Teruna Siahaan helped to establish the dendritic cell line. All supervisors critically discussed the results in the end of the study and helped to interpret the data. All authors gave imput and reviewed the final manuscribt. Julia Engert submitted the manuscript to the journal.

The first part of the *in-vitro* studies with the macrophages cell line showed that non-spherical particles as well as PEGylated particles displayed a reduced phagocytosis. Following the influence of particle shape on dendritic cell

activation was investigated. Therefore, micro- and nanoparticles with adsorbed toll-like-receptor agonists were incubated with the dendritic cell line JAWSII. In a second step activated JAWSII cells were stained for activation surface markers and analyzed using flow cytometry.

## 1. Abstract

Modern subunit vaccines have many benefits compared to live vaccines like convenient and competitive large scale production, better reproducibility and safety. However, the poor immunogenicity of subunit vaccines usually requires the addition of potent adjuvants or drug delivery vehicles. Accordingly, researchers are investigating different adjuvants and particulate vaccine delivery vehicles to boost the immunogenicity of subunit vaccines. Despite the rapidly growing knowledge in this field, a comparison of different adjuvants is sparsely found. Until today, little is known about efficient combinations of the different adjuvants and particulate vaccine delivery vehicles.

In this study we compared three adjuvants towards their immune stimulatory potential and combined them with different particulate vaccine delivery vehicles. For this reason, we investigated two types of polyI:C and a CL264 base analogue and combined these adjuvants with differently sized and shaped particulate vaccine delivery vehicles. A high molecular weight polyI:C combined with a spherical nano-sized particulate vaccine delivery vehicle promoted the strongest dendritic cells activation.

**Keywords:** Non-spherical particles; flow cytometry; nano-rods; adjuvants; vaccination; dendritic cells

## 2. Introduction

Vaccination is a potent and cost-effective tool to treat and prevent fatal diseases [1]. The morbidity of life threatening diseases like smallpox, polio, hepatitis B, or measles has been significantly reduced [2]. Consequently, the mortality of children dropped from 20 million cases worldwide in 1960 to less than 10 million in 2005 [2].

On the other hand, the development of subunit vaccines facilitates the industrial large scale production by reducing production costs, and increases the accessibility of vaccines to poor regions. Living pathogens can cause serious side effects or death in immune-deficient patients, as they can reverse to virulent wild-type strains [3]. Subunit vaccines consist of purified oligopeptides, recombinant proteins, or viral subunits, which cannot lead to disease and thus have a lower toxicological profile [4]. Despite these benefits, subunit vaccines are rather poorly immunogenic and require the addition of a potent adjuvant [5].

Adjuvants and particulate vaccine delivery vehicles have been applied to boost the immunogenic potency of subunit vaccines [6]. Specifically, adjuvants enhance antigen presentation and co-stimulation by the activation of pattern recognition receptors (PRRs) like toll-like receptors (TLR) in antigen-presenting-cells (APC) [7]. For example, TLR 3 recognizes double-stranded (ds) RNA and activates the TRIF-dependent pathway, which leads to the induction of type I interferon [8, 9].

One example of adjuvants acting via TLR 3 are polyinosine-polycytidylic acids (polyI:C), which are synthetic dsRNAs available in different molecular weights [9]. Similarly, TLR 7/8, which is highly homologous to TLR9, recognizes several synthetic imidazoquinolines and induces several inflammatory cytokines like interferon alpha [8, 10]. The natural ligands of the TLR 7/8 family remain unclear. The adenine analog CL264 is a resiquimod analogue recognized by TLR 7/8 and is functionalized by a carboxy group for chemical conjugation [11-13].

Upon administration of TLR agonists, like the above mentioned vaccine adjuvants, DCs are activated, which leads to DC maturation. The maturation process can be described by several factors. For example, a loss in phagocytic capacity, an increased expression of MHC molecules, the production of cytokines, and the up-regulation of co-stimulatory molecules including CD80, CD83, and CD86. The co-stimulatory molecules play an important role in the immune response and indicate dendritic cell activation [14].

Besides adjuvants, particulate vaccine delivery vehicles are used to efficiently deliver antigens to APCs. For this reason, numerous particulate vaccine delivery vehicles like liposomes [15], microparticles [16], nanoparticles [17], immune stimulating complexes (ISCOMs) [18-20], and virus-like particles (VLPs) [21] have been used as vaccine delivery vehicles in order to mimic pathogens. These particulate vaccine delivery vehicles can differ in size [22], charge [23], surface chemistry [24], and shape [25, 26].

Particle shape has recently been identified to influence particle uptake into different immune cells. Champion *et al.* showed that an elongated particle shape reduces the incidence of particle phagocytosis into macrophages [27]. In addition, different pathogens like *Escheria coli* or *Aeromonas hydrophila* display an elongated shape [28]. It is still unclear whether a non-spherical particle shape could influence the activation of immune cells.

The response of the immune system to an antigen depends on processing and presentation of the antigen by antigen presenting cells (APCs). Vaccine delivery vehicles are used to enhance the uptake into APCs and thus promote efficient antigen presentation. The overall efficiency of a vaccine delivery vehicle is a complex interplay of the physical and chemical vaccine delivery vehicle properties and is further boosted in a combination with an adjuvant [29]. Consequently, the synergistic combination of adjuvants and a vaccine delivery vehicle represents a promising strategy to enhance immunogenicity of subunit vaccines [5, 30].

Despite the progress in understanding the effect of adjuvants and particulate vaccine delivery vehicles, little is known about potent combination of different adjuvants and vaccine delivery vehicles, which are promising concepts to boost the immunogenicity of vaccines [31]. In particular, a comparison of different molecular weight polyI:Cs and TLR 7/8 adjuvants has not been reported. Zhou *et al.* compared a soluble low molecular weight and a soluble high molecular weight polyI:C. The high molecular weight polyI:C promoted a stronger immune response than the low molecular weight polyI:C *in-vitro* [32]. Nevertheless, the two different polyI:C forms have not been compared in combination with different particulate vaccine delivery vehicles to further boost their immune stimulatory potential. Micro- and nanoparticles have clearly proven their ability as vaccine delivery vehicles, however the preferred size and shape is still controversially discussed [22].

In this study, we compared two different molecular weight polyI:C TLR 3 ligands, as well as the TLR 7/8 CL264 adenine base analogue. In addition, we adsorbed the above mentioned adjuvants to differently sized and shaped polystyrene particles. All adjuvant samples were then applied to the dendritic cell (DC) line JAWSII and tested towards their potential to stimulate the DCs. JAWSII stimulation was followed by flow cytometry measurements of the co-stimulatory molecules CD83 and CD86.

## 3. Materials and Methods

### 3.1. Micro- and nanoparticles

Fluorescently labeled (extinction 460/emission 500) and label free 150 nm and 2 µm polystyrene particles were purchased from Phosphorex (Hopkinton, Ma, USA).

## 3.2. Non-spherical micro- and nanoparticle fabrication

The film stretching method established by Champion *et al.* [33] was used to stretch spherical 150 nm and 2 μm polystyrene particles to elliptical particles with tailored aspect ratios as mentioned earlier [34]. In brief, spherical particles were incorporated into a polyvinyl alcohol 40-88 (PVA) film (Sigma-Aldrich, Steinheim, Germany). PVA 40-88 (10% w/v) was dissolved in highly purified water at 80°C. Then, 2% of glycerol (Sigma-Aldrich, Steinheim, Germany) and spherical polystyrene particles (0.2% w/v) were added to this solution. The mixture was dried at room temperature for 4 days in 4 x 6 cm molds until a flexible film was formed. The PVA film was cut into 2 x 3 cm pieces and fixed in an in-house built film-stretching device. The 2 cm long PVA – film including the spherical polystyrene particles was stretched to the length of 6 cm in a silicone oil bath at 120°C at a stretching speed of 2 cm per minute. Afterwards, the stretched PVA film was cooled down to room temperature and washed with 100% isopropanol (Sigma-Aldrich, Steinheim, Germany). Finally, the PVA films were dissolved in highly purified water to recover the non-spherical particles. Non-spherical particles stretched to three fold of their original length are referred to as 3X stretched particles. To ensure comparability, the spherical particles used in the following *in vitro* study were treated in the same manner but without stretching the PVA film.

## 3.3. Scanning electron microscopy (SEM)

Particle morphology was confirmed using a Joel JSM 6500F scanning electron microscopy (Joel Ltd, Tokyo, Japan). Spherical and non-spherical particles were applied to a filter paper and attached to self-adhesive tape on aluminum scanning electron microscopy stubs. Afterwards, the samples were sputtered with carbon. SEM image collection was performed at 8000x magnification for the nanoparticles and 2000x magnification for the microparticles. The aspect ratio of the 3X stretched micro- and nanoparticles were calculated using the

SEM images (20 particles measured per group). The Inca software (Oxford instruments, Oxfordshire, UK) was utilized to process image acquisition data.

### 3.4. Light obscuration

Microparticles were measured by light obscuration (LO) utilizing a SVSS-C system (PAMAS, Partikelmess- und Analysesysteme GmbH, Rutesheim, Germany). All microparticle batches were analyzed in triplicates. The measuring volume was set to 0.3 ml and the pre-run volume was set to 0.5 ml. The system was cleaned with highly purified water until the particle count was less than 25 counts/ml between each measurement.

### 3.5. Dynamic light scattering

Nanoparticles were analyzed using a Malvern Zetasizer Nano ZS (Malvern, Herrenberg, Germany). Each sample was measured in triplicates; each triplicate was performed with 11 sub-runs at 24°C. 400 µl of the polystyrene particle suspensions were measured in a poly(methylmethacrylate) cuvettes (Brand, Wertheim, Germany) with a path length of 12.5 mm. Particle size was measured in water or culture media. Particle zeta potential was measured in water including 10 mM sodium chloride. The particle concentration was always 0.06 mg/ml. Size, zeta potential, and polydispersity index (PDI) were calculated using the Malvern Dispersion Technology software (version 4.20, Malvern, Herrenberg, Germany).

### 3.6. Fluorescence stability on polystyrene micro- and nanoparticles

Polystyrene particles were incubated overnight in highly purified water at 37°C to test the stability of the fluorescent dye incorporated into the particles. The supernatant was analyzed after centrifugation for free fluorescence dyes using

a Cary Eclipse fluorescence spectrophotometer (Agilent, Boeblingen, Germany).

### 3.7. Adjuvant loading on polystyrene micro- and nanoparticles

200 μl of 10 mg/ml label free polystyrene particles were incubated with 100 μl of a 0.33 mg/ml adjuvant solution and incubated for 5 hours. Particles were then centrifuged and the supernatant was analyzed by UV measurements to detect unbound adjuvant. Loading efficiency was calculated as ratio between loaded adjuvants on particles divided by the total amount of adjuvant used. Particles with surface loaded adjuvants were resuspended in highly purified water.

### 3.8. Colloidal stability of polystyrene particle adjuvant complexes in water and culture media

The different micro- and nanoparticle adjuvant loaded samples were incubated in the JAWSII dendritic cell culture media (described below) for 30 min at 37°C. Particle aggregation behavior was monitored using the Malvern Zetasizer Nano ZS for the nanoparticles or the SVSS-C light obscuration system for microparticles.

### 3.9. JAWSII dendritic cell (DC) line

A JAWSII dendritic cell line (ATCC, Teddington, United Kingdom) was grown in a $CO_2$ incubator at 5% $CO_2$ and at 37°C. $3 \times 10^6$ cells/ml were grown in an 80 $cm^2$ culture flask. The culture medium consisted of Iscove's Modified Dulbeco's Medium (IMDM) (Sigma Aldrich, Steinheim, Germany) with 5 ng/ml murine GM-CSF (Invitrogen, Darmstadt, Germany) and 10% fetal calf serum (FCS) (Invitrogen, Darmstadt, Germany). Cells were cultured in 80 cm² culture flasks with 15 ml culture media. The sub cultivation ratio was 1:2. The 15 ml culture

media was renewed twice a week. JAWSII DCs were seeded at 100,000 cells per 0.5 ml culture media in a 48 well plate.

## 3.10. JAWSII dendritic cell (DC) stimulation

JAWSII dendritic cells were stimulated with 0.83 µg of free adjuvant (low molecular weight poly:IC (LMW), high molecular weight poly:IC (HMW), or CL264 (all adjuvants from Invivogen, Toulouse, France) or 50 µg of adjuvant-loaded particles. Native particles without any adjuvant but phosphate buffer saline (PBS) were used as controls. Adjuvant loaded particles or free adjuvants were added, pipetted up and down, and incubated overnight to the JAWSII seeded in the 48 well plates.

## 3.11. JAWSII dendritic cell staining

All cells were washed with 0.2 ml PBS buffer and incubated with an anti-CD16/32 (Becton, Dickinson and Company, Franklin Lakes, USA) antibody to block non-specific binding sites for 15 min on ice in the dark. Cells were then stained with 0.5 µg/well of CD83 (Becton, Dickinson and Company, Franklin Lakes, USA) and CD86 (Becton, Dickinson and Company, Franklin Lakes, USA) for 20 min on ice in the dark. The compensation controls were prepared using the above mentioned fluorescence polystyrene particles or the CD83 and CD86 staining antibody solutions.

## 3.12. Cell analytics by flow cytometry

All samples were analyzed using a Bioscience FACS Canto II (Bioscience, Franklin Lakes NJ, USA) equipped with forward- (FSC), side scatter (SSC), and fluorescence detectors (FITC, PE, APC). The FSC detector voltage was set to 319 volts, the SSC detector voltage was set to 401 volts, the FITC detector

voltage was set to 500 volts, the PE voltage was set to 250 volts, and the APC detector voltage was set to 350 volts. Stimulated cells were analyzed in triplicates. Each triplicate contained 10,000 cells. Triplicates were collected twice (n=6). Flow cytometry data was analyzed using the Flowjo software (Tree Star, Ashland, Oregon, USA). Fluorescence intensity was analyzed using the mean intensity tool.

## 3.13. Dimethylthiazol-yl-diphenyltetrazoliumbromid (MTT) cell viability assay

A final stock solution of 5 mg/ml was produced with Thiazolyl Blue Tetrazolium Bromide (Sigma-Aldrich, Taufkirchen, Germany). First, JAWSII dendritic cells were treated as described above in the DC activation studies. Afterwards, the toxicity assay was performed. Cells were incubated for 4h at room temperature with the MTT solution. Therefore, the blue crystals were dissolved in dimethyl sulfoxide (DMSO) by shaking for 5 min at 300 rpm. Absorbance was measured at 540 nm using a Fluostar Omega plate reader (BMG Labtech GmbH, Offenburg, Germany) in 96-well plates (Greiner Bio-one GmbH, Frickenhausen, Germany). Pure DMSO was used as a blank.

## 3.14. Statistical significance

Statistical analysis was performed using a one way ANOVA test followed by a Fisher LSD method. P was set to < 0.001 and alpha was 0.05. All statistical calculations were performed using Sigma Plot (Systat Software Inc., San Jose, CA, USA).

## 4. Results

Ellipsoid fluorescence labeled polystyrene micro- and nanoparticles were stretched towards high aspect ratios using the film stretching technique established by Champion et al. [33]. The successful stretching process was confirmed by scanning electron microscopy (SEM) (Figure V-1). The mean aspect ratio decreased from 1 for spherical micro- and nanoparticles to 0.23±0.07 in case of the 3X stretched microparticles, and 0.21±0.01 for the 3X stretched nanoparticles (Figure V-1).
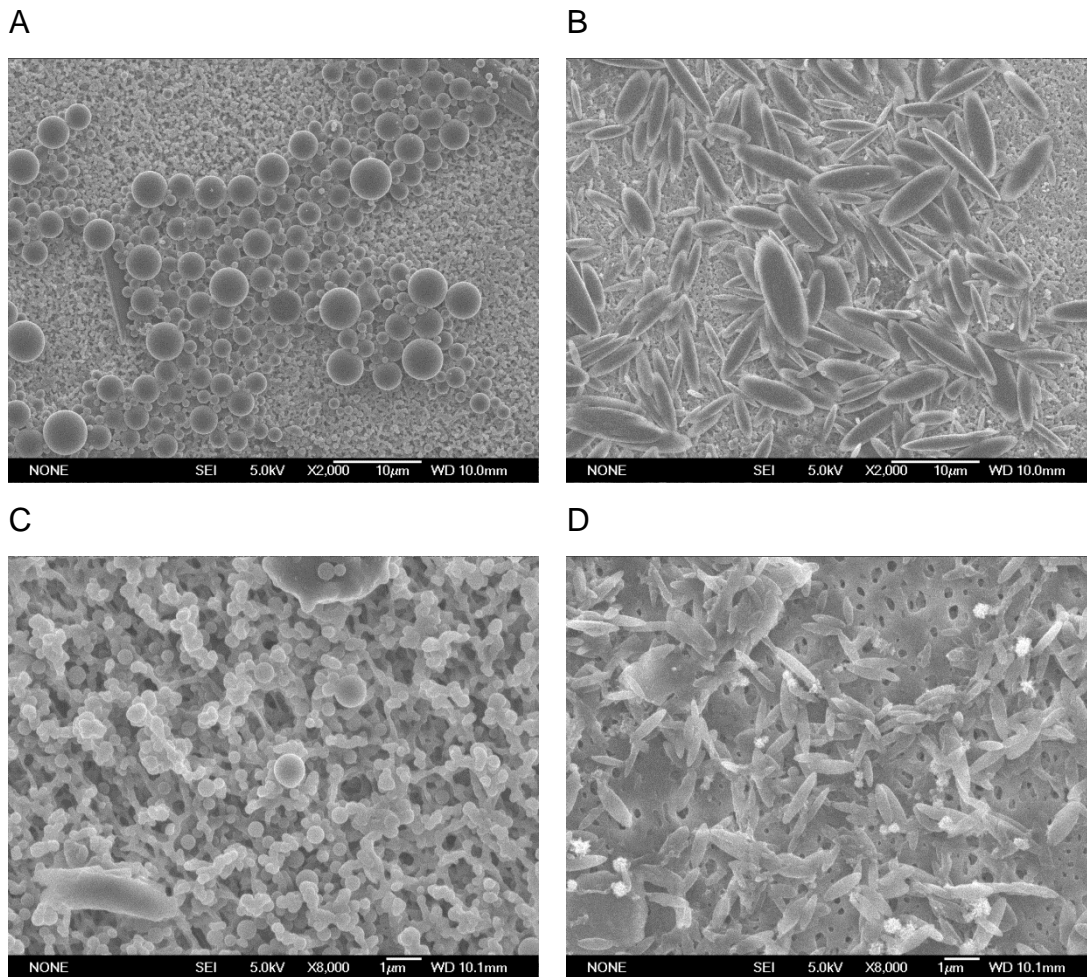
Figure V-1: SEM micrographs of spherical and non-spherical micro- and nanoparticles: (A) spherical microparticles, (B) non-spherical 3X stretched microparticles, (C) spherical nanoparticles, and (D) non-spherical 3X stretched nanoparticles.

## 4.1. Particle characterization

Nanoparticle DLS measurements revealed a nanoparticle size of 132±1.2 nm for the spheres and 172.5±16.5 nm for 3X stretched particles. Loading nanoparticles with polyI:C or CL264 did not increase particle size, no aggregation was observed. Microparticles were measured by LO. Spheres were sized 1.5±0.0 µm and 3X stretched particles 1.6±0.1 µm. No increase in microparticles' size was observed after loading the microparticles with polyI:C or CL264.

In addition, particle aggregation in the JAWSII culture media was investigated. The different particle groups were incubated in the JAWSII culture media for 30 min. The different nanoparticle samples displayed an increase in particle size from 126.8±2.4 to 185.5±20.5 nm (before incubation in culture media) to 227.7±1.3 to 589.5±31.5 nm (after incubation in culture media) (Table V-1). Microparticles did not show any increase in particle size after incubation in culture media.

The zeta potential of the different particle batches was measured to confirm the adjuvant loading. For example, it was +62.1±2.7 mV for spherical unloaded nanoparticles and +55.8±2.3 mV for 3X stretched unloaded nanoparticles. As expected, the adsorption of negatively charged adjuvants decreased the zeta potential. Nanoparticles loaded with the high molecular weight polyI:C showed the strongest decrease in zeta potential (+46.1±1.3 mV for spheres and +47.2±1.2 mV for 3X stretched particles). The loading efficiency experiment showed similar results. The high molecular weight loaded nanoparticle samples showed the highest loading efficiency (83.1±13.0% for spheres and 86.4±6.7% for 3Xstretched particles) (Table V-1).

Table V-1: An overview of the different nanoparticle sample characteristics used in the *in vitro* experiments (low molecular weight polyI:C (LMW), high molecular weight polyI:C (HMW), and the base analogue CL264 (CL264)).

| | Mean size | PDI | Mean size after incubation in DEMEM | PDI | Zeta potential [mV] | Loading efficiency [%] | Cell viability [%] |
|---|---|---|---|---|---|---|---|
| 150 nm | 132.9 ±1.2 | 0.1± 0.0 | 462.0±32.0 | 0.5±0.0 | +62.1±2.7 | -- | 63.5±11.6 |
| 150 nm LMW polyI:C | 134.9 ±1.3 | 0.2± 0.0 | 227.7±1.3 | 0.3±0.0 | +49.7±1.4 | 62.7±16.3 | 61.1±10.4 |
| 150 nm HMW polyI:C | 126.8 ±2.4 | 0.2± 0.0 | 526.0±32.0 | 0.5±0.1 | +46.1±1.3 | 83.1±13.0 | 57.5±5.5 |
| 150 nm CL264 | 133.8 ±1.2 | 0.1± 0.0 | 380.0±3.0 | 0.7±0.0 | +54.7±0.7 | 32.4±5.1 | 64.9±9.6 |
| 150 nm 3X | 172.5 ±16.5 | 0.1± 0.0 | 580.5±17.5 | 0.5±0.1 | +55.8±2.3 | -- | 53.0±13.9 |
| 150 nm LMW polyI:C 3X | 185.5 ±20.5 | 0.2± 0.1 | 398.5±33.5 | 0.4±0.1 | +47.2±1.2 | 58.2±21.1 | 72.8±8.8 |
| 150 nm HMW polyI:C 3X | 158.5 ±4.5 | 0.2± 0.0 | 589.5±31.5 | 0.5±0.1 | +36.8±1.1 | 86.4±6.7 | 53.4±15.1 |
| 150 nm CL264 3X | 222± 12.0 | 0.1± 0.0 | 421.0±44.0 | 0.2±0.0 | +41.0±0.6 | 27.1±5.6 | 66.3±14.9 |

Similarly, zeta potential measurements were obtained for the microparticle samples. Unloaded microparticles displayed the highest zeta potential values (+28.6±0.3 mV for the spheres and +34.3±0.7 mV for the 3X stretched particles). Likewise, the high molecular weight polyI:C loaded microparticles had the lowest zeta potential of all microparticle batches (+19.5±0.2 mV for the spheres and +24.5±0.3 mV for the 3X stretched particles). The results from loading efficiency experiments confirmed the zeta potential measurements. The loading efficiency was high for the high molecular weight samples (71.8±6.3% for the spheres and 68.5±11.3% for the 3X stretched particles).

Table V-1: An overview of the different nanoparticle sample characteristics used in the *in vitro* experiments (low molecular weight polyI:C (LMW), high molecular weight polyI:C (HMW), and the base analogue CL264 (CL264)).

| | Mean size | PDI | Mean size after incubation in DEMEM | PDI | Zeta potential [mV] | Loading efficiency [%] | Cell viability [%] |
|---|---|---|---|---|---|---|---|
| 2 µm | 1.5±0.0 | 1.3±0.0 | 1.6±0.1 | 1.3±0.1 | +28.6±0.3 | -- | 35.7±15.7 |
| 2 µm LMW polyI:C | 1.5±0.0 | 1.3±0.0 | 1.5±0.0 | 1.3±0.0 | +22.3±0.3 | 61.2±7.3 | 38.9±11.3 |
| 2µm HMW polyI:C | 1.6±0.0 | 1.3±0.0 | 1.5±0.0 | 1.3±0.0 | +19.5±0.2 | 71.8±6.3 | 41.6±4.4 |
| 2 µm CL264 | 1.5±0.0 | 1.2±0.0 | 1.5±0.0 | 1.3±0.0 | +26.1±0.3 | 19.3±24.2 | 32.9±9.7 |
| 2 µm 3X | 1.6±0.1 | 1.4±0.1 | 1.7±0.1 | 1.4±0.1 | 34.3±0.7 | -- | 48.6±7.2 |
| 2 µm LMW polyI:C 3X | 1.7±0.0 | 1.3±0.0 | 1.6±0.0 | 1.5±0.0 | +16.6±0.2 | 58.7±3.2 | 41.5±8.6 |
| 2 µm HMW polyI:C 3X | 1.7±0.0 | 1.4±0.1 | 1.9±0.0 | 1.4±0.1 | +24.5±0.3 | 68.5±11.3 | 31.0±6.0 |
| 2 µm CL264 3X | 1.8±0.0 | 1.3±0.0 | 1.8±0.1 | 1.5±0.0 | +21.7±0.6 | 18.7±3.4 | 43.8±11.5 |

In conclusion, the overall loading efficiency was higher for nanoparticles compared to the microparticles. No relevant differences between the different particle shapes were observed.

In addition, cell viability was investigated using a MTT cell viability assay. The overall cell viability was higher for the nanoparticle groups (between 53.0±13.9% up to 72.8±8.8). Cell viability decreased for the cell samples, which received a microparticle treatment (31.0±6.0% to 66.3±14.9%).

### 4.2. Particle uptake into JAWSII dendritic cells

Fluorescently labeled particle internalization was investigated by flow cytometry. First, the stability of the fluorescent dye loading into the polystyrene particles was tested by analysis of the supernatant of a particle suspension for free fluorescent dyes. No free fluorescent dye was found in the supernatant. Consequently, the inner cell fluorescence concentration can be correlated to the inner cell particle concentration.
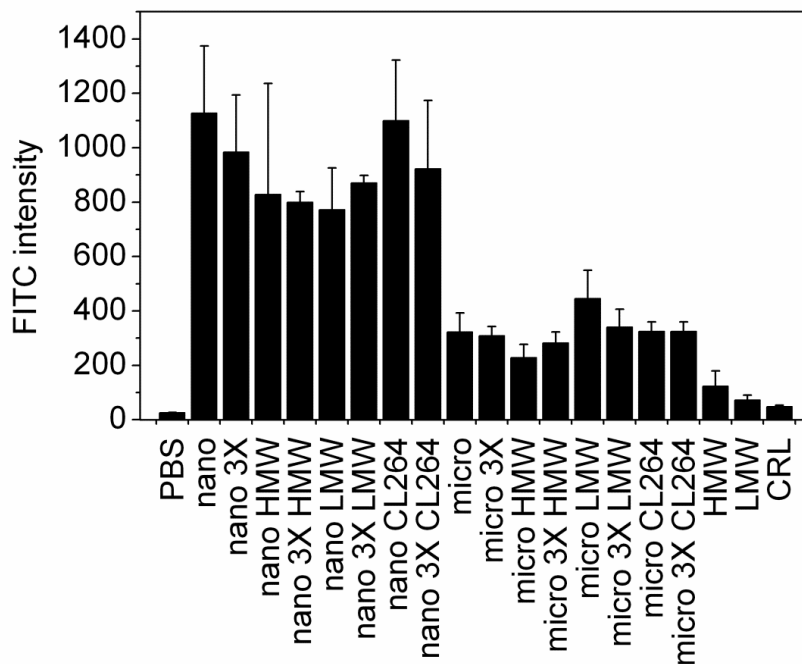


Figure V-2: Mean fluorescence intensity per cell measured by flow cytometry and analyzed using six samples per group.

Nanoparticles were internalized by JAWSII dendritic cells more efficiently than microparticles. The mean inner fluorescence concentration per cell ranged from $228.3\pm48.3$ to $445.3\pm104$ for the microparticles and $772.0\pm153.5$ to $1127.6\pm246.6$ for the nanoparticles (Figure V-2). All nanoparticle vaccine delivery vehicle groups displayed significant higher inner cell particle concentrations than all the microparticle vaccine delivery vehicles, adjuvants without particles, and the negative PBS control. However, no significant differences in the mean fluorescence per cell were observed for spherical and elongated particles. The different nanoparticle adjuvant vaccine delivery

vehicles were internalized less than the plain nanoparticles. For example, the nano HMW, the nano 3x HMW, nano LMW, and nano 3x LMW had significant lower inner particle concentrations than the plain nanoparticles. (Figure V-2). The PBS control and the particle free type adjuvant groups displayed baseline levels of mean fluorescence per cell (Figure V-2).

### 4.3. JAWSII DC activation

Comparison of the different adjuvants

In addition to particle uptake, JAWSII dendritic cell stimulation was accessed by investigating the up-regulation of CD 83 and CD86 dendritic cell surface markers. A good correlation between CD83 and CD86 was found (Figure V-3 (A), (B)). The negative control PBS and the spherical and non-spherical nanoparticles without adjuvants displayed a significant lower CD83 and CD86 up-regulation than all other nanoparticle vaccine delivery with adjuvants. The low activation of adjuvant free samples was expected and proved the overall suitability of the dendritic cell activation assay.

The high molecular weight polyI:C nanoparticle vaccine delivery vehicles (nano HMW) displayed the strongest up-regulation of CD83 as well as for CD86. The nano HMW mean CD86 intensity per cell was 180.7±67.5 and the CD83 nano HMW mean intensity per cell was 2500±54.7. (Figure V-3 (A), (B)).

A
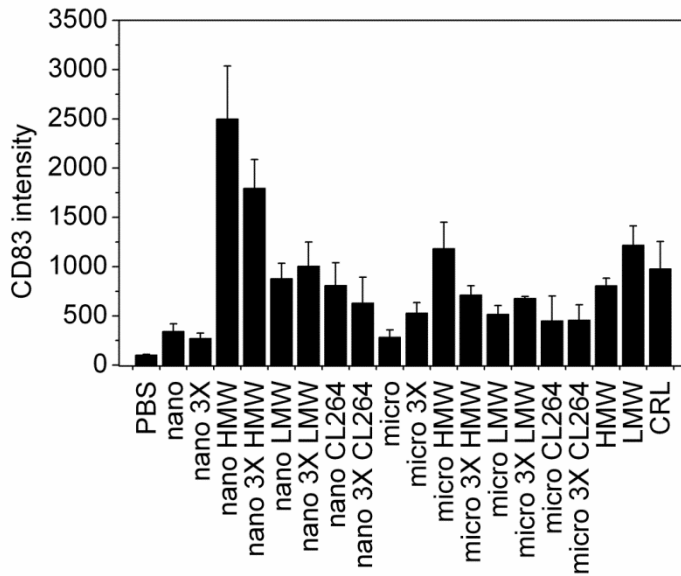


B
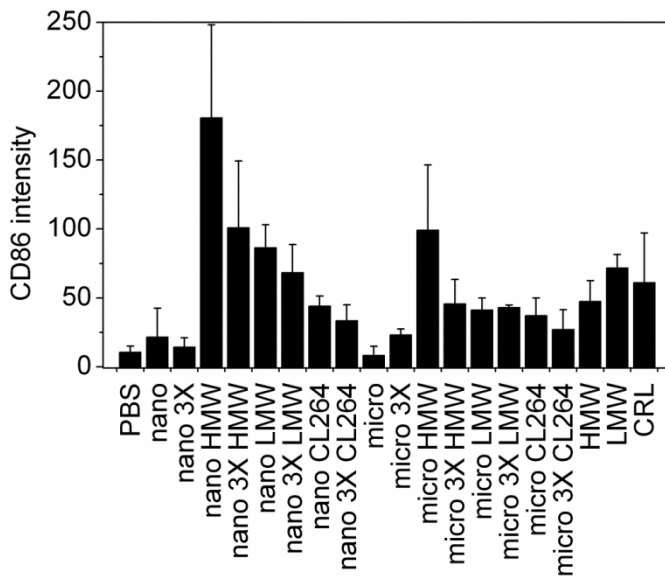


Figure V-3: Dendritic cell stimulation: (A) up-regulation of CD83, (B) up-regulation of CD86 measured by flow cytometry and analyzed using six samples per group.

The up-regulation of CD83 and CD86 by the nano HMW vaccine delivery vehicle was significantly higher compared to all other tested groups. The CL264 nanoparticle (nano CL264, Figure V-3) vaccine delivery vehicles showed the lowest up-regulation of CD83 and CD86. Accordingly, the spherical CL264 vaccine delivery vehicles (nano CL264, Figure V-3) displayed a CD83 mean

intensity per cell of only 808±230 and a CD86 mean intensity per cell of 74±7.4. Similarly, the CL264 3X stretched vaccine delivery vehicles (nano 3X CL264, Figure V-3) stayed on a very low mean CD83 and CD86 up-regulation level. (CD83 was 630±263 and CD86 was 33.4±11.6).

The low molecular weight polyI:C vaccine delivery vehicles displayed an intermediate JAWSII DC stimulation potential (significantly lower than the high molecular weight polyI:C vaccine delivery vehicles (Figure V-3).

In conclusion, the high molecular weight polyI:C vaccine delivery vehicles stimulated the DCs significantly stronger than all other samples.

Comparison of particle size (microparticles vs. nanoparticles)

Nanoparticles were internalized more efficiently by JAWSII dendritic cells. Consequently, the nanoparticle adjuvant vaccine delivery vehicles displayed a stronger DC activation than the microparticle adjuvant vaccine delivery vehicles. For example, the high molecular weight polyI:C nanoparticle vaccine delivery vehicles (nano HMW, Figure V-3 (A)) showed a mean CD83 intensity per cell of 2500±537.9. In contrast, the high weight polyI:C microparticle vaccine delivery vehicles (micro HMW, Figure V-3 (A)) showed a significantly lower mean CD83 intensity per cell (1183±263). Furthermore, the nano 3x HMW vaccine delivery vehicle displayed a CD83 intensity of 1795.7±2912 and a CD86 intensity of 101.0±48.4, which was significantly higher than the microparticle counterparts (CD83: 677.3±19.4 and CD86: 43.0±1.7). Similar results were also observed for the nano LMW vaccine delivery vehicles which trigger a significant higher DC activation than the micro LMW vaccine delivery vehicle.

Influence of particle shape (spherical vs. 3X stretched elongated) on DC activation

The spherical high molecular weight polyI:C nanoparticle and microparticles vaccine delivery vehicles (nano HMW and micro HMW, Figure V-3 (A,B)) displayed a significant stronger mean CD83 and CD86 intensity than the non-spherical counterparts. Particularly the spherical and elongated nanoparticle

HMW vaccine delivery vehicles showed the most prominent difference in DC activation. For example, the CD86 intensity of nano HMW was (2500±537) whereas the 3X stretched high molecular weight polyI:C nanoparticles had only a CD 86 intensity of (1795.66±291) (nano 3X HMW, Figure V-3 (B)).

Similar results were observed for microparticle HMW vaccine delivery vehicles. The spherical high molecular weight polyI:C microparticle vaccine delivery vehicles (micro HMW, Figure V-3 (B)) displayed a stronger mean CD86 intensity (1183±267) than the 3X stretched high molecular weight polyI:C microparticles (713±93), (micro 3X HMW, Figure V-3 (B)). In addition, the mean CD83 intensity showed stronger JAWSII DC activation for spheres than for 3x stretched particle vaccine delivery vehicles (Figure V-3 (A)).

Despite the difference in DC activation for the spherical and elongated particles with the high molecular weight polyI:C vaccine delivery vehicles, other adjuvant vaccine delivery vehicles displayed only minor changes in DC activation regarding particle shape. Particle shape had no relevant influence on DC activation in samples not containing the HMW poly:IC adjuvant.

The FACS dot plots in Figure V-4 confirmed the results from Figure V-2 and Figure V-3. The PBS negative controls display no green fluorescence nanoparticles and no CD83, CD86 activation, which proves the overall suitability of the experimental layout. The green fluorescent nanoparticles (Figure V-4 D,G) were internalized more efficiently compared to the microparticles (Figure V-4 J,M). The FACS dot plots for the nanoparticle vaccine delivery vehicles (Figure V-4 D,G) display a prominent cell population of FITC high cells, whereas the FACS dot plots of the microparticle vaccine delivery vehicles (Figure V-4 J,M) display less FITC high cells. The high molecular weight polyI:C spherical nanoparticles displayed the strongest activation. For example, Figure V-4 (E) displays the largest PE high cell population (CD83 activation) compared to all other groups.

In summary, the high molecular weight polyI:C vaccine delivery vehicles stimulated the JAWSII dendritic cell line stronger than all other adjuvant vaccine

delivery vehicles (low molecular weight polyI:C and CL264). In addition, nanoparticles activated the JAWSII dendritic cells stronger than microparticles. Spherical particles stimulated JAWSII dendritic cells stronger than non-spherical particles in case of the HMW vaccine delivery vehicles. However, particle shape had no effect for the LMW and CL264 vaccine delivery vehicles.

A



B



C



D



E



F



G



H



I
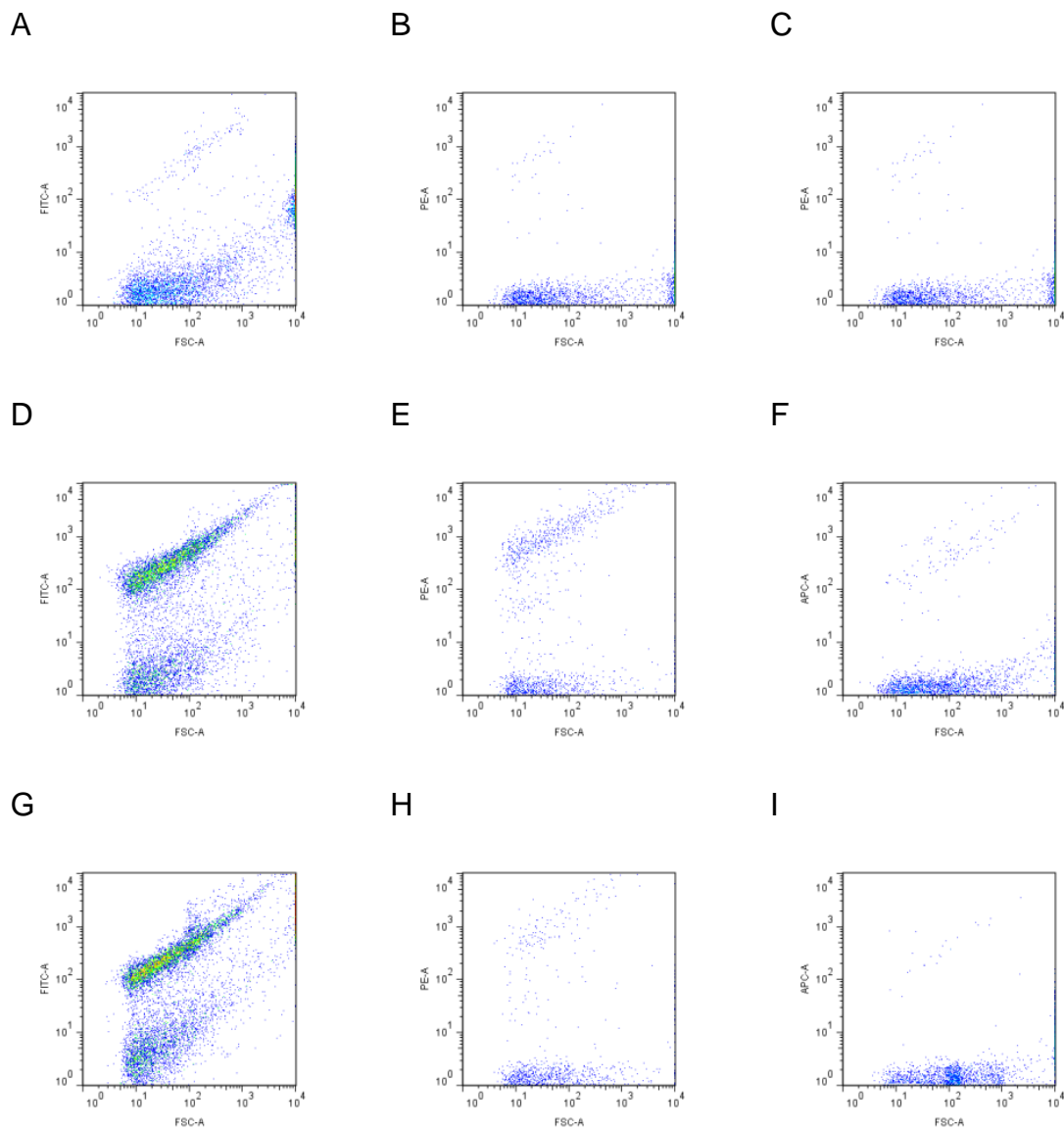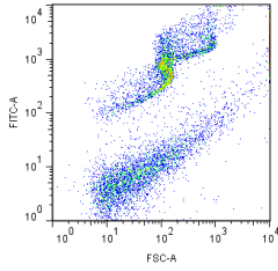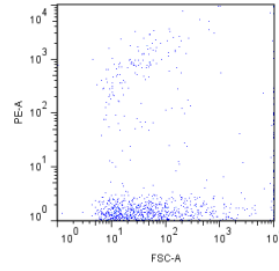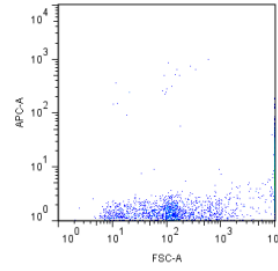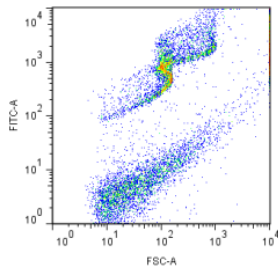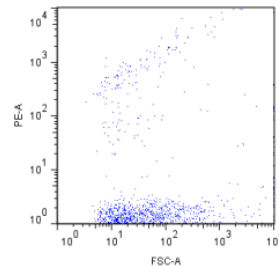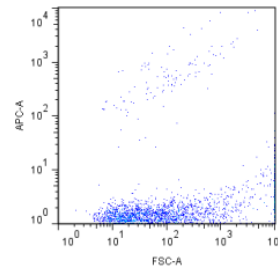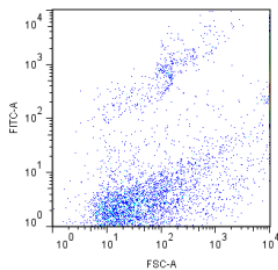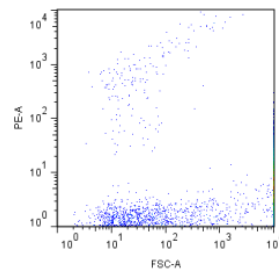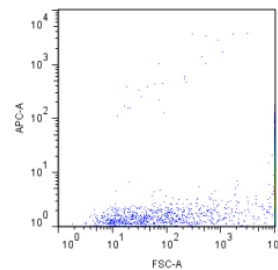
Figure V-4: FACS dot plots of JAWSII DC: X-axis forward scatter, Y-axis inner particle concentration (1st column), (CD83 (2nd column), CD86 (3rd column). A-C: PBS negative controle, D-F: HMW polyI:C spherical nanoparticles, G-I: HMW polyI:C non-spherical nanoparticles, J-L: HMW polyI:C spherical microparticles, M-O: HMW polyI:C microparticles, O-R: HMW polyI:C.

## 5. Discussion

In this study different vaccine delivery vehicles design parameters were analyzed towards their ability to stimulate DCs of the JAWSII dendritic cell line.

First, the internalization of the different vaccine delivery vehicles into dendritic cells was investigated. In the literature, polyI:C loaded PLGA microparticles as a vaccine delivery vehicle have been reported [4, 31]. However, a direct comparison to polyI:C nanoparticles and to different particle shapes has not been performed.

In our study nanoparticles were internalized more efficiently compared to microparticles. This can be explained by the preference of the dendritic cells for nanoparticles, but also by the higher positive zeta potential of the nanoparticles. The impact of particle size and surface charge has been investigated by Foged *et al.* In accordance to our findings, nanoparticles were internalized by dendritic cells more efficiently than microparticles. A positive zeta potential increased phagocytosis in vitro. However, the authors did not investigate dendritic cell activation with different TLR agonists and used only spherical particles [35]. Thiele *et al.* already reported that a positive zeta potential promotes particle uptake into APCs [36]. For this reason, the polyI:C vaccine delivery vehicles, which had a lower zeta potential, displayed a lower incident for internalization into dendritic cells compared to the plain, unbound particle groups.

Secondly, JAWSII dendritic cell activation was investigated. Despite the fact that only minor difference in DC activation were observed for the free, unbound adjuvants, major differences were revealed for the different vaccine delivery vehicles. The strong activation potential of the high molecular weight polyI:C (HMW) vaccine delivery vehicles can be explained by two factors. First, high molecular weight polyI:C stimulates DCs stronger than low molecular weight polyI:C. Similar results were achieved before by Zhou *et al.* [32]., who compared high molecular weight polyI:C and low molecular weight polyI:C, but did not combine the polyI:Cs to different vaccine delivery vehicles. Secondly, due to the cooperative nature of the polyelectrolyte interaction, the long dsRNA

chains of the HMW polyI:C are expected to interact stronger with particulate carriers than the LMW polyI:C. Accordingly, a higher loading efficiency for the HMW polyI:C was achieved. While this higher loading efficiency could have improved the delivered dose to the cells and led to the observed high DC activation, there is currently no direct evidence for this hypothesis.

In addition to the strong impact of the adjuvants, particle size played an important role in DC activation. Nanoparticles were the superior delivery vehicles for several reasons. The larger surface area and the strong positive zeta potential of nanoparticles resulted in a higher adjuvant loading efficiency. Accordingly, more adjuvant was delivered to the dendritic cells. More important, the nanoparticles were internalized more efficiently by the dendritic cells, because of their ideal size and strong positive zeta potential. Similar results were obtained by Thiel *et al.* [36] and Jung *et al.* [37], where nanoparticles induced stronger immunity than microparticles. In addition, Nixon *et al.* [38] showed that nanoparticles promote a stronger cytotoxic lymphocyte response than microparticles.

Finally, the influence of particle shape on DC activation was investigated. Numerous pathogens like bacteria or viruses display an elliptical non-spherical shape, which was the motivation to the current investigation of shape-dependent DC activation. However, the non-spherical particles did not promote a stronger DC stimulation. Instead, in case of HMW polyI:C, the non-spherical micro and nanoparticles were less potent in stimulating DCs compared to their spherical counterparts. Reasons for the observed lower DC activation could be the slightly lower particle uptake, the lower zeta potential, or the lower cell viability. Non-spherical particles were observed to resist internalization by APCs before [39]. For example, Champion *et al.* found that elongated particles resist phagocytosis by macrophages [40]. In addition, Arnida *et al.* showed a decreased internalization for gold nano-rods into macrophages [41]. Vaccine delivery vehicles loaded with LMW polyI:C or CL264 displayed no difference in DC activation due to variations in particle shape.

A head to head comparison of spherical and non-spherical TLR-agonist loaded vaccine delivery vehicles is missing. Despite the fact, that non-spherical particles did not show an increased DC activation, the results of this study provide essential information for the design of future vaccine delivery vehicles.

The above results show that the spherical nanoparticles loaded with HMW polyI:C represent a promising future vaccine delivery vehicles. In addition to a superior APC stimulation of nanoparticles compared to microparticles, nanoparticles show several other benefits. For example, the preparation is simple and uses less toxic solvents. Moreover, the preparation must not be aseptic as small nanoparticles can be sterile filtered [22]. Besides these, the small size of nanoparticles allows a free diffusion into the lymph nodes and the targeting of a specific DC subset [30].

## 6. Conclusion

In this study we compared different vaccine delivery vehicle properties like particle size and particle shape, but also different adjuvants towards their ability to stimulate the JAWSII dendritic cell line.

First, a combination of an adjuvant and a vaccine delivery vehicle showed stronger DC activation than adjuvants or vaccine delivery vehicles alone.

Second, the nanoparticle vaccine delivery vehicles displayed the stronger DC activation compared to their microparticle vaccine delivery vehicles counterparts.

Third, the high molecular weight polyI:C displayed the strongest DC activation potential of all adjuvants in combination with an vaccine delivery vehicle.

Finally, particle geometry played only a minor role in DC activation. However, spherical particles showed a stronger DC activation for the HMW polyI:C vaccine delivery vehicles than elongated vaccine delivery vehicles.

Consequently, in our study the spherical nanoparticle vaccine delivery vehicle with HMW polyI:C represent the most potent system to stimulate DCs.

## 7. References

1.	Kwon, Y.J., et al., *Enhanced antigen presentation and immunostimulation of dendritic cells using acid-degradable cationic nanoparticles.* Journal of Controlled Release, 2005. **105**(3): p. 199-212.
2.	Andersen, P. and S.H.E. Kaufmann, *Novel Vaccination Strategies against Tuberculosis.* Cold Spring Harbor Perspectives in Medicine, 2014. **4**(6).
3.	Liljeqvist, S. and S. Ståhl, *Production of recombinant subunit vaccines: protein immunogens, live delivery systems and nucleic acid vaccines.* Journal of Biotechnology, 1999. **73**(1): p. 1-33.
4.	Hafner, A.M., et al., *Tuning the immune response of dendritic cells to surface-assembled poly (I: C) on microspheres through synergistic interactions between phagocytic and TLR3 signaling.* Biomaterials, 2011. **32**(10): p. 2651-2661.
5.	Salvador, A., et al., *Combination of immune stimulating adjuvants with poly (lactide-co-glycolide) microspheres enhances the immune response of vaccines.* Vaccine, 2012. **30**(3): p. 589-596.
6.	Hafner, A.M., B. Corthésy, and H.P. Merkle, *Particulate formulations for the delivery of poly (I: C) as vaccine adjuvant.* Advanced Drug Delivery Reviews, 2013. **65**(10): p. 1386-1399.
7.	O'Neill, L.A., D. Golenbock, and A.G. Bowie, *The history of Toll-like receptors [mdash] redefining innate immunity.* Nature Reviews Immunology, 2013. **13**(6): p. 453-460.
8.	Takeda, K., T. Kaisho, and S. Akira, *Toll-like receptors.* Annual Review of Immunology, 2003. **21**(1): p. 335-376.
9.	Schulz, O., et al., *Toll-like receptor 3 promotes cross-priming to virus-infected cells.* Nature, 2005. **433**(7028): p. 887-892.
10.	Akira, S. and K. Takeda, *Toll-like receptor signalling.* Nat Rev Immunol, 2004. **4**(7): p. 499-511.
11.	Diebold, S.S., et al., *Innate Antiviral Responses by Means of TLR7-Mediated Recognition of Single-Stranded RNA.* Science, 2004. **303**(5663): p. 1529-1531.
12.	Gibson, S.J., et al., *Plasmacytoid dendritic cells produce cytokines and mature in response to the TLR7 agonists, imiquimod and resiquimod.* Cellular immunology, 2002. **218**(1): p. 74-86.
13.	Chinenov, Y., et al., *Role of transcriptional coregulator GRIP1 in the anti-inflammatory actions of glucocorticoids.* Proceedings of the National Academy of Sciences, 2012. **109**(29): p. 11776-11781.
14.	Lechmann, M., et al., *CD83 on dendritic cells: more than just a marker for maturation.* Trends in Immunology, 2002. **23**(6): p. 273-275.

15. Henriksen-Lacey, M., et al., *Liposomal vaccine delivery systems.* Expert Opinion on Drug Delivery, 2011. **8**(4): p. 505-519.

16. O'Hagan, D.T. and M. Singh, *Microparticles as Vaccine Adjuvants and Delivery Systems.* Novel Vaccination Strategies2004: Wiley-VCH Verlag GmbH & Co. KGaA. 147-172.

17. Moon, J.J., et al., *Enhancing humoral responses to a malaria antigen with nanoparticle vaccines that expand Tfh cells and promote germinal center induction.* Proceedings of the National Academy of Sciences, 2012. **109**(4): p. 1080-1085.

18. Myschik, J., et al., *On the preparation, microscopic investigation and application of ISCOMs.* Micron, 2006. **37**(8): p. 724-734.

19. Myschik, J., T. Rades, and S. Hook, *Advances in lipid-based subunit vaccine formulations.* Current Immunology Reviews, 2009. **5**(1): p. 42-48.

20. Myschik, J., et al., *Immunostimulatory biodegradable implants containing the adjuvant Quil-A-Part I: Physicochemical characterisation.* Journal of drug targeting, 2008. **16**(3): p. 213-223.

21. Plummer, E.M. and M. Manchester, *Viral nanoparticles and virus-like particles: platforms for contemporary vaccine design.* Wiley Interdisciplinary Reviews: Nanomedicine and Nanobiotechnology, 2011. **3**(2): p. 174-196.

22. Singh, M., A. Chakrapani, and D. O'Hagan, *Nanoparticles and microparticles as vaccine-delivery systems.* 2007.

23. van den Berg, J.H., et al., *Shielding the cationic charge of nanoparticle-formulated dermal DNA vaccines is essential for antigen expression and immunogenicity.* Journal of Controlled Release, 2010. **141**(2): p. 234-240.

24. Weaver, E.A. and M.A. Barry, *Effects of shielding adenoviral vectors with polyethylene glycol on vector-specific and vaccine-mediated immune responses.* Human gene therapy, 2008. **19**(12): p. 1369-1382.

25. Galloway, A.L., et al., *Development of a nanoparticle-based influenza vaccine using the PRINT® technology.* Nanomedicine: Nanotechnology, Biology and Medicine, 2013. **9**(4): p. 523-531.

26. Sunshine, J.C., et al., *Particle shape dependence of CD8+ T cell activation by artificial antigen presenting cells.* Biomaterials, 2014. **35**(1): p. 269-277.

27. Champion, J. and S. Mitragotri, *Shape Induced Inhibition of Phagocytosis of Polymer Particles.* Pharmaceutical Research, 2009. **26**(1): p. 244-249.

28. Martínez, M.J., et al., *The presence of capsular polysaccharide in mesophilic Aeromonas hydrophila serotypes O:11 and O:34.* FEMS Microbiology Letters, 1995. **128**(1): p. 69-73.

29. Peine, K.J., et al., *Efficient Delivery of the Toll-like Receptor Agonists Polyinosinic: Polycytidylic Acid and CpG to Macrophages by Acetalated Dextran Microparticles.* Molecular Pharmaceutics, 2013. **10**(8): p. 2849-2857.

30. Bourquin, C., et al., *Targeting CpG Oligonucleotides to the Lymph Node by Nanoparticles Elicits Efficient Antitumoral Immunity.* The Journal of Immunology, 2008. **181**(5): p. 2990-2998.

31. Wischke, C., et al., *Poly (I: C) coated PLGA microparticles induce dendritic cell maturation.* International Journal of Pharmaceutics, 2009. **365**(1): p. 61-68.

32. Zhou, Y., et al., *TLR3 activation efficiency by high or low molecular mass poly I: C.* Innate immunity, 2013. **19**(2): p. 184-192.

33. Champion, J.A., Y.K. Katare, and S. Mitragotri, *Making polymeric micro- and nanoparticles of complex shapes.* Proceedings of the National Academy of Sciences, 2007. **104**(29): p. 11901-11904.

34. Mathaes, R., et al., *Influence of particle geometry and PEGylation on phagocytosis of particulate carriers.* International Journal of Pharmaceutics, 2014. **465**(1): p. 159-164.

35. Foged, C., et al., *Particle size and surface charge affect particle uptake by human dendritic cells in an in vitro model.* International Journal of Pharmaceutics, 2005. **298**(2): p. 315-322.

36. Thiele, L., et al., *Evaluation of particle uptake in human blood monocyte-derived cells in vitro. Does phagocytosis activity of dendritic cells measure up with macrophages?* Journal of Controlled Release, 2001. **76**(1): p. 59-71.

37. Jung, T., et al., *Tetanus toxoid loaded nanoparticles from sulfobutylated poly (vinyl alcohol)-graft-poly (lactide-co-glycolide): evaluation of antibody response after oral and nasal application in mice.* Pharmaceutical Research, 2001. **18**(3): p. 352-360.

38. Nixon, D.F., et al., *Synthetic peptides entrapped in microparticles can elicit cytotoxic T cell activity.* Vaccine, 1996. **14**(16): p. 1523-1530.

39. Mathaes, R., et al., *Influence of particle geometry and PEGylation on phagocytosis of particulate carriers.* International Journal of Pharmaceutics, 2014. 465(1): p. 159-164.

40. Champion, J.A. and S. Mitragotri, *Role of target geometry in phagocytosis.* Proceedings of the National Academy of Sciences of the United States of America, 2006. **103**(13): p. 4930-4934.

41. Arnida, et al., *Geometry and surface characteristics of gold nanoparticles influence their biodistribution and uptake by macrophages.* European Journal of Pharmaceutics and Biopharmaceutics, 2011. **77**(3): p. 417-423.

# VI. Chapter 6

## Quality Control of Protein Crystal Suspensions Using Microflow Imaging and Flow Cytometry

* These authors contributed equally to this work

° These authors contributed equally to this work

ǂ Corresponding author

The following chapter was performed in close collaboration with Christian Hildebrandt. All experimental work was conducted together. Christian Hildebrandt guided the work related to the protein crystallization while I guided the analytical part. The publication has been written in equal parts.

Ahmed Besheer supported the experimental work with his analytical understanding, reviewed the manuscript and submitted it. Julia Engert and Gerhard Winter critically discussed the results and reviewed the manuscript.

The following chapter describes the characterization of protein crystal suspensions. Obviously this chapter is not directly associated to the topic of this thesis, which has its focus on drug delivery applications of non-spherical particles. However, several methods developed in this thesis to characterize the

shape of non-spherical particles showed potential to be used in the field of protein formulation.

The therapeutic protein investigated in this study was a needle shaped crystalline insulin. Some insulin pharmaceuticals are formulated in crystal suspension to tailor the release and pharmacokinetic profile of the insulin. The process of crystallization is a delicate step. Only minor changes in the crystallization process can lead to spherical amorphous insulin aggregates, which might show a different insulin release profile compared to the needle shaped insulin crystals.

In this study the shape characterization methods developed to analyze the non-spherical drug delivery particles were applied to discriminate spherical insulin impurities from needle shaped insulin crystals.

# 1. Abstract

Protein crystallization is an attractive method for protein processing and formulation. However, minor changes in the crystallization setup can lead to changes in the crystal structure or the formation of amorphous protein aggregates, which affect the product quality. Only few analytical tools for qualitative and quantitative differentiation between protein crystals and amorphous protein exist. Electron microscopy requires expensive instrumentation, demanding sample preparation, and challenging image analysis. Therefore, there is a need to establish other analytical techniques. It was the aim of this study to investigate the capability of light obscuration (LO), microflow imaging (MFI), and flow cytometry (FC) in differentiating the amorphous and crystalline states of insulin as a relevant model. Qualitative discrimination of the two populations based on the particle size was possible using LO. Quantitative determination of amorphous protein and crystals by MFI was challenging due to overlapping size distributions. This problem was overcome by particle analysis based on the mean light intensity. Additionally, FC was applied as a new method for the determination of the quality and quantity of amorphous protein by differences in the light scattering. Our results show the potential of MFI and FC for rapid high throughput screening of crystallization conditions and product quality.

## Keywords

# 2. Introduction

Crystallization is an important protein processing, formulation, and delivery tool, which is actively investigated at both the academic and industrial levels. This is because crystallization offers a wide field of application, including controlling/prolonging drug release,[1, 2] reducing the viscosity of highly

concentrated solutions by using crystal suspensions,[3] or increasing the protein stability.[1, 2, 4] However, it also offers a number of challenges, including the need to identify protein-friendly crystallization-processing conditions. Among the problems in protein crystal development is the fact that minor changes in crystallization conditions (changes in temperature, pH, concentration of additives, or mechanical treatment) can lead to changes in the product quality, such as changes in crystal morphology, size, stability, or even precipitation of the protein in an amorphous form [1, 5]. Rapid evaluation of the product quality is difficult, as there are still very few analytical methods for the quantitative characterization of protein crystals. The methods are traditionally divided into those that characterize morphology, and those that prove crystallinity. For the assessment of particle morphology and size distribution, microscopy, particularly electron microscopy is the most common method to analyze protein crystals.[6] Despite the strength of electron microscopy, it is a time consuming, low-throughput method that requires expensive instrumentation and nontrivial image analysis.[7] On the other hand, X-ray diffraction is commonly utilized to assess crystallinity, but needs perfectly grown crystals larger than 50 µm.[8] Therapeutic protein crystals should be much smaller due to syringeability issues.[8] Thus, it would be benefitial to establish different analytical methods, which can overcome these drawbacks and allow a simultaneous determination of amorphous impurities and proof crystallinity.

In the current study, we investigated the ability of microflow imaging (MFI) and flow cytometry (FC) to rapidly characterize the quality of protein crystals. For this purpose, we used insulin as a model protein. Crystalline insulin products from different manufacturers have huge market sales and have regulatory approval since decades.[8, 9] Minor changes in insulin's crystallization process are known to change the crystals' morphology, and foster amorphous precipitation.[10] Accordingly, MFI and FC were benchmarked against standard methods, namely light obscuration (LO), light microscopy (LM), and scanning electron microscopy.

## 3. Materials and Methods

### 3.1. Insulin

Insulin in crystal form (Insuman® basal) was a kind gift from Sanofi–Aventis (Frankfurt am Main, Germany). Human insulin (Humulin) (100 I.E. injection solution) from Lilly (Gießen, Germany) was purchased from the market. Lysozyme from chicken egg white as lyophilized powder (protein > 90%, > 40,000 units/mg protein) was purchased from Sigma–Aldrich (Taufkirchen, Germany). Sodium acetate (USP standard, analytical quality) was obtained from Merck (Darmstadt, Germany). Sodium chloride (AnalaR NORMAPUR) was obtained from VWR Prolabo (Leuven, Belgium). Zinc chloride was purchased from Ceasar & Lorenz (Hilden, Germany).

### 3.2. Amorphous Precipitation of Insulin

Amorphous insulin precipitates were obtained by mixing human insulin with a saturated zinc chloride solution in highly purified water at a 1:2 ratio.

### 3.3. Light Microscopy

For microscopy, a Biozero BZ-8000 microscope from Keyence (Neu-Isenburg, Germany) was used. The application BZ viewer was employed for analysis purposes. The samples were covered with glass cover slides. Examinations were carried out at 400-fold magnification.

### 3.4. Scanning Electron Microscopy

A JEOL JSM 6500F scanning electron microscope (Jeol Ltd., Tokyo, Japan) with Inca Software (Oxford instruments, Oxfordshire, UK) was utilized for particle morphology confirmation. Samples were sputtered with carbon after

sample fixing with selfadhesive tape on aluminum stubs. Samples were viewed at a magnification of 2000–11,000-fold.

### 3.5. Light Obscuration

A PAMAS SVSS-C40 (PAMAS GmbH, Rutesheim, Germany) light-blockage system was utilized to size (1–200 μm) and count particles. Particle count was classified into 16 different size ranges. The rinsing volume was set to 0.5 mL and the measurement volume to 0.3 mL.

### 3.6. Microflow Imaging

Particle size and mean intensity was measured using a MFI system from Brightwell Inc. (Ottawa, Canada). A constant particle stream was confirmed by utilizing a peristaltic pump. The sample volume was set to 1 mL. Calibration was performed with 5 μm polystyrene particle standards (Thermo Scientific, Fremont, California).

### 3.7. Flow Cytometry

A Bioscience flow cytometer FACS Canto II (Bioscience, Franklin Lakes, New Jersey) equipped with forward- and side-scattering laser was utilized to analyze protein crystals and amorphous precipitates. Detectors gain and sensitivity were optimized to maximize the particle detection. The forward-scatter (FSC) detector was set to 231 V and the side-scatter (SSC) detector was set to 191 V.

## 4. Results

Insuman® basal is an approved crystalline insulin product, therefore, it was chosen as the model crystalline protein. Samples containing crystals and

amorphous precipitate were produced by mixing suspended insuman basal samples (1 mL) with 2 µL of precipitated human insulin to simulate product impurities. This setup was employed for all analytical assessments.

Light microscopy and scanning electron microscopy were utilized to characterize the particle size and shape. Both methods displayed an oblong shape for the crystals with a Ferret diameter of 8 µm and width of 1 µm (Figure VI-1).Amorphous precipitates appeared as spherical particles sized up to 2 µm that tend to form clusters. After mixing of crystals and amorphous precipitates, both structures remained unaltered and were easily detectable. However, only qualitative information could be obtained from the images. Quantification was not possible due to clustering of the particles and the transparency of some particles.
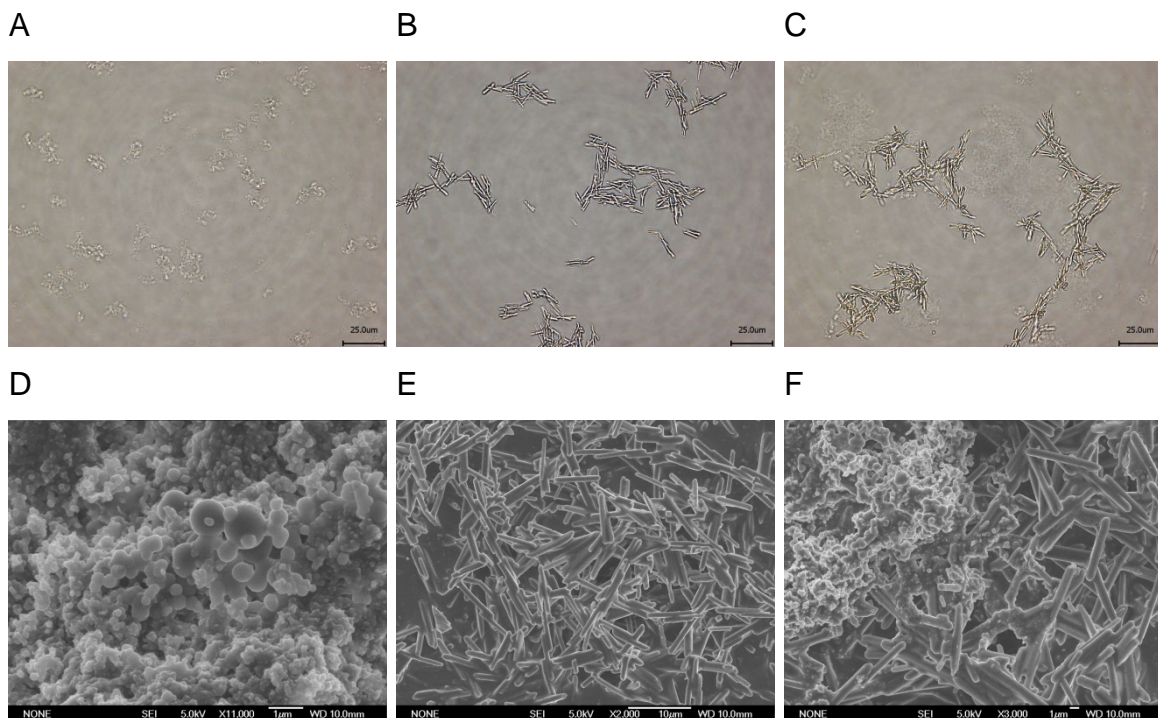


Figure VI-1: Light microscopy images of (a) amorphous human insulin, (b) insuman basal crystals, (c) mixture of insuman basal crystals and humaninsulin amorphous precipitates. The scale bar represents 25µm. Scanning electron micrographs of (d) human insulin amorphous precipitates, (d) insuman basal

crystals, (f) mixture of insuman basal crystals and human insulin amorphous precipitates.

The different samples were analyzed by LO, a standard method for particle characterization. LO measurements of the different protein samples showed that they differ in the mean size (1.64 vs. 10.24) and polydispersity index (PDI) (2.13 vs. 11.66) (Table VI-1) for the amorphous and crystalline particles, respectively (Figure VI-2A and Figure VI-2B). Over 99% of the amorphous aggregates were smaller than 4.1 µm (Figure VI-2A), while over 93% of the crystalline insulin were larger than 4.1 µm. Thus, two distinct particle fractions can be discriminated, even in the mixture of both materials (Figure VI-2C).

Table VI-1. The mean size and polydispersity index of the SVSS-C PAMAS Particle Counter (LO) of amorphous insulin aggregates and insulin crystals are displayed

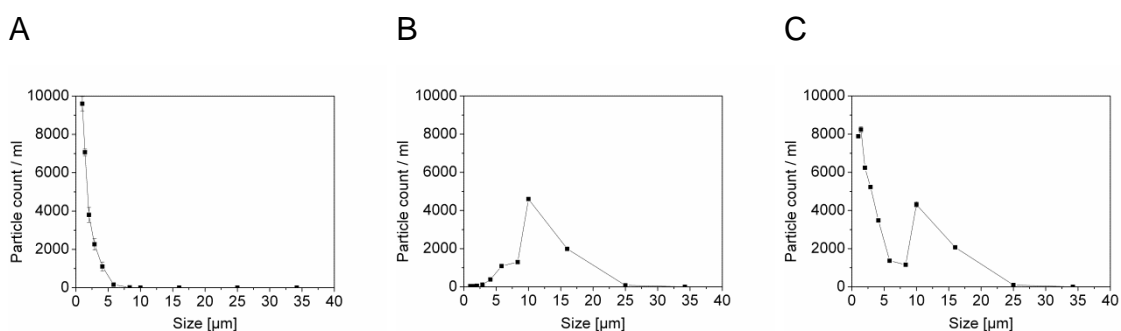|  | Mean Size (µm) | PDI |
| --- | --- | --- |
| Amorphous aggregates | 1.64 | 2.13 |
| Crystals | 10.24 | 11.66 |

A          B          C



Figure VI-2: The SVSS-C PAMAS particle counter (LO) measurement of insulin. (a) amorphous insulin aggregates, (b) insulin crystals, (c) mixture of amorphous insulin aggregates and insulin crystals.

The image-analysis-based MFI system detects particles flowing through a capillary, where the particle stream is imaged by a camera. Particle size is

calculated by the image-analyzing software, which also provides information about particle morphology.[11] Besides the particle count, the mean intensity of the particle is also assessed. This feature gives information about the optical density and can be used as a tool to distinguish between aggregates and crystals.

In contrast to LO, assessment of particle size using MFI does not show a clear separation into two different populations. Although the mean size of the aggregates is rather small compared with the crystals, (2.92 vs. 10.63, respectively), the particle distribution is rather broad (PDI = 10.64 for the aggregates and 13.53 for the crystals) (Figure VI-3), so that the two populations overlap in the mixture (Figure VI-3G). Thus, analysis of the mean intensity was used for better discrimination. The standard MFI software offers the possibility to determine the gray scale of the detected objects. The mean intensity is a dimensionless number with low values for dark objects. While amorphous precipitates show a mean intensity of approximately 801 (Figure VI-3B), the crystal values are around 644 (Figure VI-3E), indicating that the crystals appear darker in the MFI images. Using this method, two separate populations can be easily identified and quantified as shown in (Figure VI-3H).

A                                    B                                    C

D

E

F

G

H

I
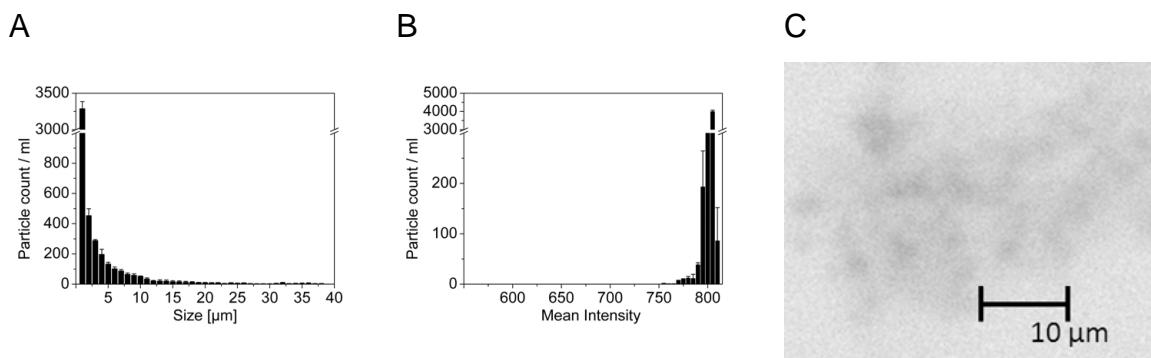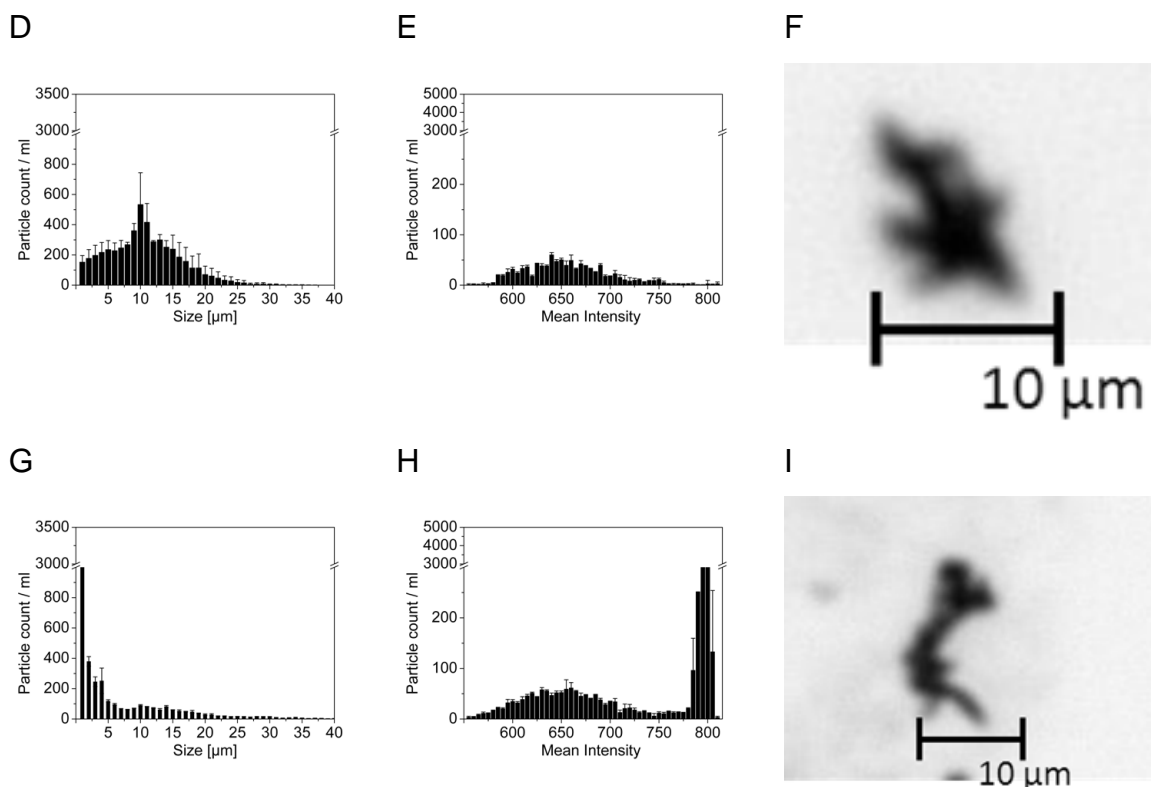
Figure VI-3: MFI size distribution measurements of (a) amorphous insulin aggregates, (d) crystalline insulin, (g) mixture of crystalline and amorphous insulin. Mean intensity measurements of (b) amorphous insulin aggregates, (d) crystalline insulin and (h) mixture of crystalline and amorphous insulin. MFI images of (c) amorphous insulin aggregates, (f) crystalline insulin and i) mixture of crystalline and amorphous insulin.

Flow cytometry was used as an additional tool for the analysis of aggregate and crystalline insulin particles. FC measurements in the range of 0.5–20 µm of protein subvisible particles have already been reported.[12] Results show that based on light scattering, one can identify distinct populations in FC dot plots. While the protein crystals show relatively high forward and side scatter values, the aggregates are expressed in a population with lower forward and side scatter values (Figure VI-4), allowing the identification of those impurities in the mixture (Figure VI-4C).

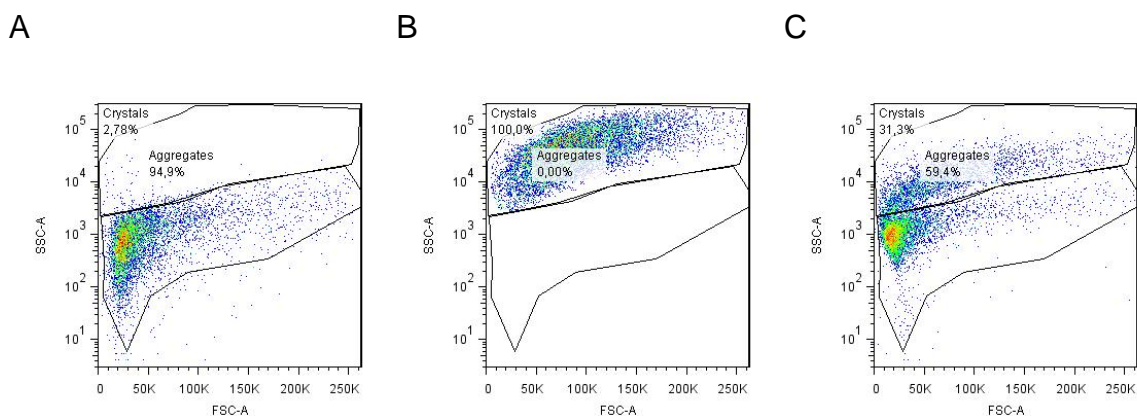Figure VI-4: Flow cytometry dot plots of (a) amorphous insulin, (b) insulin crystals, (c) mixture of amorphous and crystalline insulin.

## 5. Discussion

The product quality of protein crystal suspensions is strongly dependent on reproducible production conditions. Minor changes can lead to the precipitation of amorphous protein aggregates. An appropriate analytical tool should allow for the determination of the product's quality and would also quantify the degree of impurities. Microscopic techniques are often used to confirm the crystalline state. However, the accurate quantification of impurity needs the effort of using scanning electron microscopy (including sample preparation) and nontrivial image analysis. In contrast to microscopic observations, the methods investigated in this study allow rapid quantitative analysis of product quality, and are amenable for high throughput analysis, thus allowing the screening of protein crystallization conditions or monitoring the crystal quality by frequent in-process controls. LO was tested as a method that is commonly used in product particle analysis. This approach can size particles in the amorphous and crystalline state. LO measurements show that amorphous precipitates were in the size range of 1–5 μm while crystals show sizes from 4 to 25 μm (Figure VI-2A and Figure VI-2B). In our experiments, differentiation between crystals and amorphous aggregates was possible based solely on the particle size. However, if the particle sizes in other samples were similar or the distributions

were broader, a differentiation based solely on the size would have not been possible.

Meanwhile, MFI showed a larger size range for the amorphous aggregates (1–12 µm) and for the crystals (0.75–26 µm) compared to LO. Such differences between MFI and LO were reported previously while measuring standard polystyrene particles of different sizes and shapes.[13] One possible reason is the lower accuracy of LO for particles smaller than 2 µm. Due to the broad size distribution; identification of the crystals and amorphous aggregates based only on the particle size was not possible, as both groups overlapped. However, using the mean intensity allowed the identification of two separate populations based on the fact that the crystals appeared darker than the amorphous aggregates. Possible reasons for this can be different refractive indices between the crystals and aggregates, or greater thickness (and accordingly greater path length) for the crystals, associated with larger light scattering.

Flow cytometry was also used in this study. The use of this tool was described before in the context of protein aggregate analysis or contamination with silicone oil in biopharmaceutical products.[12-14] The flow cytometer can measure large particle numbers in a very short time frame (up to 5000 particles/s). This single-particle measurement method can analyze size ranges from 0.5 to 100 µm. To our best knowledge, this is the first reported use of flow cytometer for differentiation of protein crystals and amorphous precipitates. FC measurements expressed as dot plots show the aggregates as a population with relatively low forward and side scatter (Figure VI-4). Contrary, the oblong protein crystals show a different scattering pattern dependent on the orientation of the crystal with respect to the incident light beam, with higher forward and side scatters (Figure VI-4). These results allow for qualitative, quantitative, and clear discrimination between insulin crystals and amorphous precipitates.

## 6. Conclusion

The presented study shows the potential applicability of MFI and FC for the differentiation between crystalline and amorphous protein precipitates and the assessment of crystalline protein quality. MFI and FC are rapid and reliable methods, which provide quantitative and statistically valuable information. To the best of our knowledge, MFI and flow cytometry were used for the first time for the determination of amorphous impurities in protein crystal suspensions. The presented tools open new possibilities in industrial early-phase crystallization screening as well as large-scale product quality control of crystalline biopharmaceutical products.

## 7. Acknowledgments

## 8. References

1.  Jen, A. and H. Merkle, Diamonds in the Rough: Protein Crystals from a Formulation Perspective. Pharmaceutical Research, 2001. 18(11): p. 1483-1488.
2.  Pechenov, S., et al., Injectable controlled release formulations incorporating protein crystals. Journal of Controlled Release, 2004. 96(1): p. 149-158.
3.  Yang, M.X., et al., Crystalline monoclonal antibodies for subcutaneous delivery. Proceedings of the National Academy of Sciences, 2003. 100(12): p. 6934-6939.
4.  Shenoy, B., et al., Stability of crystalline proteins. Biotechnology and bioengineering, 2001. 73(5): p. 358-369.
5.  Durbin, S. and G. Feher, Protein crystallization. Annual review of physical chemistry, 1996. 47(1): p. 171-204.
6.  Groves, M.R., et al., A method for the general identification of protein crystals in crystallization experiments using a noncovalent fluorescent dye. Acta Crystallographica Section D: Biological Crystallography, 2007. 63(4): p. 526-535.
7.  Vermant, J., H. Yang, and G.G. Fuller, Rheooptical determination of aspect ratio and polydispersity of nonspherical particles. AIChE Journal, 2001. 47(4): p. 790-798.
8.  Basu, S.K., et al., Protein crystals for the delivery of biopharmaceuticals. Expert opinion on biological therapy, 2004. 4(3): p. 301-317.
9.  Frokjaer, S. and L. Hovgaard, Pharmaceutical formulation development of peptides and proteins1999: CRC.
10. McPherson, A., Introduction to protein crystallization. Methods, 2004. 34(3): p. 254-265.
11. Singh, S.K., et al., An industry perspective on the monitoring of subvisible particles as a quality attribute for protein therapeutics. Journal of Pharmaceutical Sciences, 2010. 99(8): p. 3302-3321.
12. Mach, H., et al., The use of flow cytometry for the detection of subvisible particles in therapeutic protein formulations. Journal of Pharmaceutical Sciences, 2011. 100(5): p. 1671-1678.
13. Mathaes, R., et al., Application of different analytical methods for the characterization of non-spherical micro- and nanoparticles. International Journal of Pharmaceutics, 2013. 453(2): p. 620-629.
14. Ludwig, D.B., et al., Flow cytometry: A promising technique for the study of silicone oil-induced particulate formation in protein formulations. Analytical Biochemistry, 2011. 410(2): p. 191-199.

# VII. Chapter 7

**Summary**

Micro- and nanoparticles are extensively investigated as drug delivery systems (DDSs) since the 1970s. Researchers have increased the performance of DDSs by tailoring their design parameters, like size, surface chemistry and flexibility. However, particle shape was usually neglected. The purpose of the current thesis is to contribute to fill that gap.

A reproducible method to fabricate non-spherical particles was established and a number of analytical methods were developed to characterize particle shape in the different size ranges. In a second step, the impact of particle shape on the immune system was investigated using a macrophages cell line and a dendritic cell line.

The influence of particle shape on immune cells was insufficiently described in literature with two possible outcomes. Firstly, a non-spherical particle shape reduces uptake into phagocytic cells like macrophages and secondly, a non-spherical shape triggers immune cell activation. Therefore, the *in-vitro* experiments were divided into two parts: Particle uptake was investigated with a macrophages cell line, immune cell activation was investigated with a dendritic cell line.

In the general introduction (chapter 1) the latest fabrication methods for non-spherical particles are summarized and evaluated towards large scale production capabilities. Non-spherical particles require complementary analytical techniques to be characterized. In addition, the impact of different particle geometries on biological interaction is outlined. Firstly, the influence of particle geometry on particle up-take into different phagocytic cells and the bio-distribution is summarized. Moreover, current research fields like shape dependent uptake mechanisms and applications for tumor therapy and

vaccination are described. Finally, an expert opinion is given, which discusses key challenges and future trends of non-spherical drug delivery systems.

In the early stage of the project (chapter 2) the simple but reproducible film-stretching method was established in our laboratory to fabricate elongated micro-and nanoparticles. In a second step those non-spherical particles were characterized. In the past electron microscopy was usually the only applied analytical method to investigated particle shape. However, it is expensive, requires demanding sample preparation, and analyzes only a small fraction of the complete particle population. Therefore, we used our well-defined non-spherical particles to establish innovative high throughput methods to close the analytical gap for non-spherical particles. For example, the micro flow imaging technique was utilized to analyze non-spherical particles in the range of 5 – 10 μm. In addition, flow cytometry was used to analyze particle shape in the range of 2 – 10 μm and asymmetric flow field flow fractionation to characterize particle shape in the range of 20 – 200 nm.

In chapter 3 the versatile asymmetric flow field flow fraction method used to separate nanoparticles of different shapes. However, the washing procedure and the focus sequence of the asymmetric flow field flow fraction method lead to the aggregation of the non-spherical nanoparticles. A precise analysis of the non-spherical particles was not applicable. Chapter 3 highlights the versatility of the AF4 methods, but also controversially discusses the complexity of the method, including a demanding method development.

Following non-spherical fabrication and characterization, the established non-spherical micro- and nanoparticles were tested *in-vitro*:

Chapter 4 describes the comparison of particle up-take into J774.A1 macrophages of PEGylated and un-PEGylated spherical and non-spherical particles. Therefore, spherical and non-spherical micro-and nanoparticles were PEGylated. PEGylation as well as stretching particles towards an elongated particle shape reduced the incident for internalization by macrophages. A combination of the non-spherical shape and PEGylation had an additive effect

for the nanoparticles. Chapter 4 highlights the need to combine different drug delivery system design parameters to achieve a desirable and tailored biological performance.

In addition to particle up-take, in chapter 5, dendritic cell activation was investigated using the dendritic cell line JAWSII. Different vaccine adjuvants were adsorbed to spherical and non-spherical micro- and nanoparticles to form vaccine delivery vehicles. The adjuvants tested in this thesis were a high molecular weight polyI:C, a low molecular weight polyI:C and the Resiquimod analogue CL264. Then the different vaccine delivery vehicles were compared towards their potential to stimulate the dendritic cells. In our study the high molecular weight polyI:C was the most potent adjuvant and nanoparticles stimulated the dendritic cells stronger than microparticles. Finally, spherical particles stimulated the dendritic cells stronger than the non-spherical particles. Consequently, the spherical nanoparticles with adsorbed high molecular weight polyI:C were the superior vaccine delivery vehicle.

Non-spherical particle characterization is not only important in the field of drug delivery. Obviously, challenges in the field of protein formulation were not directly associated with the topic of this thesis. However, the developed methods in Chapter 2 and 3 can be applied to the analytical tool box of protein formulation. For example, crystalline insulin is a multi-billion dollar pharmaceutical product and contains of non-spherical needle shaped crystals. In contrast, amorphous insulin impurities display a spherical shape. In chapter 6 the characterization methods of chapter 2 were applied to biologics manufacturing quality control. Therefore, microscopy, micro flow imaging, and flow cytometry were utilized to identify and quantify spiked-in spherical insulin impurities in crystalline insulin suspensions.

Taking together the conclusions of all chapters, non-spherical particles were reproducibly fabricated and characterized. The impact of particle shape on the interaction with macrophages and dendritic cells was studied. A remarkable difference between the non-spherical and spherical particles was observed *in-*

*vitro*. Particle shape has the potential to play an important design parameter in future of drug delivery systems.

# VIII.Appendix

## Publications Associated with this Thesis:

**Mathaes, R**., Winter, G., Besheer, A.*, & Engert, J.*‡ (2014). Non-spherical micro- and nanoparticles: fabrication, characterization and drug delivery applications. Expert Opinion on Drug Delivery, 2014. 12(3): p. 481-492.

**Mathaes, R**., Winter, G., Engert, J.*, & Besheer, A.* ‡ (2013). Application of different analytical methods for the characterization of non-spherical micro-and nanoparticles. International Journal of Pharmaceutics, 453(2), 620-629.

**Mathaes, R**., Winter, G., Besheer, A.* ‡, & Engert, J.*‡ (2014). Influence of particle geometry and PEGylation on phagocytosis of particulate carriers. International Journal of Pharmaceutics, 465(1), 159-164.

**Mathaes, R**., Winter, G., Siahaan, T., Besheer*,A., Engert*‡,J., Influence of particle size, geometry, and adjuvants on dendritic cell activation, (this manuscript is in the submitted for publication to the European Journal of Pharmaceutics and Biopharmaceutics.)

# Additional Publications Written During the research period (not directly associated with this thesis)

**Mathaes, R**.*, Hildebrandt, C.*, Winter, G., Engert, J.°, & Besheer, A°‡. (2013). Quality Control of Protein Crystal Suspensions Using Microflow Imaging and Flow Cytometry. Journal of Pharmaceutical Sciences, 102(10), 3860-3866.

Nishi, H., **Mathäs, R**., Fürst, R.,  Winter, G. (2014). Label-Free Flow Cytometry Analysis of Subvisible Aggregates in Liquid IgG1 Antibody Formulations. Journal of Pharmaceutical Sciences, 103(1), 90-99.

Liebner, R., **Mathaes, R**., Meyer, M., Hey, T., Winter, G., Besheer, A. (2014). Protein HESylation for half-life extension: Synthesis, characterization and pharmacokinetics of HESylated anakinra. European Journal of Pharmaceutics and Biopharmaceutics, 87(2), 378-385.

Deng, Y., **Mathaes, R**., Winter, G., Engert, J. (2014). Encapsulation of antigen-loaded silica nanoparticles into microparticles for intradermal powder Injection. European Journal of Pharmaceutical Sciences, 63, 154-166.

Kalonia, C., Kumru, OS., Prajapati, I., **Mathaes, R**., Engert, J., Zhou,S., Middaugh, RC. and Volkin, DB (2014). Calculating the Mass of Subvisible Protein Particles with Improved Accuracy Using Microflow Imaging Data. Journal of Pharmaceutical Science, 104 (2), 536-547.

Hildebrandt, C.\*, **Mathaes, R.**\*, Saedler, R., Winter, G. Origin of aggregate formation in antibody crystal suspensions containing PEG, (this manuscript is in the submission process for publication.)

# IX. Curriculum Vitae

Roman Mathäs

Wohnhaft in Basel

Geboren am 15. Jan 1985

In Mainz

| | |
|---|---|
| 08.2014 bis heute | Roche, Basel |
| 01.2011 - 06.2014 | Wissenschaftlicher Mitarbeiter: AK Prof. Winter |
| | Promotion am Lehrstuhl Pharmazeutische Technologie und Biopharmazie der Ludwigs-Maximilian Universität München |
| 10.2012 - 05.2014 | MBA-Fernstudium: General Management |
| | University Cardiff und Fernuniversität Hagen |
| 05.2010 - 11.2010 | Praktisches Jahr, Roland Apotheke, Berlin |
| 11.2009 - 05.2010 | Praktisches Jahr, Kings College London |
| 10.2005 - 11.2009 | Pharmaziestudium Philipps-Universität Marburg |
| 06.2004 - 06 2005 | Zivildienst, Deutsches Rotes Kreuz, Mainz |
| 06.1991 - 04.2004 | Schule, St. Katharinen Gymnasium, Oppenheim |